

**On the transport of alkali ions through
polymeric mold compounds
and
polyelectrolyte membranes**

Dissertation

Zur Erlangung des Doktorgrades
der Naturwissenschaften

(Dr. rer. nat.)

dem Fachbereich Chemie
der Philipps-Universität Marburg

vorgelegt von

Viviana Motta, M.Sc.

aus Syrakus (Italien)

Marburg, 2019

Die vorliegende Arbeit wurde im Zeitraum von Januar 2015 bis Januar 2019 am Fachbereich Chemie der Philipps-Universität Marburg unter der Leitung von Herrn Prof. Dr. Karl-Michael Weitzel angefertigt.

Erstgutachter: Prof. Dr. Karl-Michael Weitzel

Zweitgutachter: Prof. Dr. Wolfgang Parak

Tag der Einreichung: 24.05.2019

Tag der mündlichen Prüfung: 09.07.2019

Hochschulkennziffer: 1180

To my family,

“Nothing in life is to be feared, it is only to be understood. Now is the time
to understand more, so that we may fear less.”

Marie Curie (1867 – 1934)

Acknowledgement

During my time as a doctoral student at the University of Marburg, many people helped me to complete the work of this thesis. Therefore, I want to thank them warmly, as they contributed to the success of this work.

First of all, I would like to address many thanks to Prof. Karl-Michael Weitzel for giving me the opportunity to conduct my PhD course in a foreign country, i.e. at the chemistry department of the University of Marburg. I thank him for letting me work on an interesting and versatile field of research. His guidance by means of scientific discussions helped me throughout my research.

I gratefully acknowledge Dr. Martin Schäfer for his continuous support and enthusiasm, which gave me the right attitude to motivate myself throughout all the projects. I thank him for teaching me how to work in a team, how to develop my academic skills and how to embrace the responsibility and honor of becoming a researcher and a scientist. I also thank him for his care in proofreading the sections of this thesis.

I have had productive collaborations throughout these years. For that, I wish to extend my gratitude to Dr. Jonas Hühn for the fruitful discussions and collaboration on the PEMs project. Moreover, I want to thank Prof. Wolfgang J. Parak for his availability in preparing the second appraisal and Dr. Stefan Schwab and Prof. Herbert Hutter for providing the mold compounds studied within the work of this thesis.

I also extend my sincere thanks to the employees of the workshops for helping me with technical issues, in particular: Herr Karl Keitzel (mechanical workshop) and Herr Nobert Frommknecht (electronics workshop). Moreover, I wish to thank Dr. Frank Noll for the realization of SEM analysis shown in this work and Frau Elke Washk for all her essential assistance with travel arrangements and bureaucratic matters at my arrival in Marburg.

I gratefully acknowledge each and every member of the AG Weitzel who helped me inside and outside the academic sphere. I hope I was able to infuse part of my culture with my acting and manners, although I always respected usage and customs of the German culture, adapting my attitude to them. I want to thank especially my colleague Anneli Hein for having made me feel welcome at my arrival in Germany and her constant support throughout the whole time in Marburg.

I thank my parents, my brother Giuseppe and all the closest member of my family, in particular my grandparents, my aunt Maria, my cousin Adriana, my parents-in-law and my dear friends Chiara, Vanessa P. and Kristina. I am incredibly grateful for their support, understanding and encouragement during the best and the worst periods of this adventure of life. Finally, but most importantly, I thank Manuel, who joined me the first time I met the members of my group. He has never left me alone in dealing with difficulties of the daily and working life, but rather encouraged me in facing them and becoming an adult and a responsible person. I thank him because we were in this together since the beginning and this success is dedicated to him as well.

Abstract

The aim of this work is the attempt in understanding ion transport properties across structured materials such as polyelectrolyte multilayers (PEMs) and highly filled epoxy resins used as an encapsulant, i.e. mold compounds. The ion transport properties are studied by means of the technique of charge attachment induced transport (CAIT), which was recently developed and time-of-flight secondary ion mass spectrometry (ToF-SIMS). The mold compounds studied in this work are of four types (MCP1, MCP2, MCP3, MCP4) with a composition of 80% - 88% of silica filler and the rest of raw materials such as epoxy resin, hardener and flame retardant. The samples are analyzed by means of the CAIT technique, leading to the evaluation of values of ionic conductivity and activation energy related to the process of transport of potassium ions. The ionic conductivity of the mold compounds is on the order of $10^{-12}/10^{-13}$ S/cm, while activation energy values are in a range of 1.3 eV - 2.7 eV. For a better understanding of the potassium diffusion process into the mold compounds, the diffusion of potassium through MCP3 sample is investigated via a combination of CAIT method and an ex-situ ToF-SIMS analysis. The ToF-SIMS analysis reveals a depth diffusion profile of the potassium into the material. A mathematical theory is established in order to evaluate the diffusion coefficients for the transport of potassium. According to the numerical procedure, a good fit between experimental and theoretical data is achieved assuming the presence of two different transport pathways operative inside the material: diffusion along the boundaries of grains, i.e. zones of accumulation of the inorganic component of the mold compound and diffusion through the bulk. Diffusion coefficients of $D_B = 1.8 \times 10^{-21} \text{ cm}^2\text{s}^{-1}$ and $D_{BG} = 5.4 \times 10^{-20} \text{ cm}^2\text{s}^{-1}$ are found for bulk and grain boundary diffusion, respectively.

The PEM films studied in this work are prepared from the layer-by-layer assembly of ionic p-sulfonato-calix[8]arene (calix8) and cationic poly(allylamine hydrochloride) (PAH) onto functionalized gold substrates. Samples with $n = 1, 3, 6, 9, 12, 15, 20, 30$ bilayers are analyzed by means of the CAIT technique. The data lend support to the conclusion that conductivity, as well as activation energy measurements for $(\text{PAH}/\text{calix8})_n$, cannot be acquired under the conditions of the CAIT method, due to the low resistivity shown from the specific PEMs analyzed. Studies on the transport of Li^+ , K^+ and Rb^+ through $(\text{PAH}/\text{calix8})_{30}$ are performed by means of CAIT and ToF-SIMS. For each ion beam (Li^+ , K^+ , Rb^+) two kind of experiments are performed: $(\text{PAH}/\text{calix8})_{30}$

samples are bombarded with the three different alkali ions varying the time for the bombardment, i.e. 5 seconds in one case and 100 seconds in the other. The evaluation of the concentration profiles gives qualitative information regarding the transport properties, whereas numerical analysis of the lithium and rubidium concentration profiles for 5 seconds long bombardment provides quantitative information on the diffusion process. The numerical calculation reveals that the lithium and rubidium transport across the membrane results in a combination of two diffusion pathways accounting for diffusion of slow ions and fast ions. For the lithium case, a good fit is achieved using diffusion coefficients of $D_{\text{slow, Li}^+} = 0.4 \times 10^{-16} \text{ cm}^2/\text{s}$ and $D_{\text{fast, Li}^+} = 1.2 \times 10^{-15} \text{ cm}^2/\text{s}$ and assuming that 40% of the incoming ions enter the slow pathway, whereas the rest of the ions is transported via a fast pathway. For the rubidium case, the numerical calculation reveals that the fast diffusion pathway is predominant: only the 0.01% of the rubidium ions enter the slow pathway, whereas the rest is dominated from the faster one, with a $D_{\text{fast, Rb}^+} = 7 \times 10^{-15} (\pm 1.5 \times 10^{-15}) \text{ cm}^2/\text{s}$. The study of ion transport of alkali ions Li^+ and Rb^+ across calixarenes-based PEMs leads thus to the conclusion that the presence of the calixarenes units may influence the type of transport.

Lastly, studies of voltage offset measured on current-voltage curves in a typical CAIT experiment are presented. This study aims to give a better understanding of the process beyond the measured voltage offset. In order to do that, a basic CAIT experiment is performed, where a metal plate is bombarded with an ion beam from a potassium emitter of the composition $\text{KAlSi}_2\text{O}_6 : \text{Mo} (1:9)$. The registered current-voltage curves show finite offsets in the order of 0.5 eV. In order to investigate the detection process of the specific $\text{KAlSi}_2\text{O}_6 : \text{Mo} (1:9)$ emitter, values of ionic and electronic work function are evaluated. By means of a theoretical model, the recombination of K^+ ions from Leucite $\text{KAlSi}_2\text{O}_6 : \text{Mo} (1:9)$ onto the metal detector is traced to a combination of the ionic work function of the emitter material, the electronic work function of the emitter material and the recombination energy of the elemental potassium I.E.K.

Zusammenfassung

Das Ziel dieser Arbeit ist es, die Ionentransporteigenschaften über strukturierte Materialien wie Polyelektrolyt Multilagen (PEMs) und sogenannte „Mold compounds“, die als Vergussmasse zum Beispiel für Computerchips verwendet werden, zu verstehen. Die Ionentransporteigenschaften werden mit Hilfe des kürzlich entwickelten „charge attachment induced transport“ (CAIT), einer Methode bei der Ladungsträgertransport durch Anlagerung von geladenen Teilchen auf der Probenoberfläche induziert wird, und der Flugzeit-Sekundärionen-Massenspektrometrie (ToF-SIMS) untersucht.

Im Rahmen dieser Arbeit wurden vier unterschiedliche Typen von „mold compounds“ untersucht, die sich in Ihrer Zusammensetzung unterscheiden. Dabei wurde der Anteil des Kieselsäure-Füllstoff sowie der Anteil der Epoxidharz, Härter und Flammschutzmittel variiert. Die Proben werden mit Hilfe der CAIT-Technik analysiert. Dabei erhält man Werte für die Ionenleitfähigkeit und die Aktivierungsenergie im Zusammenhang mit dem Transport von Kaliumionen. Die Ionenleitfähigkeit der „mold compounds“ liegt in der Größenordnung von 10^{-12} / 10^{-13} S/cm, während die Aktivierungsenergie in einem Bereich von 1.3 eV bis 2.7 eV liegen. Zum besseren Verständnis des Kaliumdiffusionsprozesses in den „mold compounds“ wird die Diffusion von Kalium mit einer Kombination der CAIT-Methode und einer Ex-situ-ToF-SIMS-Analyse untersucht. Die ToF-SIMS-Analyse zeigt ein Diffusionstiefenprofil des Kaliums in der Probe. Es wird eine mathematische Theorie auf Basis der Nernst-Planck-Poisson Gleichungen genutzt, um die Diffusionskoeffizienten für den Transport von Kalium zu bestimmen. Eine gute Übereinstimmung zwischen experimentellen und theoretischen Profile erreicht man unter der Annahme, dass zwei unabhängige Transportwege vorhanden sind. Man kann die Diffusion durch das Volumen des Materials sowie die Diffusion entlang von Korngrenzen unterscheiden. Diffusionskoeffizienten von $D_B = 1.8 \times 10^{-21} \text{ cm}^2\text{s}^{-1}$ und $D_{BG} = 5.4 \times 10^{-20} \text{ cm}^2\text{s}^{-1}$ werden für die Volumen- bzw. Korngrenzendiffusion gefunden.

Die in dieser Arbeit untersuchten PEM-Filme werden Schicht für Schicht aus ionischem p-Sulfonato-Calix[8]arene (Calix8) und kationischem Poly(allylaminhydrochlorid) (PAH) auf funktionalisierten Goldsubstraten hergestellt. Proben mit $n = 1, 3, 6, 9, 12, 15, 20, 30$ Doppelschichten werden mittels der CAIT-Technik analysiert. Die durchgeführten Strommessungen zeigen, dass Leitfähigkeits- und Aktivierungsenergiemessungen für

(PAH / calix8)_n unter den Randbedingungen der CAIT-Methode aufgrund des niedrigen spezifischen Widerstands nicht erfasst werden können. Die erreichbaren Ionenstromstärken reichen nicht aus, um die Oberfläche auf das Quellpotential aufzuladen. Daher wurde eine Probe mit 30 Doppelschichten zunächst mit Hilfe von CAIT mit einem Alkaliionenstrahl beschienen und nachfolgend mit ToF-SIMS untersucht. Aus dem so entstandenen Tiefenprofil erhofft man sich Aussagen über den Diffusionskoeffizienten ableiten zu können. Das Experiment wurde mit drei unterschiedlichen Alkaliionenstrahlen durchgeführt: Li⁺, K⁺, Rb⁺. Mit jedem der Ionenstrahlen wurde zunächst eine Probe für 5 s beschienen. In einer zweiten Sequenz von Experimenten wurden die Proben für 100 s mit dem Ionenstrahl beschienen. Die Auswertung der Konzentrationsprofile liefert qualitative Informationen über die Transporteigenschaften, während die numerische Analyse der Lithium- und Rubidium-Konzentrationsprofile für einen 5 Sekunden langen Beschuss quantitative Informationen über den Diffusionsprozess liefert. Die numerische Berechnung zeigt, dass der Lithium- und Rubidiumtransport durch Transport auf zwei unterschiedlichen Wegen stattfindet. So konnten schnelle und langsame Ionen unterschieden werden, die dezidiert unterschiedliche Diffusionskoeffizienten aufwiesen. Für den Transport von Lithium wird eine gute Übereinstimmung zwischen experimentellen und theoretischen Profilen unter Verwendung von Diffusionskoeffizienten $D_{\text{slow, Li}^+} = 0.4 \times 10^{-16} \text{ cm}^2/\text{s}$ und $D_{\text{fast, Li}^+} = 1.2 \times 10^{-15} \text{ cm}^2/\text{s}$ erreicht. Man musste dazu annehmen, dass 40% der eintretenden Ionen den langsamen Pfad durch die Probe nehmen, während der Rest der Ionen über einen schnellen Weg transportiert wird. Für den Rubidium Transport zeigt die numerische Berechnung, dass der schnelle Diffusionsweg vorherrscht: Nur 0.01% der Rubidiumionen treten in den langsamen Weg ein, während der Rest den schnelleren Pfad nimmt wird, mit einem $D_{\text{fast, Rb}^+} = 7 \times 10^{-15} (\pm 1.5 \times 10^{-15}) \text{ cm}^2/\text{s}$. Die Untersuchung des Ionentransports der Alkaliionen Li⁺ und Rb⁺ durch PEMs auf Calixarene-Basis führt daher zu dem Schluss, dass die Anwesenheit der Calixarene-Einheiten die Art des Transports beeinflussen kann.

Zuletzt werden Studien zum Spannungsversatz an Strom-Spannungs-Kurven in einem typischen CAIT-Experiment vorgestellt. Diese Studie hatte das Ziel, die Neutralisations- und Kontaktprozesse an den Grenzflächen zu verstehen. Dazu wird ein grundlegendes CAIT-Experiment durchgeführt, bei dem eine Metallplatte mit einem Ionenstrahl aus einem Kaliumemitter der Zusammensetzung KAlSi₂O₆: Mo (1:9) beschossen wird. Die

erfassten Strom-Spannungs-Kurven zeigen endliche Offsets in der Größenordnung von 0.5 eV. Um den Detektionsprozess des spezifischen Emitters $\text{KAlSi}_2\text{O}_6: \text{Mo} (1: 9)$ zu untersuchen, werden Werte der ionischen und elektronischen Austrittsarbeit ausgewertet. Anhand eines theoretischen Modells wird die Rekombination von K^+ -Ionen aus Leucite $\text{KAlSi}_2\text{O}_6: \text{Mo} (1: 9)$ auf dem Metalldetektor auf eine Kombination der ionischen und elektronischen Austrittsarbeit des Emittermaterials und zurückgeführt die Rekombinationsenergie des elementaren Kaliums I.E._K.

Table of content

1 Introduction and motivations	1
2 Theoretical background	4
2.1 Polyelectrolyte multilayers	4
2.2 Mold compounds	10
2.3 Ion transport in condensed matter	14
2.3.1 Diffusion	16
2.3.2 Grain boundary diffusion	21
2.3.3 Electrodiffusion	26
2.3.4 Ion Transport through PEMs	34
2.4 Thermionic emission	37
3 Methods of analysis	40
3.1 CAIT Description	40
3.2 Time-of-flight Secondary Ions Mass Spectrometry (ToF-SIMS)	43
3.2.1 Principle of a SIMS analysis	43
3.2.2 ToF-SIMS Setup	46
3.2.3 Analysis modes: mass spectra, surface imaging, depth profiling	54
3.3 Profilometry	56
3.4 Sputter coating	57
4 Experimental part	58
4.1 Experimental CAIT setup	58
4.1.1 Ion emitters	59
4.1.2 Ion optics and sample holder	61
4.2 Samples preparation	64
4.2.1 Substrates and polyelectrolyte multilayers preparation	64
4.2.2 Mold compounds samples	70

4.3 ToF-SIMS conditions	71
4.4 Dektak.....	72
5 Results and discussion	73
5.1 MCP results and discussion	73
5.1.1 Conductivity measurements and activation energies.....	73
5.1.2 Diffusion of potassium through MCP3 and numerical simulations	81
5.2 Polyelectrolyte multilayers results and discussion	91
5.2.1 Design I : glass/Cr/Au/PEMs system.....	91
5.2.2 Design II : steel/Au/PEMs system	98
5.2.3 Design III : steel/Cr/Au/PEMs system.....	98
5.2.4 Design IV : steel/Au-foil/PEMs system.....	105
5.3 Measurements of offsets in CAIT detection process	116
5.3.1 Current-voltage curves.....	118
5.3.2 Measurements of ionic and electronic work function of a Leucite potassium emitter	123
5.3.3 Theoretical model	129
6 Conclusions and outlook.....	134
7 References.....	140
8 Appendix.....	153

List of figures

Figure 1: Schematic representation of the alternating adsorption of an anionic polyelectrolyte and a cationic polyelectrolyte. Figure taken from [7].....	4
Figure 2: Different steps of a dipping layer by layer technique.....	5
Figure 3: Structural formulas of an epoxy resin (top) and curing agent (bottom) Figure taken from [69].....	11
Figure 4: Schematic representation of a pellet processing protocol. Figure taken from [68].....	11
Figure 5: Step by step illustration of a transfer molding process, where a pellet-type EMC is used in order to encapsulate a semiconductor chip. Figure taken from from [70].....	12
Figure 6: Schematic of the viscosity-time/temperature relationship during EMC molding Figure taken from [70].....	12
Figure 7: Potential landscape for mobile ions along an arbitrary direction in the random energy model (schematic) schematic). Figure taken from [75].....	19
Figure 8: Fisher’s model of an isolated grain boundary. D : lattice diffusivity. D_{gb} : diffusivity in the grain boundary. δ : grain-boundary width Figure taken from [71].....	22
Figure 9: Illustration of type A, B, and C diffusion regimes in a polycrystal according to Harrison’s classification Figure taken from [71].....	23
Figure 10: Schematic illustration of a penetration profile in a bi-crystal for type B kinetics kinetics. Figure taken from [71].....	25
Figure 11: Discretization procedure. Figure taken from [14].....	27
Figure 12: (a) The backside current as a function of the kinetic energy of the ions of a membrane sample for three different blind currents I_{blind} , (b) the same information for the glass. Figures taken from [14].....	31
Figure 13: Representation of the Boundary conditions for hopping model.....	36
Figure 14: Transport of ions toward a sample and neutralization at the backside electrode.....	41
Figure 15: Representation of the evolution of the backside current via an equivalent circuit.....	41

Figure 16: Resistive and capacitive contributions of the registered backside current....	42
Figure 17: Description of the sputter process. Left: the impact of the primary ion induces a collision cascade of particles in the solid that leads to ejection of particles when returning to the surface. Right: secondary particles ejected during the sputter process. Picture taken from [138].....	44
Figure 18: Schematic construction of a ToF-SIMS instrument (picture taken from taken from Iontof’s training material).....	46
Figure 19: Illustration of an LMIG with its component Adapted from the instrument manual.....	47
Figure 20: Schematic illustration of a dual-source ion column Adapted from the instrument manual.....	48
Figure 21: Schematic with main components of the mass analyzer of the ToF-SIMS instrument Taken from the instrument manual.....	50
Figure 22: Representation of a reflector compensating for distributions of initial kinetic energies of analyzed ions: an ion entering with large kinetic energy will have a longer travel distance inside the reflectron (blue dot) than an ion with low kinetic energy (green dot).....	51
Figure 23: Schematic of a stylus profilometer Figure taken from [142].....	56
Figure 24: Diagram of the sputtering process Taken from [143].....	57
Figure 25: Sketch of the charge attachment induced transport (CAIT) setup.....	58
Figure 26: The assembly of ion sources is presented on the left [139], while the electric circuit diagram on the right.....	60
Figure 27: Pictures of the emitter type b is presented on the left, while the electric circuit diagram on the right.....	61
Figure 28: Representation of cationic polyelectrolyte (PAH) and anionic calixarene (calix8).....	67
Figure 29: Functionalization of the gold layer. The thiol group of the MPA binds to the gold surface, while the carboxylate forms, after the loss of H ⁺ , a negatively charged layer, providing the basic structure for the construction of the PEMs.....	68
Figure 30: The second step is based on the alternating adsorption of PAH and calix8..	69
Figure 31: Assembling of the mold compound sample onto a copper electrode via a heat conducting glue.....	70

Figure 32: Backmount holder (left) and topmount holder (right) Pictures taken from the instrument manual.....	71
Figure 33: Time dependence of the backside current for an MCP1 sample at 30 V and 170 °C.....	74
Figure 34: Temperature dependent current–voltage characteristic of the sample MCP1.....	74
Figure 35: Temperature dependence of the specific conductivity for MCP1 sample.....	76
Figure 36: Temperature dependence of the specific conductivity for different reproduction measurements of the MCP1.....	77
Figure 37: Temperature dependence of the specific conductivity for an MCP4 measured daily for 5 days while permanency under vacuum conditions.....	78
Figure 38: Temperature dependence of the specific conductivity. Data according to EIS and CAIT methods for samples MCP1 (a), MCP2 (b) and MCP3 (c).....	80
Figure 39: ToF-SIMS of the MCP3 sample bombarded with a K^+ ion beam of kinetic energy of 19 V. Signal: black squares for $^{39}K^+$ (bombarder ion), blue crosses for SiO^+ (representative of the MCP).....	81
Figure 40: ToF-SIMS of the MCP3 sample bombarded with a K^+ ion beam of kinetic energy of 19 V. Left: K^+ , Na^+ , F^+ , SiO^+ , SiF^+ and $SiCl^+$ depth profile in linear scale. Right: same depth profiles in logarithmic scale.....	82
Figure 41: ToF-SIMS of the MCP3. Left: K^+ , Na^+ , F^+ , SiO^+ , SiF^+ and $SiCl^+$ depth profile in linear scale. Right: same depth profiles in logarithmic scale.....	83
Figure 42: plot of the logarithm of the $^{39}K^+$ signal versus the squared depth.....	85
Figure 43: Chemical maps for SiO^+ (a) and C^+ ion signal (b), i.e. a top view of the signals integrated into the z-direction.....	86
Figure 44: top view of the K^+ signal (c) integrated in the z-direction.....	86
Figure 45: 3D images of potassium. Left: whole 3D cuboid visualization. Right: same 3D cuboid with a cut of the 10% along the z-direction.....	87
Figure 46: SEM image of an MCP3 fresh film.....	88
Figure 47: Ion density vs depth from experimental data (black), simulated mixed pathway diffusion (red), simulated sole bulk diffusion (green) and simulated sole grain boundary diffusion (blue).....	90

Figure 48: Current-voltage characteristic of a (PAH/calix8) ₃₀ under the influence of the substrate.....	92
Figure 49: Temperature dependence of the ionic conductance under the influence of the substrate. A value of activation energy of 1.025 eV ± 0.04 eV has been calculated from the slope.....	93
Figure 50: Representation of the conductance G vs. number of bilayers (left) and temperature dependence of the conductance (right) under the influence of the substrate.....	94
Figure 51: E _{act} of (PAH/calix8) _n with n = 1, 3, 6, 9, 12, 15, 20, 30 under the influence of the substrate	94
Figure 52: Illustration of the construction Design I in the case of a desired final system (left) and an undesired scratching of the lateral coverage of chromium (right).....	97
Figure 53: Top view of a fresh gold-sputtered steel substrate (a), a PEM-functionalized sample (b) and the same sample after some days into storage (c).....	98
Figure 54: Current–voltage characteristic for (PAH/calix8) ₉ at a temperature range from 70 °C to 100 °C. Black stars rely on the input current measured in the same range of voltages.....	99
Figure 55: Current–voltage characteristic for (PAH/calix8) ₉ in a temperature range from 70°C to 100 °C. Pink triangles rely on the measured backside corresponding to an ion beam with heating current of 6200 mA instead of 5800 mA.....	100
Figure 56: Ellipsometry measurements conducted onto (PAH/calix8) _n with n = 3, 6, 9, 12, 15, 20 and 30 (*original raw data from the analysis conducted in Hamburg).....	102
Figure 57: Concentration profiles of the bombarded (PAH/calix8) ₁₅ . The ion signals are normalized to maximum ion signal of the corresponding species. Left: depth profile for 1 hour long-time bombardment. Right: depth profile for 300 sec long-time bombardment.....	103
Figure 58: Depth profiles of position B (left) and position C (right) taken from a fresh sample of (PAH/calix8) ₁₅ . In both cases fragments of the film were taken as reference for the PEM layer.....	104
Figure 59: (PAH/calix8) ₁₅ picture with visible inhomogenous spots (left); picture taken by a ToF-SIMS camera showing the same inhomogeneity in microscale (right).....	105
Figure 60: Plots of ion densities vs depth for [Li ⁺ , K ⁺ , Rb ⁺]@(PAH/calix8) ₃₀ after bombarding time of 5 seconds (a) and 100 seconds (b).....	107

Figure 61: Ion density versus depth of experimental data (light blue), simulated slow pathway diffusion (red) and fast pathway one (green) together with total contribution (blue).....109

Figure 62: Ion density versus depth of experimental data (light blue) and simulated curves from different calculation test. More details regarding the appendix are given in the text.....111

Figure 63: Ion density versus depth. Experimental data (pink dots) and numerical data (simulated till 40nm plus Lorentz distribution) are plotted.....113

Figure 64: Ion density versus depth of experimental data (magenta symbols) and simulated curves from different calculation test. More details regarding the appendix are given in the text.....114

Figure 65: Schematic graph of a generic I_{back} vs U_{rp} curve. The intercept with the x-axis represents the offset voltage.....116

Figure 66: Sketch of the experimental setup for measuring thermionic ion currents. The upper graph shows the electrical circuit. The bottom graph shows pictures of the set up.....118

Figure 67: Normalized ion current vs voltage plots of different measurements. A gold electrode was used as metal detector plate.....119

Figure 68: Evaluation of the experimental U_{offset} from the linear fit of the curves. Listed in table 9 the values for each reproduction measurement as well as the average value of $U_{offset,exp}$120

Figure 69: Normalized ion current vs voltage plots of different measurements. A steel electrode was used as metal detector plate. Listed in table 10 the values for each reproduction measurement as well as the average value of $U_{offset,exp}$120

Figure 70: Normalized ion current vs voltage plots of different measurements after treating the surface of the electrode (both gold and steel data shown). Listed in table 11 the values for each reproduction measurement as well as the average value of $U_{offset,exp}$122

Figure 71: Ion current vs voltage curves for different heating current. A gold electrode was used as metal detector plate.....123

Figure 72: Representation of the ion current density as a function of the temperature.....124

Figure 73: Evaluation of the ionic work function W_{ion} , from the slope of the linear fit of the curve.....125

Figure 74: Evaluation of data for determining the work function according to Richardson-Dushman. Measurement: REP I (reproduction I).....126

Figure 75: Evaluation of data for determining the work function according to Richardson-Dushman. Measurement: REP II (reproduction II).....126

Figure 76: Evaluation of data for determining the work function according to Richardson-Dushman. Measurement: REP III (reproduction III).....126

Figure 77: Evaluation of data for determining the e- work function according to Richardson-Dushman measurement: REP I (reproduction I).....127

Figure 78: Evaluation of data for determining the e- work function according to Richardson-Dushman. Measurement: REP II (reproduction II)..... 127

Figure 79: Evaluation of data for determining the e- work function according to Richardson-Dushman measurement: REP III (reproduction III).....128

Figure 80: Evaluation of data for determining the e- work function according to Richardson- Dushman measurement: REP IV (reproduction IV).....128

Figure 81: Sketch of the relevant distances and the energy landscape for the thermionic emission and detection of K^+ ions from a $KAlSi_2O_6 : Mo$ (1:9) emitter.....129

Figure 82: Simple illustration of the emitter filament-type (left) and pellet-type (right). Arrows indicate the hypothetical emission of species (ions and e-), whereas encircled indicate only the emission which occur in the two cases respectively. More details in text.....131

List of tables

Table 1: A graphic representation of the different types of substrates used. On the left column a cut-side view of the PEM-coated substrate; on the right column the same view but after mounting the sample on the sample holder.....	65
Table 2: Building blocks for the preparation of PEMs.....	67
Table 3: List of samples produced within the study of this thesis.....	69
Table 4: Composition of the mold compounds.....	70
Table 5: Values of conductance G and conductivity σ evaluated from the slope of the linear regression of figure 34.	75
Table 6: Activation energy values evaluated for the same type of mold compound MCP1.....	77
Table 7: evaluated activation energies from the slope of the linear regression of curves of fig. 38.....	80
Table 8: Main fragments taken as reference of the PEMs. Nominal mass, experimental mass at which the peak has been found and the location of origin of the fragment are listed in table.....	106
Table 9: Charge accumulated for $[Li^+, K^+, Rb^+]@(PAH/calix8)_{30}$ after bombarding time of 5 seconds and 100 seconds.....	108
Table 10: the values for each reproduction measurement, as well as the average value of $U_{offset,exp}$	120
Table 11: the values for each reproduction measurement, as well as the average value of $U_{offset,exp}$	120
Table 12: the values for each reproduction measurement, as well as the average value of $U_{offset,exp}$	122
Table 13: Summary of the results of the linear regressions from the figures 72-74....	127
Table 14: Summary of the results of the linear regressions from the figures 75-78....	128
Table 15: Data for the evaluation of the U_{Offset} , according to the equation (68).....	130
Table 16: Electronic work function for the different elements mentioned.....	132

Abbreviations

(PAH/calix8) _n	polyelectrolyte multilayers made of <i>n</i> bilayers of PAH and calix8
2D	two dimensions
3D	three dimensions
CAIT	Charge Attachment Induced Transport
calix8	p-sulfonato-calix[8]arene
CMM	Capillary Membrane Model
CPUs	Central Processing Units
DSC	Dual-Source Column
e.g.	exempli gratia
EIS	Electrochemical Impedance Spectroscopy
EMC	Epoxy Mold Compound
<i>et al.</i>	and others
Fig.	Figure
GB	Grain Boundary
HMM	Homogeneous Membrane Model
IS	Impedance Spectroscopy
K@gold	bombardment of potassium ions on gold
K@steel	bombardment of potassium ions on steel
KAlSi ₂ O ₆ :Mo(1:9)	composition of a Leucite potassium emitter
LbL	Layer-by-Layer deposition technique
LiAlSi ₂ O ₆	synthetic spodumene
LMIG	Liquid Metal Ion Gun
M[AlSi ₂ O ₆]	aluminosilicate with (M = K, Rb)

M@(PAH/calix8) ₃₀	bombardment of M ⁺ on (PAH/calix8) ₃₀
MCP	Mold Compound
MPA	3-Mercaptopropionic Acid
NPP	Nernst-Planck-Poisson
OP	Operational Amplifier
PAH	Poly(allylamine hydrochloride)
PEMs	Polyelectrolyte Multilayers
PPX	Poly-para-xylylene
PSS	Polystyrenesulfonate
TDC	Time to Digital Converter
ToF-SIMS	Time-of-Flight Secondary Ion Mass Spectrometry

Symbols and physical constants

A	bombarded area
D	diffusion coefficient or diffusivity
D_{gb}	grain boundary diffusion coefficient
E	applied field $E = U / d$
e	elementary charge [$e = 1.602176465 \cdot 10^{-19}$ C]
E_{act}	activation energy
E_f	Fermi level
G	conductance [S]
$I.E.$	ionization energy of an element [eV]
I_{back}	registered backside current
I_{blind}	ion current that reaches the sample surface
I_C	capacitive current
I_{max}	current at the beginning of a discharging process
I_p	primary ion current
I_R	resistive current
I_{sat}	saturation level of the current
J_{input}	ion flux density deposited at the sample
J_{blind}	ion flux density that reaches the sample surface
J_x	flux of particles (diffusion flux)
k	material constant
k_B	Boltzmann's constant [$k_B = 1.3806503 \cdot 10^{-23}$ JK ⁻¹]
m	ion mass
m	slope of the recorded current-voltage characteristic

m/z	mass/charge ratio
M^+	alkali ions
Q	charge incorporated [C]
R	resistance of the sample
T	temperature [°C]
U_{offset}	voltage offset
U_{rp}	kinetic energy
v	ion velocity
W	work function
Y_m	sputtering yield
Z_e	charge of the ionic species
α	ionization probability
δ	grain boundary width
ϵ_0	dielectric constant of vacuum [$\epsilon_0 = 8.854187817 \cdot 10^{-12} \text{ F m}^{-1}$]
ϵ_r	relative dielectric constant
η	transmission of the analyzer
σ	specific conductivity [S/cm]
σ_0	pre-exponential factor
τ	time constant
Φ	electric potential

1 Introduction and motivation

The research in material science has seen a huge step forward over the last decades: on the one hand there was the request of new high performance materials in different areas such as drug delivery, precise environmental sensors or synthetic polymer based coatings for various industrial applications; on the other hand, more relevance was given to the demand on improving the performance, multifunctionality, integration, and sustainability of those materials. Within these topics, the focus of the worldwide scientific environment has been the construction of structured hybrid systems, based upon synthetic or natural polymers combined with metal, ceramic, carbon or natural structures: the ability to create structured materials both on macro and nanoscale has become an important field of research with applications in a variety of areas.

Despite the different fields of applications, the issue of ion transport appears to be a key factor for different classes of materials. Beyond the mere technical challenges, there are important scientific questions relating to ion transport in the bulk and at interfaces. There is a considerable number of experimental methods available for characterizing the dynamics and transport of ions, e.g. impedance spectroscopy (IS), solid-state NMR techniques, pulsed field gradient NMR (PFG-NMR) and tracer diffusion (RTD). Within the mentioned, IS is one of the most commonly used technique, however, it relies on a well-defined electrical contact between the sample and two electrodes. This aspect can envisage situations where a sample contact with two electrodes is not possible or not desirable. An alternative to the IS is the recently developed charge attachment induced transport (CAIT) technique. This technique is based on the use of only one electrode and it has been applied to a variety of solid electrolyte materials, such as ion conducting glasses [1, 2, 3, 4] and polymers [5, 6, 7]. Bearing in mind the previous points, material such as polyelectrolyte multilayers and mold compounds found an extended interest in the scientific community. Despite the fact that these two classes of materials have different fields of applications, it is worth noting that the issue of ion transport appears to be a key factor for both cases.

Mold compounds are highly filled epoxy resins used to encapsulate electronic devices such that the device is protected against mechanical, environmental and chemical attacks. Mold compounds used for chip encapsulation are one of the main contamination sources for mobile ions in semiconductor devices. These ions are a prominent reliability

risk, especially, when it comes to high power devices such as high voltage transistors. Due to strong electrical fields, ions from the mold compound can migrate into sensitive areas of these devices resulting in chip failure. The issue of ion contamination represents a well-known concern [8]: these materials indeed cannot be totally free from mobile ions in trace amount. Provided that the issue of ion contamination represents a well-known concern in the field of electronic packages, the analysis conducted within this study aims to investigate ion diffusion in microcircuit encapsulation materials, e.g. mold compounds. The samples used for the study of this work are of four types (MCP1, MCP2, MCP3 and MCP4). Previous publications presented analytical techniques to investigate ion diffusion in mold compounds [9, 10]. Schwab *et al.* described a method to evaluate the risk of field induced ion migration in different molding compounds depending on the temperature and field strength. This method allows the qualitative and quantitative determination of ion mobility in mold compounds, without the interference of electron conductivity. They describe furthermore a new approach to measure field induced ion migration in mold compounds using a sodium amalgam electrode [11, 12]. Within the study of this thesis, investigation of ion diffusion in microcircuit encapsulation materials, e.g. mold compounds, has been performed *via* a combination of charge attachment induced transport technique (CAIT) and time-of-flight secondary ion mass spectrometry (TOF-SIMS). Qualitative and quantitative analysis have been performed in order to provide meaningful information on the transport properties of potassium ions through the specific mold compounds.

Polyelectrolyte multilayers (PEMs) represent a class of materials used as multi-purpose membranes for water softening and seawater desalination [13, 14], for purification of water and ethanol from organic pollutants such as phenols and aromatic hydrocarbons [15], for conductive coatings [16] and patterning [17, 18]. One of the main aspects is that PEMs have also shown promising applications as selective membranes for the immobilization of macromolecules or particles [19] and for the controlled transport and release of small molecules [20]. In order to link this generic argument with a more specific attempt in understanding ions transport properties across PEMs, the work described in this thesis gives a multiple-level analysis on the transport of alkali ions (Li^+ , K^+ , Rb^+) through PEMs prepared from layer-by-layer assembly of ionic calixarenes and cationic poly(allylamine hydrochloride) (PAH). The reason why this model system has been used is that calixarenes are important building blocks in supramolecular chemistry;

they represent one of the most important macrocyclic host molecules [21] together with crown ethers and cyclodextrins. Because of their basket shape, they are suited for the complexation of small molecules and ions. Regen and co-workers [22, 23] prepared Langmuir and Langmuir-Blodgett films of well-ordered amphiphilic calixarene derivatives and used these films for gas-permeation studies. Swanson and co-workers [24] described multilayer films of polyelectrolyte/calixarene, which were used as chemically selective layers for organic-vapor detection. In other words, these membranes exhibit high selectivities in the rejection of specific ions, due to the specific interactions with the unit rings. Ion transport across PEMs containing calixarenes has been investigated by Toutianoush *et al.* [25] where p-sulfonato-calix[n]arene / poly(vinylamine) (PVA) multilayers were used as model system and the permeation rates of various electrolytes in aqueous solution were given; there the author verified that permeation of the metal ions across the calixarene/polyelectrolyte multilayer films is retarded compared with the all-PEM membranes, i.e. membranes without ring units from calixarenes. Within the work of this thesis PEMs have been analyzed by means of the charge attachment induced transport technique (CAIT) as first step of the analysis; in the second part of the analysis the samples were investigated via time-of-flight secondary ion mass spectrometry (TOF-SIMS); in the final level of the analysis numerical calculations have been conducted and a theoretical model has been established in order to provide qualitative and quantitative information on the ion transport properties of these membranes.

After considering the motivations beyond the project of this thesis, a brief overview of the main sections will be given here: section 2 will describe the theoretical background with respect to the materials used and to the process of ion transport in condensed matter. Subsequently, a description of the techniques used (CAIT and ToF-SIMS) will be presented in section 3. The entire experimental part consisting of preparation of samples and building up of set up, will be described in section 4. Finally, in section 5 a discussion of the results obtained for mold compounds (section 5.1) and PEMs (section 5.2) will be given, together with an extra discussion connected with the electronic properties of the CAIT method (section 5.3), whose motivations will be highlighted in the relevant section.

2 Theoretical background

2.1 Polyelectrolyte multilayers

Polyelectrolyte multilayers play an important role in a lot of technological applications, including molecular capsules [26], immobilization of enzymes [27], patterning of surfaces [28], preparation of light-emitting diodes [29], photoelectrochemically active electrodes [30], membranes [31], microporous [32] and erodible films [33]. Among several methods to obtain multilayers, a simple and versatile approach is the layer-by-layer (LbL) deposition, that was used for the first time by Iler [34] in 1966 in the case of colloidal particles, and then extended in the case of polymers (polyelectrolytes in particular) in 1991 by Decher and Hong [35, 36]. The thorough review of various types of multilayers and their applications can be found in the book edited by Decher and Schlenhoff [37]. The LbL technique has become one of the most used methods for surface functionalization [38] because it allows obtaining uniform films with a well-defined thickness. The formation of polyelectrolyte multilayers can be explained considering an overcompensation mechanism (figure 1): if a surface is positively charged, then a negative polyelectrolyte can be easily adsorbed on it, making the surface negatively charged in turn and allowing the subsequent absorption of a positive polyelectrolyte [39]:

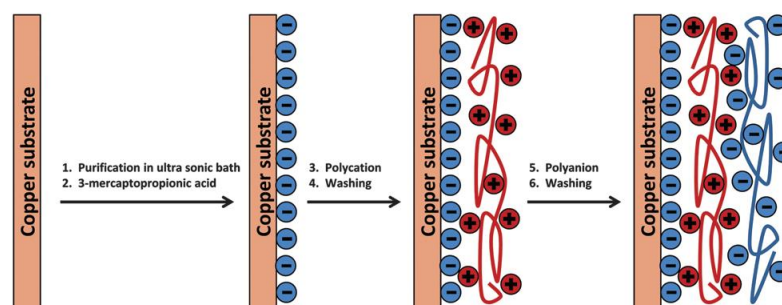


Fig.1: Schematic representation of the alternating adsorption of an anionic polyelectrolyte and a cationic polyelectrolyte. Figure taken from [7].

There are two different effects that allow the growth of a polyelectrolyte membrane: the first is due to the electrostatic forces with short-range (van der Waals forces, hydrophobic forces) that occurs between polyelectrolytes having different charges. The second effect

is a favourable entropic contribution due to the release of counterions during the absorption process both from the surface and from polyelectrolyte chains. During formation of each polyelectrolyte layer, the polyions in the bulk are electrostatically attracted by the oppositely charged polyelectrolytes constituting the uppermost layer of the film in construction. This adsorption process, driven by the electrostatic interactions and by the gain in entropy from the release of polyelectrolyte counterions and the partial removal of the hydration shell around ionized groups, leads to charge overcompensation at the interface [40]. It is necessary to point out that the condition of overcompensation causes the electrostatic repulsion of the polyelectrolyte in excess and limits the adsorbing layer to a monolayer coverage. After the first layer formation, the surface is rinsed with pure buffer and the film is brought into contact with the polyelectrolyte solution of opposite charge, which starts a new deposition step (figure 2):

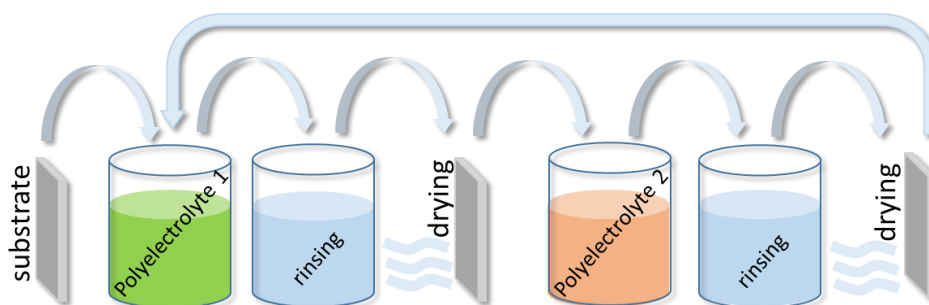


Fig. 2: Different steps of a dipping layer by layer technique.

The stable polyelectrolyte multilayer films could exhibit two basic regimes of growth with the number of deposition cycles: linear or exponential [41, 42]. It is known that the conformation of chains is a key aspect in multilayer growth [43], and it is generally determined not only by intrinsic properties such as chain length [44] but also by other factors such as pH and ionic strength of the solution [45, 46].

With regard to the build-up process, several issues are currently under debate. For instance, it is not well known to what extent the excess of charge is distributed on the surface: some studies attribute it to the first few layers under the surface [47, 48], while others attribute it to the molecule–molecule and molecule–surface charge overcompensation [49, 50]. Another aspect that remains to be clarified concerns whether

the compensation of the internal charge is due to a 1:1 stoichiometry of the alternating polymers (“intrinsic compensation”) or to the presence of mobile salt ions (“extrinsic compensation”). In order to give a better understanding to the question of the intrinsic/extrinsic compensation, Riegler and Essler studied [51] a multilayer system based on polyallylamine / polystyrene sulfonate (PAH/PSS). In their work, they conducted a quantitative analysis with respect to the internal charge stoichiometry of the polyelectrolytes. To this end, the adsorbed amount of polymer is translated into charge per area.

$$\sum charge = \sum_j \alpha_{PAH} \Gamma_{PAH,j} - \sum_i \alpha_{PSS} \Gamma_{PSS,i} \quad (1)$$

with:

$\Gamma_{PSS,i}$ = adsorbed amount of PSS monomols/m² in layer i

$\Gamma_{PAH,j}$ = adsorbed amount of PAH monomols/m² in layer j

i = PSS layer number index

j = PAH layer number index

α_{PSS} = degree of charging of PSS

α_{PAH} = degree of charging of PAH

As postulation, they assumed that the strong acid PSS is fully negatively charged, i.e. totally dissociated ($\alpha_{PSS} = 1$) and the weak polyelectrolyte PAH as well ($\alpha_{PAH} = 1$). With both polyelectrolytes fully charged the PAH charges significantly overcompensate the PSS charges, but it turned out that the polyelectrolyte charge stoichiometry is not 1:1, and the multilayer must contain some small counterions for charge compensation. It was suggested that this “extrinsic compensation” occurs when the charge density of the polyelectrolytes exceeds a certain threshold. If the distance between the charges is less than the *Bjerrum length*, the strong binding of the counterions (so-called “Manning condensation”) prevents their release upon multilayer formation. This explains why multilayers with PAH contain counterions whereas other polyelectrolyte films are ion-free. It is generally accepted, however, that if the multilayer is immersed in an external solution with a significant salt concentration, the chemical potential of the salt forces some swelling of the multilayer thus establishing some degree of extrinsic compensation [52, 53]. In any case, the salt concentration in solution has been proven to be a crucial

experimental variable not only in controlling the build-up of the multilayers but also in determining their transport properties [54, 55, 56, 57, 58, 59].

The structure and properties of these PEMs have been extensively studied by X-ray and neutron reflectivity [60, 61], ellipsometry [51, 62], quartz crystal microbalance, scanning electron microscopy and atomic force microscopy [63]. Measurements of the ζ potential [64, 65] have shown a symmetrical oscillation from -20 mV for the anionic layer to +20 mV for the cationic layer. This indicates that during the successive deposition of PSS and PAH layers each polyelectrolyte brings with it a net charge which is, in absolute value, the same for the polyanion and the polycation and does not change during the build-up procedure. This also implies that the charge excess of the multilayer does not vary between the deposition of two consecutive PSS and PAH layers. In order to share further light onto this aspect in 2004 Morales *et al.* published a survey based on a study of a polyelectrolyte multilayers system made of polystyrene sulfonate (PSS) and polyallylamine (PAH) deposited on a gold electrode modified with cysteamine. Following the notation introduced by Silva *et al.* [66], the total number of bilayers has been denoted as:

$$N = \frac{n_{PSS} + n_{PAH}}{2} \quad (2)$$

where n_{PSS} and n_{PAH} are the number of layers of PSS and PAH, respectively. Thus, N is an integer number when $n_{PSS} = n_{PAH}$ and a semi-integer number when $n_{PSS} = n_{PAH} + 1$. The layers are numbered by a superscript running from $i = 0$ for the cysteamine layer to $i = 2N$ for the outer layer in contact with the bulk solution. Layers with even index i are positively charged and layers with odd index are negatively charged. The molar concentration of fixed charge groups takes the same value $X_i = X$ for layers $i = 0, \dots, 2N - 1$. The charge concentration in these layers can, therefore, be written as $\omega^i X$, where $\omega^i = (-1)^i$ is the charge number of the fixed groups. The concentration of charged groups in the last layer is $X^{2N} = X(1 + \alpha)$, where α is a factor describing its relative charge excess. This assumption concerning fixed charge concentration is in agreement with previous experimental findings for PSS/PAH multilayers in which the ζ potential was measured indicating always the same oscillation between ± 20 mV as mentioned before [64, 65]. In

every layer a position coordinate x^i running from $x^i = 0$ at the interface with the layer ($i - 1$) to $x^i = d$ at the interface with layer ($i + 1$) is used. The layer thickness d is assumed to be the same for all layers. The charge of the fixed groups of the polymer chains in every layer is compensated by the mobile counterions. Moreover, since the multilayers in the system under consideration are rinsed by a (moderately) concentrated solution of supporting electrolyte, some coions (i.e., mobile ions of the same sign as the fixed groups) are also present. Bearing in mind the previous points, Morales *et al.* suggested an equation which describes the local electroneutrality condition, assumed to be valid throughout the system:

$$\omega^i X^i + \sum_k z_k c_k^i = 0 \quad (3)$$

In equation 3, c_k^i denotes the molar concentration of k (with k indicating the counterions) at any position x_i within the i th layer.

Turning now to the question of the inner structure of polyelectrolyte membranes, there have been attempts in order to explain qualitatively the main process of formation for a polyelectrolyte multilayer. Although it may be true that these studies are limited in giving an explanation valid under any form of conditions or parameters, however, they provide comprehensive and reliable models for possible mechanisms. In the following section some of those mechanisms are presented. In their work [67] Barreira *et al.* refer to the *Capillary Membrane Model (CMM)* and the *Homogeneous Membrane Model (HMM)* as two plausible cases which could occur. In the first case, they claim that when only a few layers have been deposited the film is very porous such that *pinholes* may exist, so there might be areas of the substrate covered by only one or two layers. The effective coverage of the electrode for these films is small and these *pinholes* may persist during the sequential assembly of the polyelectrolyte layers, although their area is progressively reduced and they tend on the average to be further apart from each other as more layers are added. Eventually, after a certain number of layers, most of these pinholes become closed. With the *HMM* model, the PEM has been modelled as a homogeneous membrane where the increase in the number of layers leads linearly to an increase in the thickness L of the film. A different approach with respect to the two previous mechanisms

is the model suggested by Ladam *et al.* [64]. According to their idea, a multilayer film can be subdivided into three regions. The first one (I) is close to the substrate and it is typically composed of only a few layers which differ from region II due to the influence of the substrate. The second region (II) represents the *bulk*, here all anionic and cationic layers possess equal thickness and in most cases, polyanion/polycation stoichiometry is observed to be 1:1 or at least close to that value. The last region (III) is the one close to the surface of the film and it is typically composed of only a few layers. It could be described as a transition zone between the charge-compensated region II and the charged surface. The transitions between zones I and II and between zones II and III are gradual. When the film is fabricated, zone I is completed first, then as more layers are added, zones I and III will preserve their respective thicknesses, while zone II will grow.

2.2 Mold compounds

The term mold compound refers to highly filled epoxy resins used to encapsulate many types of electronic packages, from capacitors and transistors to central processing units (CPUs) and memory devices. The modern mold compounds have evolved into a complex formulation containing circa 20 raw materials and multiple processing steps, each statistically controlled to yield a uniform and predictable end product. At the most basic level, mold compounds contain five classes of raw materials:

- Organic resins: typically meltable, such as epoxy resin;
- Fillers: are non-melting inorganic materials, such as silica;
- Catalysts: accelerate the cure reaction;
- The mold release material: allows the naturally adhesive epoxy resin to come out of the mold;
- A pigment or colorant;
- Other materials, such as flame retardants, adhesion promoters, ion traps and stress relievers are added to the mold compound as appropriate.

Mold compounds have evolved over the years to keep pace with industry needs: each innovation in chips or packages design required indeed a similar change in the design of the encapsulant. In 1969, encapsulants typically were filled with fused silica at about a 68 percent w/w loading. Currently, materials are filled with 90 percent fused silica. This shift was not made for reasons of cost but driven by end-user performance requirements. Over the last decade, every raw material and process in molding compounds have been re-examined and almost all have seen major changes. With the acronym EMC (epoxy mold compounds) one refers to highly formulated products that contain epoxy resins as organic resin and the rest of the raw materials: curing agents, accelerators, fillers, flame retardants, adhesion promoters, parting agents (allows release from the mold wall after molding), pigments like carbon black and other proprietary additives. Each EMC supplier has its formulation “tricks” to tailor the properties to the application and molding process [68]. The epoxy resin most commonly used in EMC is epoxy cresol novolac resins cured with phenolic curing agents (figure 3):

2 Theoretical background

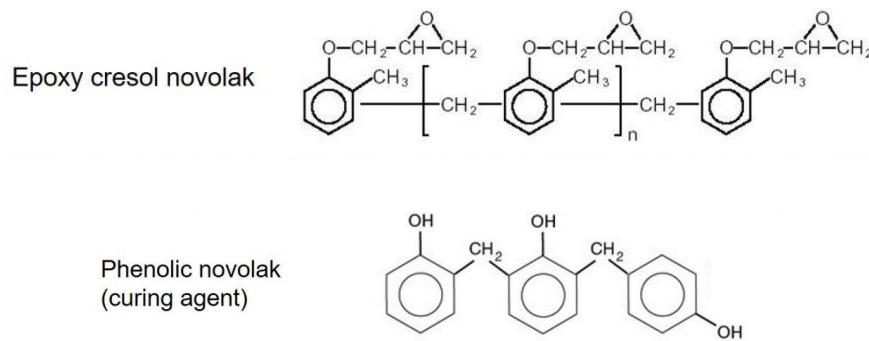


Fig. 3: Structural formulas of an epoxy resin (top) and curing agent (bottom). Figure taken from [69].

It is worth noting the main advantages in using mold compounds:

- Ease of processing with good mold filling;
- Good adhesion to lead frames, packaging substrates, and semiconductor dies;
- Acceptable chemical and moisture resistance.

The spherical silica fillers usually have a multimodal particle size distribution to allow for high filler loadings: this step increases the viscosity of the uncured resins which could have detrimental effects during the molding process; moreover, the spherical shape helps to keep the viscosity manageable during mold filling. During the processing of the pellets, the raw ingredients are mixed at an elevated temperature to soften the materials and allow good mixing in a kneader or roll mixer. The temperature is carefully controlled to control the crosslinking reaction. After the ingredients are fully mixed the mixture is cooled and ground into powder (pulverized) or into pellet form (pelletizing) (figure 4).

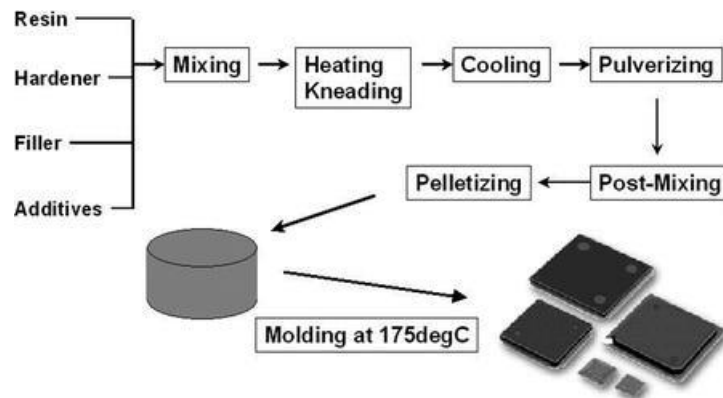


Fig. 4: Schematic representation of a pellet processing protocol. Figure taken from [68].

2 Theoretical background

The process where an epoxy mold compound is ultimately used is the *transfer molding* (figure 5). In a typical transfer molding process, a B-staged pellet is placed into a heated mold:

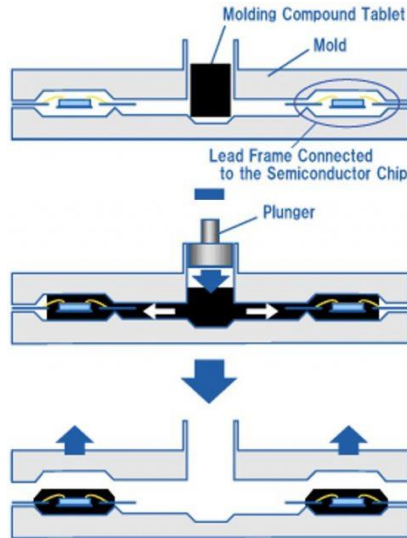


Fig. 5: Step by step illustration of a transfer molding process, where a pellet-type EMC is used in order to encapsulate a semiconductor chip. Figure taken from [70].

The mold is closed and the EMC pellet is placed into the chamber and heated to 175°C. At 175°C, the EMC softens (de-vitrifies as it goes through the T_g) and the viscosity decreases dramatically. After a specified softening time the plunger injects the now liquid EMC into the runner system. After the mold is completely filled and the specified mold time is reached, the mold is opened and the parts ejected. At the molding temperature of 175 °C, the viscosity is very low and the cavities can fill rapidly. Figure 6 shows a schematic trend of the viscosity profile during molding.

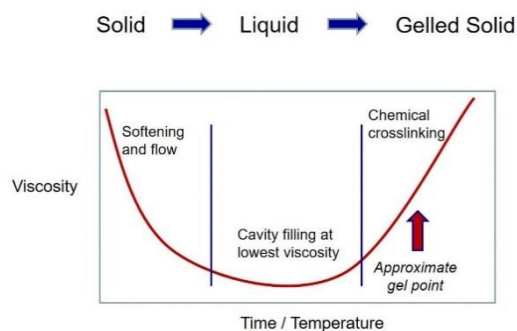


Fig. 6: Schematic of the viscosity-time/temperature relationship during EMC molding. Figure taken from [70].

2 Theoretical background

Once the mold compound fills the cavities, then the chemical crosslinking causes a rapid increase in the viscosity. In order to maximize the manufacturing throughput, the EMC is held in the mold only long enough to gel. At the gel point, the material is not fully cured but has sufficient mechanical strength to allow the mold to be opened and the part ejected. Upon cooling, the EMC is a gelled glass but the EMC is not fully cured. For typical EMC's the molding process is long enough to achieve about 40% epoxy conversion. After the molding process, the molded packages are postmold baked at 175 °C for 3 - 4 hours to achieve full cure.

2.3 Ion transport in condensed matter

Diffusion is fundamental for transport of matter and for ionic conduction in disordered materials, in particular diffusion in solids is fundamental in the art and science of materials and thus it represents an important topic of solid-state physics, physical chemistry, physical metallurgy, and materials science. The term diffusion refers to the transport of matter from one point of space to another by thermal motion of atoms or molecules and it is relatively fast in gases, slow in liquids, and very slow in solids. Diffusion plays a key role in many processes as intermixing of gases and liquids, permeation of atoms or molecules through membranes, evaporation of liquids, drying of timber, doping silicon wafers to make semiconductor devices. Direct technological applications of diffusion concern, e.g. doping during fabrication of microelectronic devices, solid electrolytes for batteries and fuel cells, surface hardening of steel through carburization or nitridation, diffusion bonding and sintering.

The atomic mechanisms of diffusion in crystalline solids are closely connected with defects. Point defects such as vacancies or interstitials are the simplest defects and often mediate diffusion in crystals. Dislocations, grain-boundaries, phase boundaries, and free surfaces are other types of defects. They can act as high-diffusivity paths (short circuits) because the mobility of atoms along such defects is often much higher than in the lattice. In solids with a structural disorder such as glasses or crystals with highly disordered sublattices, the concept of defects is no longer useful. Nevertheless, diffusion is fundamental for transport of matter and for ionic conduction in disordered material and many of the physical concepts, which have been developed for metals, apply to diffusion in all crystalline solids.

The science of diffusion in solids had its beginnings in the 19th century and it is based on several cornerstones. The most important ones are: (i) The continuum theory of diffusion originated from the work of the German scientist Adolf Fick, inspired by experiments on diffusion in gases and of salt in water performed by Thomas Graham in Scotland. (ii) The Brownian motion detected by the Scottish botanist Robert Brown, who observed small particles suspended in water migrating in an erratic fashion. This phenomenon was interpreted many decades later by Albert Einstein. He realized that the phenomenon described by Brown was a random walk driven by the collisions between

particles and the water molecules. His theory provided the statistical cornerstone of diffusion and bridged the gap between mechanics and thermodynamics. (iii) The perception of the Russian and German scientists Jakov Frenkel and Walter Schottky. According to them, point defects play an important role for properties of crystalline substances, above all for those controlling diffusion.

2.3.1 Diffusion

The equations governing diffusion processes are Fick's laws. These laws represent a continuum description and are purely phenomenological. A physical understanding of diffusion in solids is based on random walk theory and on the atomic mechanisms of diffusion. Considering the flux of diffusing particles in one dimension (x -direction), Fick's first law for an isotropic medium can be written:

$$J_x = -D \frac{\partial C}{\partial x} \quad (4)$$

Here J_x is the flux of particles (diffusion flux) and C their number density (concentration). The negative sign in equation (4) indicates opposite directions of diffusion flux and concentration gradient. The factor of proportionality, D , is denoted as the *diffusion coefficient* or as the *diffusivity* of the species considered. Since the diffusion flux is expressed in number of particles (or moles) traversing a unit area per unit time and the concentration in number of particles per unit volume, the diffusion coefficient D has units of $[\text{cm}^2 \text{s}^{-1}]$ or $[\text{m}^2 \text{s}^{-1}]$. Usually, in diffusion processes the number of diffusing particles is conserved, implying that the diffusing species neither undergoes reactions nor exchanges with internal sources or sinks [71]. For a diffusing species which obeys a conservation law an equation of continuity can be formulated:

$$\frac{\partial C}{\partial t} = -\frac{\partial J}{\partial x} \quad (5)$$

Equation (5) is denoted as the continuity equation. Fick's first law (4) and the equation of continuity (5) can be combined to give an equation which is called Fick's second law or sometimes also the diffusion equation:

$$\frac{\partial C}{\partial t} = D \frac{\partial^2 C}{\partial x^2} \quad (6)$$

From a mathematical point of view, this is a second order, linear partial differential equation. Initial and boundary conditions are necessary for particular solutions of this equation which permit the determination of D from measurements of the concentration distribution as a function of position and time. In a simple example, a thin layer of the diffusing species is considered. The diffusing species (diffusant) is deposited at the plane $x = 0$ and allowed to spread for $t > 0$.

$$C(x, 0) = M \delta(x) \quad (7)$$

M denotes the number of diffusing particles per unit area and $\delta(x)$ the Dirac delta function. This initial condition is also called instantaneous planar source. In the frame of this theory two geometries can be distinguished:

1. Sandwich geometry: If the diffusant (or diffuser) is allowed to spread into two material bodies occupying the half-spaces $0 < x < \infty$ and $-\infty < x < 0$, which have equal and constant diffusivity. The solution of equation (6) is then:

$$C(x, t) = \frac{M}{2\sqrt{\pi Dt}} \exp\left(-\frac{x^2}{4Dt}\right) \quad (8)$$

2. Thin-film geometry: If the diffuser is deposited initially onto the surface of a sample and spreads into one half-space, the solution is:

$$C(x, t) = \frac{M}{\sqrt{\pi Dt}} \exp\left(-\frac{x^2}{4Dt}\right) \quad (9)$$

These solutions are also denoted as Gaussian solutions. Note that (8) and (9) differ by a factor of 2. The quantity $2\sqrt{Dt}$ is a characteristic diffusion length.

So far have been considered only solutions of the diffusion equation when the diffusant is initially concentrated in a very thin layer. Experiments are also often designed

in such a way that the diffusant is distributed over a finite region. In practice, the diffusant concentration is often kept constant at the surface of the sample. This is, for example, the case during carburization or nitridation experiments of metals. In principle different solutions for different geometric arrangements of the sources are possible. Considering, for instance, the diffusion with constant surface concentration, the concentration at $x = 0$ is maintained at concentration $C_s = C_0/2$. The construct of the diffusion solution for a semi-infinite medium, the free end of which is continuously exposed to a fixed concentration C_s , reads:

$$C = C_s \operatorname{erfc} \left(\frac{x}{2\sqrt{Dt}} \right) \quad (10)$$

the quantity of material which diffuse into the solid per unit area is:

$$M(t) = 2C_s \sqrt{Dt/\pi} \quad (11)$$

From a microscopic point of view, diffusion occurs by the Brownian motion of atoms or molecules. As mentioned already in section 2.3, Albert Einstein in 1905 [72] published a theory for the chaotic motion of small particles suspended in a liquid. Einstein related the mean square displacement of particles to the diffusion coefficient. This relation was, almost at the same time, developed by the polish scientist Smoluchowski [73, 74]. It is nowadays called the Einstein relation or the Einstein-Smoluchowski relation.

$$D_x = \frac{\langle X^2 \rangle}{\tau} \quad (12)$$

Turning now to the question of the dependence of diffusion upon thermodynamic variables such as temperature and pressure: while diffusion in solids generally depends

rather strongly on temperature, the variation of the diffusion coefficient with pressure, at least for pressures accessible in laboratory devices, is far less striking than that with temperature. Usually, the diffusivity decreases with pressure not more than a factor of ten for pressures of 1GPa (10^4 bar). The temperature dependence of diffusion coefficients obeys the Arrhenius formula:

$$D = D^0 \exp\left(-\frac{\nabla H}{k_B T}\right) \quad (13)$$

Where D^0 denotes the pre-exponential factor also called the frequency factor, ΔH the activation enthalpy of diffusion and T the absolute temperature.

Up to now main concepts of diffusion of particles in condensed matter have been described. Considering, in particular, the conduction of ions in glasses, polymers, nanocomposites and disordered solids there is no simple, broadly accepted model but many theories have been formulated, every of which aims to give a better understanding of the process. Ion motion in disordered solids is fundamentally different from electronic conduction in crystalline solids, indeed ions are much heavier than electrons so their motion is far less governed by quantum mechanics. A standard model used to describe transport in disordered solids with ionic-type conduction assumes the existence of a random potential landscape with ions randomly distributed over the local minima (*sites*) of the potential energy, and the conduction is due to activated transitions of ions over the barriers separating these sites (figure 7):

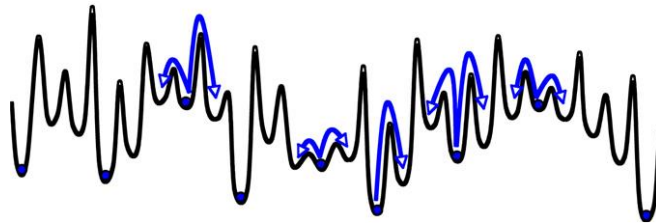


Fig. 7: Potential landscape for mobile ions along an arbitrary direction in the random energy model (schematic). Figure taken from [75].

This potential landscape is irregular and contains a distribution of depths and barrier heights, as sketched in figure 7. The varying energies result from differing binding energies at residence sites and differing saddle point energies between residence sites, and they are influenced by interactions between the ions. One refers to that as the *random energy model*. The model in which the site energies are assumed to be equal whereas the barrier heights are random is often called the *random barrier model* [76]. In figure 7 ion jumps in a disordered landscape in one dimension are illustrated. The arrows indicate attempted jumps, most of which are unsuccessful and the ion ends back in the minimum it tried to leave: if the barrier is denoted by E_{act} , T is the temperature and k_B is the Boltzmann's constant, according to rate theory, the probability of a successful jump is $\exp(-E_{\text{act}} / k_B T)$.

2.3.2 Grain boundary diffusion

In contrast to gases and liquids, crystalline solids exhibit several structurally different paths by which atomic diffusion can take place. Diffusion through crystals is promoted by atomic defects such as vacancies or interstitials. Next to them, grain boundaries, dislocations and free surfaces need to be considered as different paths. Because the diffusivity in these regions is high, the terms *high-diffusivity paths* or *diffusion short circuits* were coined to describe these very fast diffusion phenomena. Within these high-diffusivity paths, grain boundary (GB) diffusion plays an important role in many processes taking place in engineering materials at elevated temperatures. GB diffusion is important also at relatively low temperatures. In particular, the service life of many microelectronics elements and devices is limited by room temperature diffusion or electromigration of impurities along GBs resulting in the degradation of service characteristics. The fact that GBs provide high diffusivity (“short circuit”) paths in metals has been known since decades: in the 1930s mostly from indirect evidence and then in 1950s the fast grain-boundary diffusion was well documented by autoradiographic images [77], from which the ratio between diffusivity along grain-boundaries and in the lattice was estimated by Le Claire to be several orders of magnitude [78]. These observations were immediately followed by two important events: the appearance of the nowadays classic Fisher model of boundary diffusion [79], on one hand, and the development and extensive use of the radiotracer serial sectioning technique, on the other hand. During the following decades, the techniques for grain-boundary diffusion experiments have been considerably improved and extended to a wider temperature range and to a broad spectrum of materials. Most of the mathematical treatment of grain-boundary diffusion is based on the model first proposed by Fisher. According to this model, the grain boundary is represented by a semi-infinite, uniform, and isotropic slab of high diffusivity embedded in a low-diffusivity isotropic crystal [71] (figure 8). The grain boundary is described by two physical parameters: the grain boundary width δ and the grain boundary diffusivity D_{gb} , which depends on the grain boundary structure. It is widely accepted value for grain-boundary width of the order of an interatomic distance $\delta \approx 0.5$ nm.

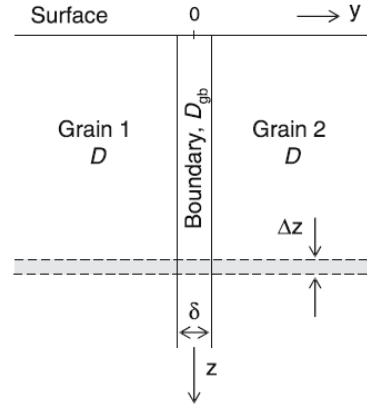


Fig. 8: Fisher's model of an isolated grain boundary. D : lattice diffusivity.

D_{gb} : diffusivity in the grain boundary. δ : grain-boundary width. Figure taken from [71].

Mathematically, this diffusion problem can be described by applying Fick's second law to diffusion inside the grains and inside the grain-boundary slab. For composition-independent diffusion coefficients it is valid:

$$\frac{\partial c}{\partial t} = D \left(\frac{\partial^2 c}{\partial y^2} + \frac{\partial^2 c}{\partial z^2} \right) \quad \text{for } |y| \geq \delta/2 \quad (14)$$

$$\frac{\partial c_{gb}}{\partial t} = D_{gb} \left(\frac{\partial^2 c_{gb}}{\partial y^2} + \frac{\partial^2 c_{gb}}{\partial z^2} \right) \quad \text{for } |y| < \delta/2 \quad (15)$$

Grain boundary diffusion is a complex process which involves diffusion from the source, diffusion along the grain boundary, leakage of the diffuser from the grain-boundary and perhaps subsequent lattice diffusion into fringes around the grain boundary. Depending on the relative importance of the various elementary processes, different diffusion kinetics (or diffusion regimes) can be observed. Each regime prevails in a certain domain of annealing temperatures, annealing times, grain sizes, lattice and grain-boundary parameters. Figure 9 shows Harrison's classification of the diffusion kinetics, which introduces three regimes called type A, B, and C [80]. In the following subsections, the three types of regimes will be discussed in details.

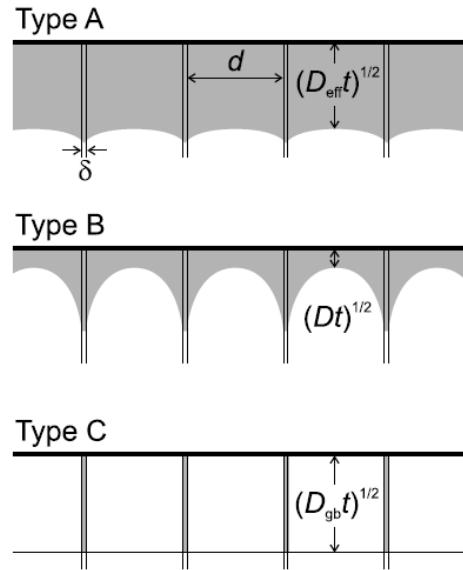


Fig. 9: Illustration of type A, B, and C diffusion regimes in a polycrystal according to Harrison's classification. Figure taken from [71].

Type A: This kinetics is observed after diffusion anneals at high, or/and with long annealing times, or/and in materials with small grain size. Lattice diffusion length, \sqrt{Dt} , need to be only a little larger than the spacing d between grain boundaries:

$$\sqrt{Dt} \geq d/0.8 \quad (16)$$

In that case, the diffusion fringes around neighbouring grain boundaries overlap and a diffusing atom may visit many grains and grain boundaries during a diffusion experiment. This results in an almost planar diffusion front with a penetration depth proportional to \sqrt{t} . From a macroscopic point of view, the polycrystal obeys Fick's law for a homogeneous medium with some effective diffusion coefficient D_{eff} . The latter represents a weighted average of the lattice D and grain-boundary D_{gb} .

$$D_{eff} = gD_{gb} + (1 - g)D \quad (17)$$

In equation (18) the quantity g is the fraction of atomic sites in the grain boundary of the polycrystal, which can be written as:

$$dg = \frac{q\delta}{d} \quad (18)$$

where q is a numerical factor depending on the grain shape. For example, $q = 1$ for parallel grain boundaries and $q = 3$ for cubic grains.

Type B: This kinetics emerges after diffusion anneals at lower temperatures, or/and with relatively short annealing times, or/and in materials with sufficiently large grain size. Under such conditions, the bulk diffusion length, \sqrt{Dt} , can become much smaller than the spacing d between grain boundaries. Simultaneously, the width of the grain-boundary fringes, which is given by \sqrt{Dt} , can be considerably larger than the grain-boundary width δ . Thus, the conditions for type B kinetics are:

$$\sqrt{Dt} \ll d \quad (19)$$

In this regime, grain-boundary fringes develop by out-diffusion from the boundaries. In contrast to the type A regime, the lattice diffusion fringes of neighbouring grain boundaries do not overlap. In a grain-boundary diffusion experiment, the overall penetration profile consists of two parts shown schematically in figure 10. First, a near-surface part due to the direct lattice diffusion from the surface. This part extends to about $(3 \text{ to } 4) \times \sqrt{Dt}$, and the concentration in this region follows either a Gaussian or an error function depending on the surface condition. Second, a deep penetrating grain boundary tail due to the simultaneous diffusion inside grain-boundaries.

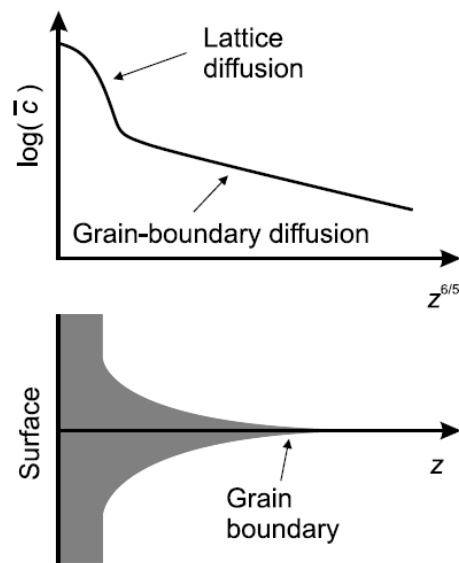


Fig. 10: Schematic illustration of a penetration profile in a bi-crystal for type B kinetics. Figure taken from [71].

Type C: Type C kinetics corresponds to conditions where diffusion through the bulk is practically 'frozen in'. Then, diffusion takes place along grain boundaries only, without any essential leakage into adjacent grains. This situation can be matched in diffusion anneals at sufficiently low temperatures and/or for very short diffusion times.

2.3.3 Electrodiffusion

One of the methods used within the work of this thesis is the CAIT technique (whose details will be given in the next sections 3.1). This technique is based on the bombardment of the sample surface with a metal ion beam. There, ion bombardment causes and defines a surface potential due to which the ions are transported through the material under analysis and detected as a neutralized current at the backside of the sample. From a theoretical point of view, the framework suited best for describing the ion transport under the conditions of a CAIT experiment is that of the coupled Nernst-Planck-Poisson (NPP) equations in its time dependent form. This set of equations, indeed, allows describing the diffusion and the migration of the ions under the influence of a concentration gradient and an electric potential gradient. In the framework of the Nernst-Planck theory, the ion flux density J is given by [81]:

$$J_\nu = -D_\nu (\nabla n_\nu + n_\nu \nabla \phi \frac{Z_\nu e}{k_B T}) \quad (20)$$

where ν is the index of the ion species with the respective diffusion coefficient, D_ν . The two terms inside the brackets introduce the diffusion *via* the ion density gradient, n_ν , and the migration induced transport via the potential gradient, $\nabla \phi$. The ion density, n_ν , takes into account any mobile ions that are in the sample already prior to the ion bombardment, $n_{\nu,bg}$ (“bg” stands for background ions), as well as ions that are injected into the sample due to the bombardment, $n_{\nu,bomb}$: $n_\nu = n_{\nu,bomb} + n_{\nu,bg}$. The charge of the ionic species is given by $Z_\nu e$, where Z_ν is an integer and e the elementary charge. Boltzmann’s constant is given by k_B and T is the temperature.

The time dependence of the ion transport is introduced by Fick’s second law:

$$\frac{\partial n_\nu}{\partial t} = -\nabla J_\nu \quad (21)$$

accounting for the mass conservation condition. The electrical potential is defined by the ion distribution and the boundary conditions that account for the experimental conditions. Hence, the potential and the ion distribution must be calculated self-consistently via the Poisson equation:

$$\varepsilon_0 \nabla[\varepsilon(\vec{r})\nabla\phi] = -e \sum_v Z_v (n_v - n_{v,bg}) \quad (22)$$

where the vacuum dielectric permittivity is given by ε_0 and the dielectric function by $\varepsilon(\vec{r})$. Because of the numerical complexity to solve this set of NPP equations, a cylindrical symmetry of the system has been taken into account:

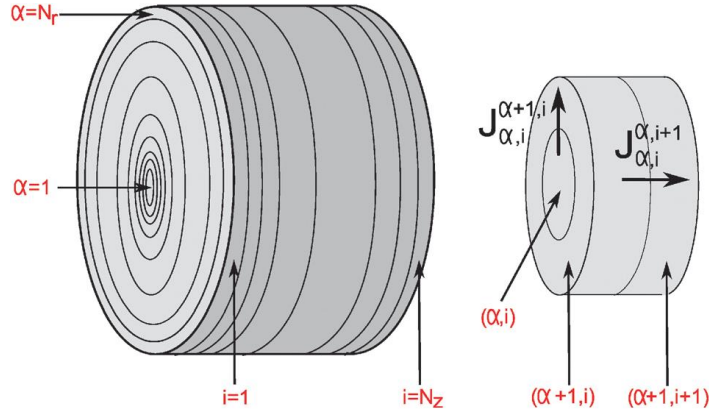


Fig. 11: Discretization procedure. Figure taken from [3].

The sample is discretized in volume elements (α, i) as depicted in figure 11. It is further assumed that the sample is isotropic such that its dielectric function $\varepsilon(\vec{r})$ simplifies to a dielectric constant, ε_r , and the diffusion coefficient is spatially constant all over the bulk sample. Consequently, we only have to consider transport along the main cylinder axis and transport in a radial direction. Angular transport does not contribute. Furthermore, if the thickness of the sample is exceedingly smaller than its radius, eventually also radial transport can be neglected. With these simplifications, equations (20), (22) and (21) become:

$$\vec{j} = J_r \vec{e}_r + J_z \vec{e}_z = -D \left(\left[\frac{\partial n(r,z)}{\partial r} + n \frac{Ze}{kT} \frac{\partial \phi(r,z)}{\partial r} \right] \vec{e}_r + \left[\frac{\partial n(r,z)}{\partial z} + n \frac{Ze}{kT} \frac{\partial \phi(r,z)}{\partial z} \right] \vec{e}_z \right) \quad (23)$$

$$\epsilon_0 \epsilon_r \left[\frac{1}{r} \frac{\partial}{\partial r} \left(r \frac{\partial \phi(r,z)}{\partial r} \right) + \frac{\partial^2 \phi(r,z)}{\partial z^2} \right] = -Ze(n(r,z) - n_{bg}) \quad (24)$$

$$\frac{\partial n}{\partial t} = - \frac{\partial J_z}{\partial z} - \frac{1}{r} \frac{\partial}{\partial r} (r J_r) \quad (25)$$

where J_r and J_z are the radial and axial components of the ion flux vector and r and z are the radial and the axial coordinates, respectively. In order to solve these equations, further information on the potential at the boundaries of the sample is needed, in particular as the Poisson equation is a differential equation of the second order, two boundary conditions obtained from the experimental arrangement are needed. The first boundary condition regards the backside of the sample, where the potential at the rear end of the sample is supposed to be zero, $\phi_{\alpha, N_z} = 0$. The second condition stems from the continuity of the normal component of the electric displacement vector at the position of the front surface of the sample at $z = 0$. In this specific point the ion speed results:

$$v_0 = \sqrt{\frac{2ZeU_{rp}}{m}} \quad (26)$$

Due to the finite kinetic energy of the impinging ions, the potential at the sample surface may never exceed $\phi_{surf}^{max} = U_{rp}$. Once the surface potential has reached this value, excess ions are repelled or stopped in front of the sample. The maximum value of the surface potential also implies that the ion flux density through the sample is limited to a value given by:

$$J_{sample}^{max} = \frac{U_{rp}}{ZeAR} \quad (27)$$

where A is the bombarded area and R is the actual resistance of the sample for DC ion transport. Considering now two different cases:

case (a)

$$J_{blind} < J_{sample}^{max} \quad \Phi_{surf} < U_{rp} \quad (28)$$

case (b)

$$J_{blind} > J_{sample}^{max} \quad \Phi_{surf} = U_{rp} \quad (29)$$

with J_{blind} being the ion current that reaches the sample surface. In the first case (a) ions are deposited at the sample, the sample starts to charge and a surface potential builds up which slows the movement of the ions. Assuming a homogeneous ion beam and neglecting radial movement, the speed of the ions in front of the sample is a function of position and depends on the local potential, Φ_z :

$$v(z) = \sqrt{\frac{2Ze(U_{rp} - \Phi(z))}{m}} \quad (30)$$

The reduction of the ion speed leads to an accumulation of ions density such that a space charge zone forms. Under this condition, the steady-state ion flux density is given by:

$$J_z(z) = nv(z) = const. \quad (31)$$

However, the accumulation of charges remains small such that in all cases considered the potential varies (almost) linearly in front of the sample and the potential in front of the sample may be described as:

$$\phi(z) = \frac{\phi_{surf}}{d} (z + d) \quad (32)$$

where d is the distance between the aperture and the sample surface. The corresponding electric field in front of the sample is then:

$$E = \frac{\phi_{surf}}{d} \quad (33)$$

Considering the second case (b) the surface is charged until the surface potential and the repeller voltage become equal. Due to the high mobility of the ions in the vacuum, most of the excess ions are radially deflected such that again a significant space charge zone cannot be established. Consequently, the field in front of the sample will be similar to the case (a) and a linear potential gradient is obtained. In the steady state, as many ions may reach the sample surface as ions are discharged at the backside electrode such that the ion flux density deposited at the sample, J_{input} , equals the maximum flux density through the sample, J_{sample}^{max} .

In a previous study [3] the theory outlined above has been applied to polymer membranes as well as ion-conducting glasses, being able to predict the tendency of the backside current for both cases. At low kinetic energies, the surface is charged up to U_R as already discussed above. As long as the blind current is sufficiently large the surface potential rises linearly with increasing kinetic energy. The front potential eventually saturates at a level that is determined by the value of the blind current.

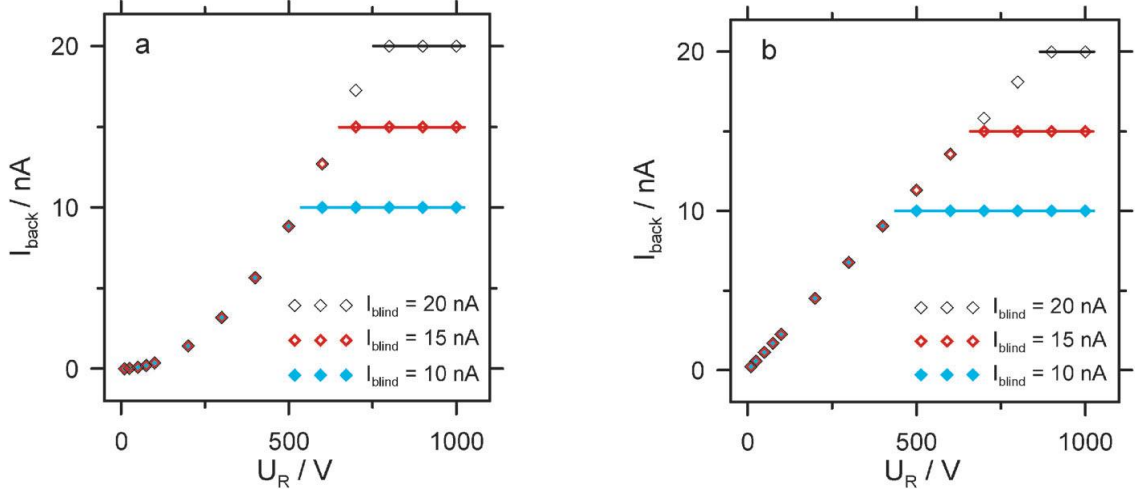


Fig. 12: (a) The backside current as a function of the kinetic energy of the ions of a membrane sample for three different blind currents I_{blind} , (b) the same information for the glass. Figures taken from [3].

Figure 12 shows the current at the backside of the membrane (a) and the glass sample (b), respectively, under comparable conditions. Evidently, in the glass sample the backside current increases linearly with the ion kinetic energy until the saturation level is reached. This saturation level, termed as I_{sat} , depends on the ion blind current, again confirming the dominance of field driven transport. In the membrane, on the other hand, the backside current increases approximately parabolically with the ion kinetic energy at low repeller voltages. The theoretical expressions that describe the trend for the backside current were found to be:

$$I_{back} = \frac{9 \phi_{surf}^2 Z e A D \epsilon_0 \epsilon_r}{8 L^3 k_B T} \quad (34)$$

in the membrane case, and for the glass:

$$I_{back} = \frac{\phi_{surf} Z^2 e^2 A D n}{L k_B T} \quad (35)$$

where Z is the charge number of the ions, e is the elementary charge, A is the bombarded area, D is the temperature dependent diffusion constant, n the number of charge carriers inside the film, L is the thickness of the specific ion conductor material, k_B is the

Boltzmann constant and T the temperature. According to the theoretical description of the process up to now discussed, in the case of ion-conducting glasses, an ohmic behavior is expected, resulting in a linear relation between current and voltage. If this is the case, then the conductance G and the specific conductivity σ , in turn, can be determined from the slope m of the recorded current-voltage characteristic curve by taking into account the bombarded area A and the thickness d of the sample according to the following formulas:

$$G = m = \frac{\Delta I_{det}}{\Delta U_{rp}} \quad (36)$$

$$\sigma = G \cdot \frac{d}{A} \quad (37)$$

Simulations based on the coupled NPP-equations

Within the work of this thesis, numerical simulations on the basis of the NPP-equations (introduced in section 2.3.3 Electrodiffusion) have been performed in order to gain more insights into the transport process investigated within the experiments conducted.

To this end, the coupled set of equations (20)-(22) was solved via a fourth order Runge-Kutte routine. Therefore, the z-axis has been discretized into space elements, which could in principle have different sizes Δz_i . The discrete NPP-equations (20)-(22) can then be written as follows:

$$J_{v,i}^{i+1} = -D_{v,i}^{i+1} \left(\frac{n_{v,i+1} - n_{v,i}}{\Delta z_i} + n_{v,i}^{i+1} \frac{\varphi_{i+1} - \varphi_i}{\Delta z_i} \frac{e}{K_B T} \right) \quad (38)$$

$$\varphi_i = \left(\frac{\frac{en_i}{\epsilon_0 \epsilon_r} \Delta z_i \Delta z_{i+1,i} \Delta z_{i,i-1} + (\varphi_{i+1} \Delta z_{i,i-1} + \varphi_{i-1} \Delta z_{i+1,i})}{\Delta z_{i,i-1} \Delta z_{i+1,i}} \right) \quad (39)$$

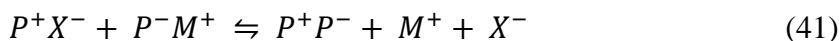
$$\frac{\partial}{\partial t} n_{v,i} = - \frac{J_{v,i}^{i+1} - J_{v,i-1}^i}{\Delta z_i} \quad (40)$$

Where i is the index of the space element, $n_i = \sum_v (n_{v,i} - n_v^0)$ the excess ion density and $\Delta z_{i,i+1} = 0.5(\Delta z_i + \Delta z_{i+1})$ the distance between the centers of two adjacent space elements I and $I + 1$. The ion flux density between these two space elements is given by $J_{v,i}^{i+1}$, while $D_{v,i}^{i+1}$ and $n_i^{i+1} = (n_i \Delta z_{i+1} + n_{i+1} \Delta z_i) / (\Delta z_{i+1} + \Delta z_i)$ are the diffusion coefficient and the ion density at the boundary of the two space elements. The reader should note that in equation (39) the electric potential depends on the exact charge distribution inside the sample as well as on the potential in the neighboring space elements. Therefore, the potential is calculated recursively using the potential of the previous recursion step as an input for the actual recursion step. The converged potential subsequently enters the Nernst-Planck equation (38) where the electrodiffusion of the carriers is calculated. The so calculated ion fluxes enter Fick's second law such that the ion distribution is modified. In the following time step, the potential is calculated again to match the modified ion distribution and so forth.

The calculations have been performed by means of a simulation configurator. For the calculation the z -axis is discretized into space elements Δz , whose number and width can be arbitrary chosen from the operator. The time grid has been set in time increments Δt as well. In particular, the time evolution of the ion transport is followed until a quasi-stationary situation is reached, where the ion current adsorbed at the sample from surface and the current measured at the backside electrode become equal. In the relevant sections regarding the results, specific values for the space and time grids used for the calculations will be given.

2.3.4 Ion Transport through PEMs

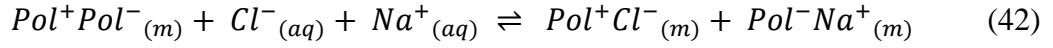
Bearing in mind the well know layer-by-layer technique discussed in section 2.1 and using simple equilibrium arguments, the alternate adsorption of cationic and anionic polyelectrolytes which leads to the complex formation of polyelectrolyte multilayers, may be written according to equilibrium:



in which P^+ and P^- stand for polymer-bound, positively and negatively charged groups, respectively, and M^+ and X^- are the small metal and halogen counter-ions. Since each polymer chain contains a large number of charged groups, a physically crosslinked network structure is formed, in which the P^+P^- ion pairs represent the crosslinking sites. While for polyelectrolytes of lower charge density the small counter-ions are completely released upon multilayer formation [82], some of the counter-ions remain with polyelectrolytes of high charge density, such as PAH, probably due to Manning condensation [83]. As a consequence, membranes made of highly charged polyelectrolytes contain P^+P^- pair as well as P^+X^- and P^-M^+ pairs. The latter ones act as ion-exchange sites and introduce bipolar properties to the membrane [84, 85]. As a consequence, the permeating cations and anions receive a pronounced Donnan rejection at the positively and negatively charged layers, respectively. Because of their higher charge density, the divalent ions are more strongly rejected than the monovalent ones, and the membranes show high selectivity in ion transport [84, 86]. In addition to the electrostatic (Donnan) effect from the P^+X^- and P^-M^+ pairs, it was suggested that the P^+P^- also contribute to the selectivity. Under the influence of the permeating ions, the polymer-bound ion pairs may be separated. The separation produces new exchange sites, which interact with the permeating ions and contribute to the selectivity in ion transport. As a consequence, ion transport proceeds as hopping between discrete polymer-bound exchange sites [87].

In their work in 2003, Farhat and Schlenoff described the mechanism of ion transport across PEMs made of poly(diallyldimethylammonium) (PDADMA) and poly(styrene sulfonate) (PSS) as ion hopping between discrete sites: these sites are small clusters of extrinsic polymer charges coupled to counterions. Using simple equilibrium

arguments (see equation (18)), it may be shown that an intrinsic PEM may be converted to one that bears extrinsic sites by exposure to a solution containing salt [88]:



The system essentially behaves as a variable capacity ion exchanger. These sites are small clusters of extrinsic polymer charges coupled to counterions. Any ion, be it a salt or a probe ion, is associated with a particular oppositely charged polymer segment. This is a rather un-Debye-Hückel (DH) statement: in the high ionic strength limit, charges should be heavily screened and oblivious of each other [89]. However, DH theory is valid for dilute ionic strength and assumes a mean field for the electrostatic potential experienced by a point charge in the presence of others [89]. In their theory model, Farhat and Schlenoff assert that the polymer charges within the PEMs are discrete and recognizable as such by counterions. Viewed at the molecular level, hopping is actually an ion exchange: extrinsic charges occupied by salt counterions are now replaced by a probe ion, and the vacancies that appear as a result of the departure of the probe ion are occupied by salt ions, so at some point in this transaction, there is a momentary charge separation of ion from fixed site. A motion of this kind should be thermally activated, and the appropriate temperature dependence has been observed previously [88]. An ion exchange hopping, where salt and probe ions change place, implies that the movement of both species is coupled. This coupled interdiffusion of two different anions, A and B, with diffusion coefficients D_A and D_B , and charges z_A and z_B and respective membrane concentrations C_A and C_B , can be described in terms of one diffusion coefficient D_{AB} by [90]:

$$D_{AB} = \frac{D_A D_B (z_A^2 C_A + z_B^2 C_B)}{z_A^2 C_A D_A + z_B^2 C_B D_B} \quad (43)$$

From equation (43), it is evident that the slower ion present at lower concentration will have a stronger effect on interdiffusion. The diffusion coefficient for hopping transport in two dimensions is given by $D = \delta_{\text{hopp}}^2 / 4\tau$ [91] where δ_{hopp} is the average hopping distance and τ is the hopping time. In figure 13 below a graphic representation of the hopping model according to Farhat and Schlenoff model is exemplified:

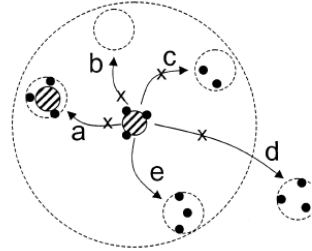


Fig. 13: Representation of the boundary conditions for hopping model according to Farhat and Schlenoff.

A probe ion (shaded circle in the middle) balanced by three univalent extrinsic sites, attempts to hop under five scenarios. Each hopping attempt results in either failure or success. The large dashed circle represents a hopping range and, the small dashed circles represent a site of adjacent lattice points within which the probe must find at least three extrinsic charges available to maintain electroneutrality. Of the five hopping attempts depicted (from (a) to (e)), only (e) is successful in finding an unoccupied (by probe ion) site with at least three charges within the hopping range.

2.4 Thermionic emission

The thermionic emission is a process in which electrically charged particles are emitted from a material by heating the emitter. Originally thermionic emission was introduced for describing the production of electrons from heated metal wires [92, 93]. Soon, however, it was discovered that thermionic emission also includes the emission of ions from solid material [94]. Thermal emission of electrons was first introduced by heating a wire filament with an electric current [95]. The amount of thermal emission of electrons or ions from the surface of the material increases rapidly, by enhancing the temperature of the emitter. The temperature dependence of the total ion current density from alkali metal aluminosilicates, in general, follows the Richardson–Dushman behavior [96], which was originally developed for the emission of electrons from metals:

$$J_0 = A_R T^2 \exp\left\{-\frac{W}{k_B T}\right\} \quad (44)$$

Here J_0 is the total ion current density, W is the effective work function, A is a universal emission constant, T is the temperature and k_B the Boltzmann constant. Each material has its own work function and the work function is associated with the Fermi level E_f and the ionization energy χ of the material, represented by [97]:

$$W = \chi - E_f \quad (45)$$

The ionization energy is the amount of energy required to remove the outermost electron (valence electron) from its atom in free space. The Fermi energy level E_f is the highest electron energy state populated in a material at absolute zero temperature. The material Fermi level and work function are the primary properties that determine the emission behavior for a given material set. Richardson's equation (44) suggests that the emission current is independent of the field strength of the emitter. However, the experiments displayed that the electric field also plays a role in determining the emission current

density. In general, it is well known that there are different regimes of the electric field in thermionic emission. At low fields, the emission is dominated by the formation of a space-charge zone in front of the emitter giving rise to an upper limit of the ion current possible. This is in general referred to as the Child-Langmuir regime [98, 93]:

$$J = k \left\{ \frac{U_{rp}^{\frac{3}{2}}}{d_{CoI}^2 \sqrt{M_{Ion}}} \right\} \quad (46)$$

where U_{rp} is the potential at the emitter-vacuum interface, d is the distance between the emitter surface and grounded detector plate, M_{Ion} is the mass of the ion emitted, and k is a material constant. At moderate field strengths, the emission current is thermally dominated by the Richardson-Dushman relation [99, 100, 98, 93, 92]. The space charge in front of the emitter surface does not effectively limit the ion current anymore and at high electric field strengths, the field dependence of the emission current is determined by the Schottky effect, which decreases the effective work function according to [101]:

$$J = J_0 T^2 \exp \left\{ \frac{e\sqrt{eE}}{k_B T_S} \right\} \quad (47)$$

where J_0 corresponds at the ion flux density according to the Richardson-Dushman equation, E is the applied field $E = U/d$ and T_S a constant named Schottky-Temperature.

Thermionic emitters have a wide range of application: as a source of electron in conventional electron tubes (e.g., television picture tubes), as an ion source in many technological and scientific branches such as Li-ion sources in satellite charge control [102]; in particular sodium and potassium ions are used as an important tool for signal transduction in cell biology [103] and cesium ions in commercial time of flight secondary ion mass spectrometry [104]. Among the ion emitting materials, zeotype aluminosilicates appear to be particularly efficient for thermionic production of long term stable alkali metal ion beams. For the emission of lithium, sodium, potassium, and rubidium ions

aluminosilicates of composition $MAlSi_2O_6$ ($M = Li-Rb$) have been mainly used. The solid aluminosilicate emitters can be used for the realization of a simple broad-beam alkali ion source for application in ultra-high vacuum [105]. Aluminosilicates are often mixed with molybdenum (Mo) in order to guarantee a homogeneous temperature distribution of the material [106]. Aluminosilicates are of the composition $X_2O \cdot Al_2O_3 \cdot 2SiO_2$, where X represents the alkali species. The basic structure of this material is silica with a certain proportion of the Si^{4+} ions replaced by Al^{3+} in silicate to produce a framework with Al–O – Si linkages. The silica crystalline structure is very open with large tunnels through which the alkali metal ions can move freely. Aluminosilicate is a good ionic conductor, but not an electronic conductor. Because of this special property aluminosilicates can be used as ion exchanger as well as thermionic emitters [107].

3 Methods of analysis

3.1 CAIT Description

The acronym CAIT (charge attachment induced transport) refers throughout this thesis to the method of analysis developed in 2010 within the research group of Prof. Weitzel. This technique represents a new experimental approach for measuring ionic conductivity, diffusion coefficient and activation energy of specific ion transport through different kind of materials. In the scientific environment there is a considerable number of experimental methods available for characterizing the dynamics and transport of ions, e.g. impedance spectroscopy (IS) [108, 109], solid-state NMR techniques [110, 111], pulsed field gradient NMR (PFG-NMR) [112, 113] and tracer diffusion (RTD) [114, 115, 116, 117]. Although impedance spectroscopy is one of the most commonly used techniques, however, the technique relies on a well-defined electrical contact between the samples and two electrodes. There are situations where it would be advantageous to have a technique for measuring conductivity which requires only one contact between the sample and an electrode: in the case of thin film samples, to name one, the evaporation or sputter deposition of a second electrode may lead to an electrical short circuit, or furthermore when dc bias voltages are applied, there may be anodic dissolution and cathodic deposition of the metal resulting in unstable sample/metal interfacial contacts [118]. In this context the CAIT method represents an alternative and innovative technique; over the last decade, within the works of this group of research, conductivity, diffusion coefficient and activation energy for the transport of ions through borosilicate glasses [119, 2], phosphate glasses [3, 4], PPX film [5] and polyelectrolyte multilayers [6, 7] together in some case with numerical simulations [120, 121] have been studied.

The CAIT method is based on bombarding an ion conducting sample with an appropriate low energy ion beam generated by a thermionic emission process (see previous section 2.4). The homogeneous ion beam is accelerated with a certain kinetic energy U_{rp} by an electrostatic lens, the repeller lens (see the experimental part for details and description). The kinetic energy of the ions is given by:

$$E_{kin} = \frac{1}{2}mv_0^2 = ZeU_{rp} \quad (48)$$

where m is the ion mass, v the ion velocity and Ze is the charge of the ionic species. By means of a series of electrostatic lenses, the ion beam is focused and directed toward the sample. The ions at the surface of the sample are absorbed via a soft landing process which avoids an undesired implantation phenomenon. The bombarder ions impinge on the front surface of the sample, leading to the formation of a surface potential and a surface particle density. Since the backside of the sample is in contact with an electrode and that electrode is grounded, then a potential and particle density gradient toward the backside of the electrode arises. The ions are transported according to these gradients and move toward the grounded electrode where they are neutralized and a corresponding neutralization current can be detected I_{back} .

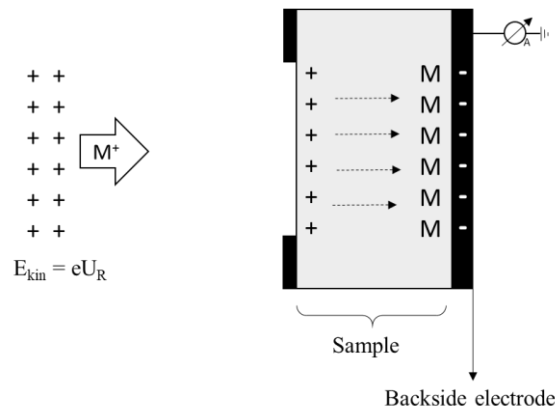


Fig. 14: Transport of ions toward a sample and neutralization at the backside electrode.

A quasi-stationary (steady state) current only rises under the condition that as many ions are deposited on the surface as many ions are neutralized at the backside electrode (figure 14). The evolution of the backside current against the time can be better described by the electric circuit in figure 15 [122]:

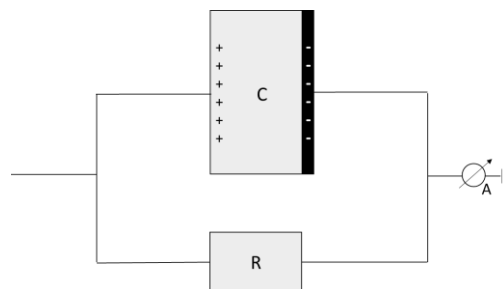


Fig. 15: Representation of the evolution of the backside current *via* an equivalent circuit.

It has been said that after the deposition of positive ions on the surface of the sample, a positive potential will be generated: in terms of circuit, one side of the capacitor will be positively charged. As a compensation process of the excess of charge, electrons will accumulate along the backside electrode, leading to a higher I_{back} at the beginning of each measurement. As the charge compensation proceeds, the capacitive current drops more and more, until a stable and constant value is reached (I_{back}). This represents the steady-state condition named above. Ultimately the detected current consists of two contributions:

- I_R , the resistive current, which falls throughout the resistance R of the film
- I_C , the capacitive current, which can be described as follow:

$$I_C = I_{max} \times \exp\left(-\frac{t}{\tau}\right) \quad (49)$$

Where I_{max} is the current at the beginning of the discharging process of the capacitor and describes the time needed until the discharging process is completed, and τ is defined as $\tau = RC$ (with R the resistance of the film and C the capacitance)

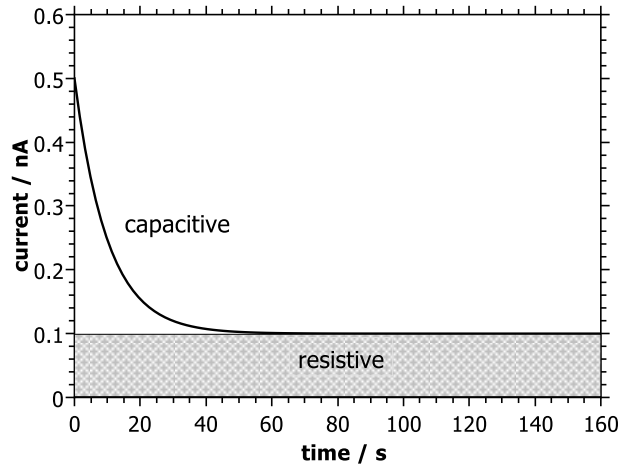


Fig. 16: Resistive and capacitive contributions of the registered backside current.

3.2 Time-of-flight Secondary Ions Mass Spectrometry (ToF-SIMS)

3.2.1 Principle of a SIMS analysis

Secondary ion mass spectrometry (SIMS) is based on the detection of ionized molecules, molecular fragments or atoms generated as a consequence of the bombardment of a primary ion beam on the surface of the sample under analysis. The technique has its roots on the characterization of materials in the semiconductors industry and evolved to be one of the most powerful techniques for the analysis of organic and inorganic samples [123, 124]. Although the emission of secondary ions from surfaces was observed about 100 years ago [125], the first instruments only appeared in the early 1950s and 1960s (Herzog [126], Leibl [127], Castang and Slodzian [128]). Up to the early 1980s the widest application of SIMS was to exploit its destructive capability to analyze the elemental composition of materials as a function of depth. This approach was known as dynamic SIMS, which found extensive application throughout the semiconductor industry where the technique has had a unique capability to identify chemically the ultra-low levels of charge carriers in semiconductor materials and to characterize the layer structure of devices. Although of great importance, this variant of SIMS could not be described as a surface mass spectrometry. It was only in the late 1970s that the surface mass spectrometry capability was developed as a consequence of the work of Benninghoven and his group in Münster [129]. Although the SIMS technique is basically destructive, the Münster group demonstrated that using a very low primary particle flux density ($< 1\text{ nA cm}^{-2}$) the information derived from the mass spectra data would be characteristic of the chemistry of the surface layer, because statistically no point on the surface would be impacted more than once by a primary particle during an analysis. This approach was named as *static SIMS*. From that moment the nomenclature *dynamic SIMS* and *static SIMS* appeared, where the two are distinguished by the primary ion dose acceptable during analysis. For *static SIMS* the limits for the acceptable primary ion dose density is $< 10^{13}$ ions cm^{-2} per experiment [130], in contrast in *dynamic SIMS* the minimum dose measurement is $\sim 10^{17}$ ions cm^{-2} (see paragraph analysis modes for details). In both cases, *static* or *dynamic* SIMS, the principal phenomenon related to the formation of secondary ions is the sputtering process which can be described as a cascade of collisions of the incident particles in the material being analyzed (a general view of the process is

represented in figure 17). Ions from the source collide with the surface of the sample generating atomic motion by either direct collisions between the primary ions and the atoms of the material, or non-direct collisions between atoms in motion (which in particular for polymer leads to a collective molecular motion regime [131]). Since typical primary ion beam energies are of the order of keV, the collisions energies are much higher than the binding energies of the atoms in the material, resulting in an extensive fragmentation around the collision region and producing essentially only the emission of atomic particles. As the collision cascades spread they become less energetic, resulting in less fragmentation and generating the emission of molecular fragments (see schematic in figure 17). The fragments from the first monolayers of the sample will have sufficient energy to overcome the surface binding energy and leave the sample. Such fragments are ejected as atoms and molecules. The description of the sputtering phenomenon and ion formation is still the object of much research, with several models that consider both theoretical aspects and molecular dynamics simulation results [131, 132, 133, 134, 135, 136, 137].

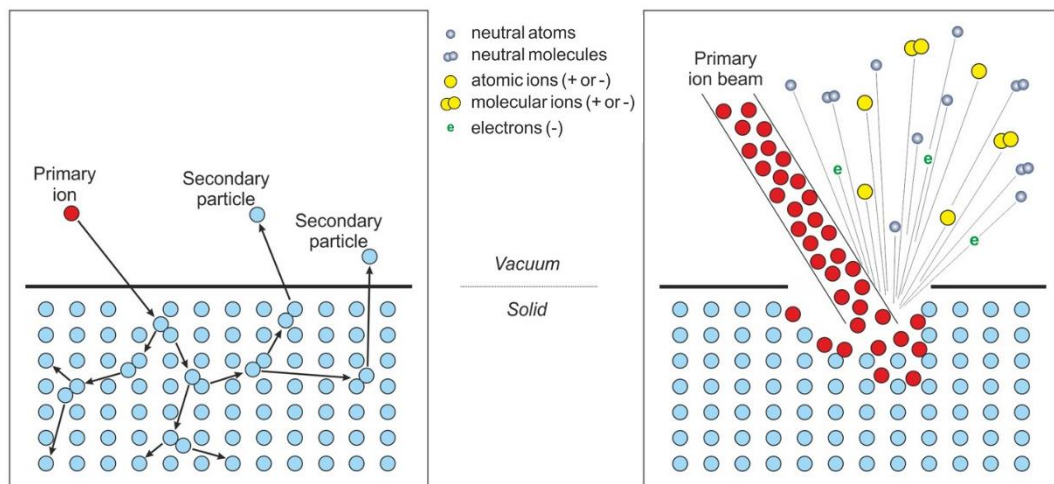


Fig. 17: Description of the sputter process. Left: the impact of the primary ion induces a collision cascade of particles in the solid that leads to ejection of particles when returning to the surface. Right: secondary particles ejected during the sputter process. Picture taken from [138].

The sputtering yield (Y) determines the rate of material desorption after the incidence of primary ions. It is defined as the ratio between the number of atoms removed and the number of incident ions. However, only a small fraction of the atoms and fragments removed are ionized (from 0.0001% to 10%) [139]. The basic SIMS equation relates the number of ionized species of mass m to their sputtering yield Y_m [140]:

$$I_m = I_p Y_m \alpha \theta_m \eta \quad (50)$$

where I_m is the current of ions with mass m , I_p is the primary ion current, α is the ionization probability, θ_m is the concentration of m in the surface and η is the transmission of the analyzer employed. Both the sputtering yield and the ionization probability will depend on parameters such as the primary ion beam energy, the angle of incidence and the type of molecule. Furthermore, the electronegativity of species present in the surface of the material under analysis will influence the ionization probability of different fragments of the same molecule. This is known as *matrix effect* and is a significant problem when it comes to quantification of ToF-SIMS data.

In conventional SIMS instruments, secondary ions are generated continuously by use of a static primary ion beam, and the different ion species are detected sequentially, e.g. in a *double-focusing magnetic* mass spectrometer or a *quadrupole* spectrometer. At a given instant, only secondary ions of a previously selected mass-to-charge ratio reach the detector. Thus, most secondary ions are not measured. Even in multi-detector instruments, only a few ion species with similar mass-to-charge ratios can be detected simultaneously. Most secondary ions are therefore lost during the analysis. Contrary to this, *time-of-flight* mass spectrometry allows measuring all secondary ions with one polarity quasi-simultaneously. This together with the high resolution capabilities of the modern instruments made the latter being the most popular one. In the next sections, the main components of a ToF-SIMS instrument will be described in details.

3.2.2 ToF-SIMS Setup

The ToF-SIMS IV instrument used for the results presented in this thesis was commercialized by the company ION-TOF GmbH (Münster, Germany). The system supports three different primary ion sources, the main one being a bismuth *liquid metal ion gun* (LMIG), that can produce monoatomic or cluster Bi^{+n} beams, and a *dual-source column* (DSC) with sources capable of producing O^{2+} atoms and Cs^+ ions. The O^{2+} and Cs^+ beams are typically used for etching in depth profiling modes. The instrument has also an electron gun for charge compensation. The two sources (i.e. LMIG and DSC) are positioned at 45° to the surface of the sample and in between stays a ToF analyzer with a single stage reflectron and a multi-channel plate detector capable of up to 20 kV post acceleration voltage, resulting in a time resolution of nanoseconds for typical pulsed acquisition. The analysis chamber is maintained at ultra-high vacuum at a pressure of around 10^{-9} mbar. Figure 18 shows a picture of the equipment with its main components.

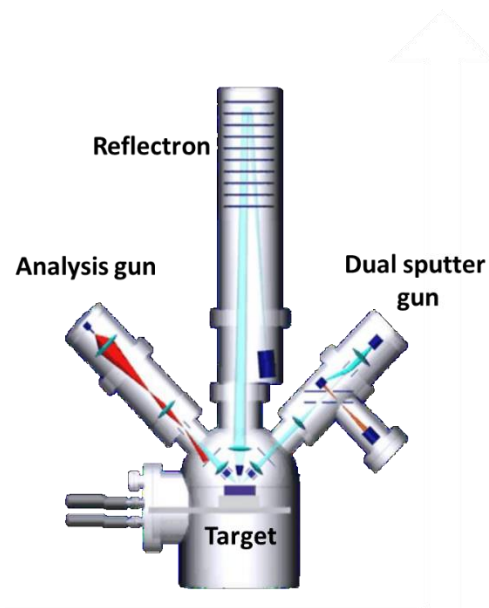


Fig. 18: Schematic construction of a ToF-SIMS instrument (picture taken from taken from Iontof's training material).

Primary ion beam column

In figure 19 below all the components present in the primary ion beam column are shown. The column contains a liquid metal ion gun (LMIG) with a bismuth tip.

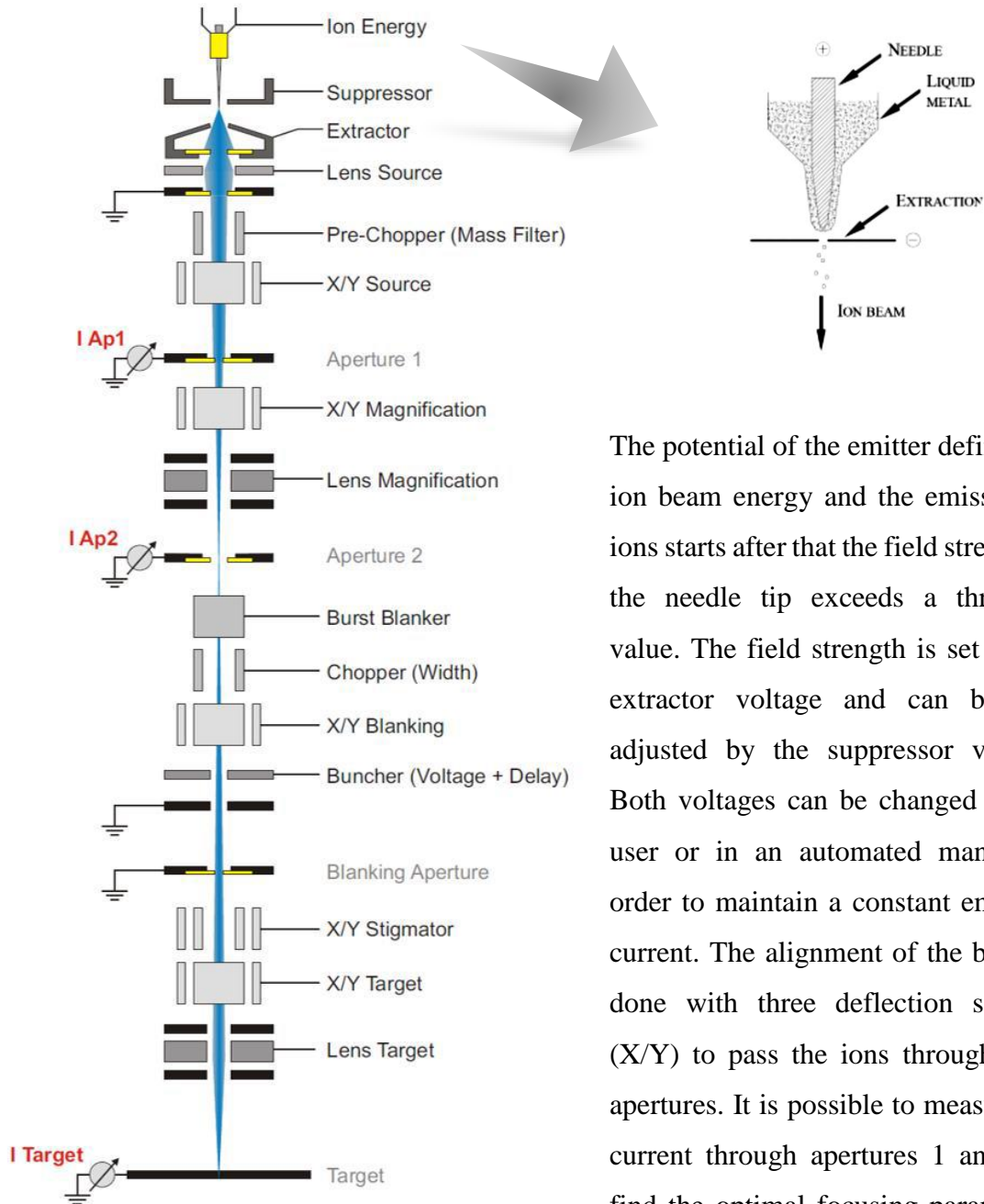


Fig. 19: Illustration of an LMIG with its components.
Adapted from the instrument manual.

The focusing through the blanking aperture can be optimized by measuring the current hitting the target (with a Faraday cup or even a conducting sample). For all analysis modes, the beam must be pulsed and this is done at the pre-chopper and

The potential of the emitter defines the ion beam energy and the emission of ions starts after that the field strength at the needle tip exceeds a threshold value. The field strength is set by the extractor voltage and can be fine adjusted by the suppressor voltage. Both voltages can be changed by the user or in an automated manner in order to maintain a constant emission current. The alignment of the beam is done with three deflection systems (X/Y) to pass the ions through three apertures. It is possible to measure the current through apertures 1 and 2 to find the optimal focusing parameters.

chopper which is also where the beam mass filtering is done by blocking ions of different masses that will have different velocities for the same beam energy (the highest current beam species are Bi^+ and Bi^{3+}). The maximum energy of the beam is 30 keV for single charged species.

Dual-source column

The dual-source ion column (DSC) contains an electron impact source capable of producing O_2^+ and a thermal sputtering ion source capable of producing Cs^+ . A 90 degrees deflection magnet is used for beam selection and the focusing, bunching and pulsing work in a similar way to the primary ion beam column. These sources are used more commonly as etching guns in depth profiling modes (see next section 3.1.3) although they can also be used as primary ion guns for specific applications. Figure 20 shows a schematic with the main components present in the dual-source column. Typical energies for the O_2^+ and Cs^+ beams are respectively 1 keV and 3 keV.

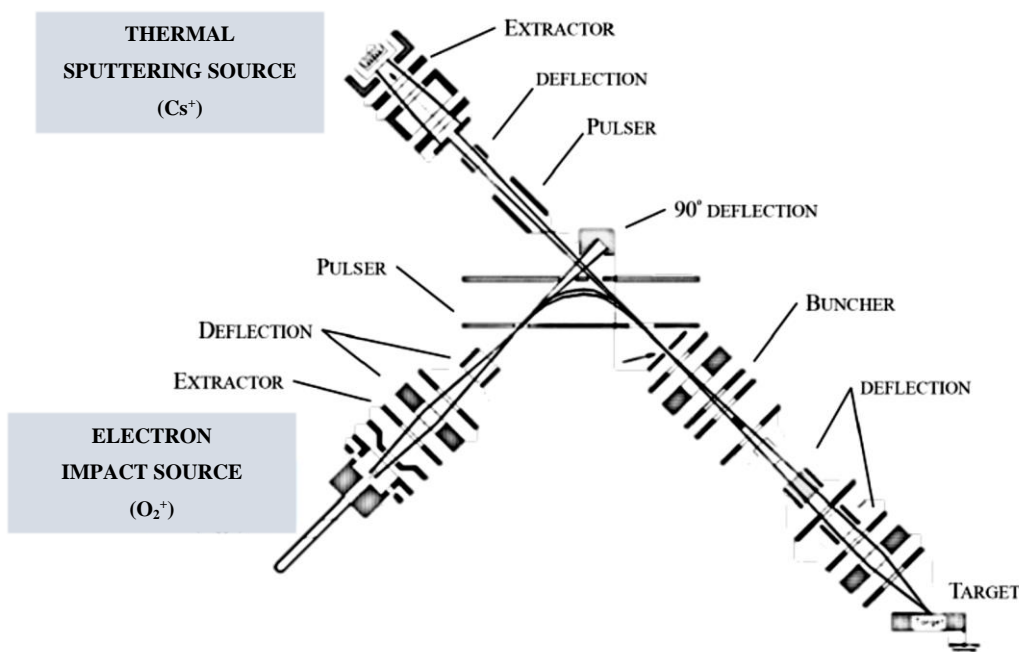


Fig. 20: Schematic illustration of a dual-source ion column. Adapted from the instrument manual.

Analyzer and Detector

A time of flight (ToF) analyzer has unique characteristics that make it the ideal detection system for SIMS. In a *linear ToF* secondary ions are separated by their mass/charge ratio (m/z) and their masses are determined by the time they take to travel a distance L in a flight tube free of electromagnetic fields after being accelerated by an extractor to a common energy E . The relation between E and the flight time, t , is:

$$E = zU = \frac{mv^2}{2} = m \frac{L^2}{2t^2} \quad (51)$$

where z is the ion charge state, U is the extractor potential and v is the velocity of the secondary ion. Therefore, lighter ions travel at higher speeds and reach the detector before heavier ions in a time t , according to the relation:

$$t_d = L \left[\frac{m}{2E} \right]^{\frac{1}{2}} = L \left[\left(\frac{m}{z} \right) \frac{1}{2U} \right]^{\frac{1}{2}} \quad (52)$$

The drift time t_d as calculated by means of eq. (52) is not fully identical to the total time of flight. A rigorous mathematic treatment of the ToF analyzer has to include all contributions to the total time-of-flight. For instance, the time needed for acceleration of the ions t_a has to be added. A further elaboration of the total time of flight will be successively introduced, as the reflectron system and its advantages will be discussed.

There are several factors that influence on a ToF-analyzer resolution (or width of a secondary ion packet) [141] such as angular spread of ion trajectories or effective depth of the detector, but the major source of resolution degradation is the energy spread (ΔE) of ions of the same mass. The resolution R is indeed, in first order, determined only by the energy spread:

$$R \equiv \frac{t}{2\Delta t} = \frac{m}{\Delta m} = \frac{E}{\Delta E} \quad (53)$$

In order to overcome such problem, scientists came up with the idea of introducing a reflector as focusing ion mirror. Mamyrin *et al.* (1973) demonstrated experimentally a two-stage ion mirror: Mamyrin's proposal in his thesis was to improve energy focusing through the use of a linear static electric field (ion mirror). An illustration of a ToF analyzer with two-stage ion mirror is shown in Figure 21. The picture has been taken from a literature study [142] and it illustrates the setup used for a photoelectron photoion coincidence (PEPICO) experiment. However, the sketch represents a good didactic example of how a reflectron system, used in a typical ToF-SIMS instrument, works.

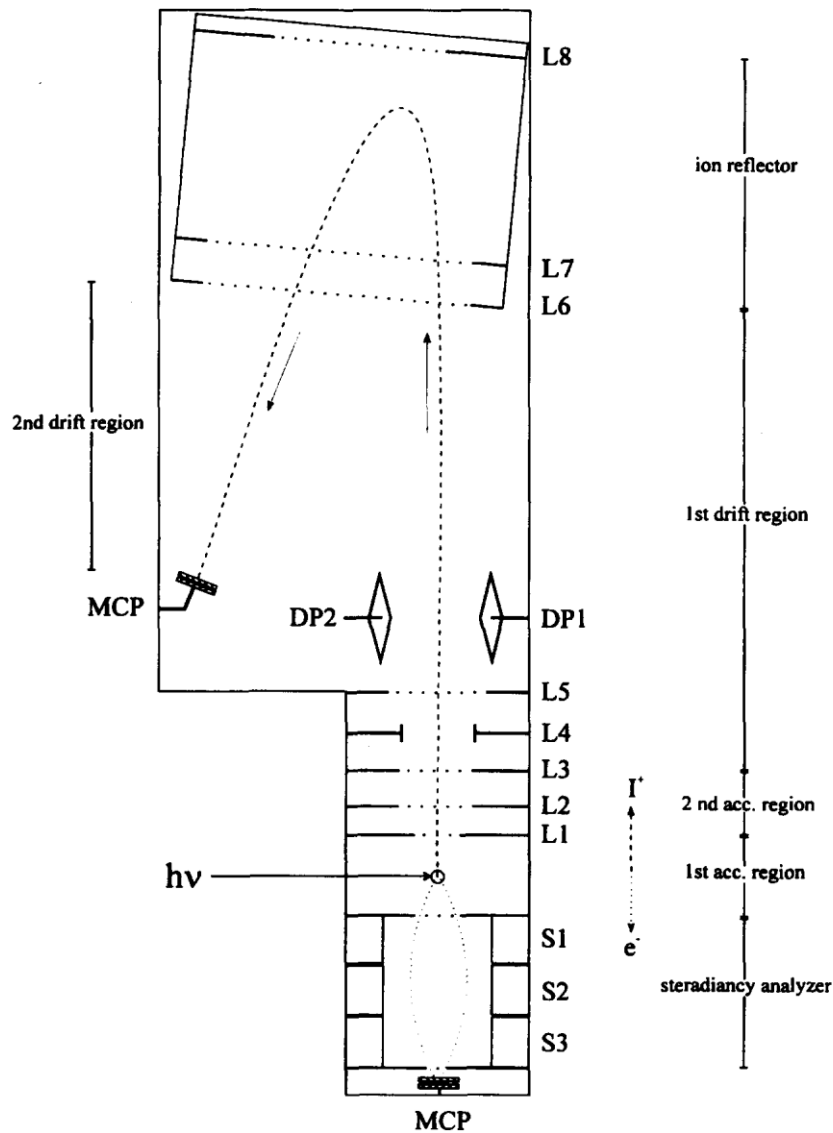


Fig. 21: Sketch of a reflectron spectrometer [142].

The ion spectrometer consists of five different regions. The ion source defined by the lens elements S1 and L1 ($d = 1.5$ cm) serves as the first acceleration region. The lenses L2 and L3 ($d = 2.3$ cm) define the second acceleration region. The latter lens has the same potential as the lenses L5 and L6, i.e. that of the drift tube. The two-stage acceleration creates a space focus within the first field free drift region (1stFFDR). After passing through the 1stFFDR (from L3 to L6, length = 87.3 cm) the ions are decelerated and turned around in a two-stage ion reflector consisting of a first deceleration region L6 to L7 and a reflection region L7 to L8. The ions then pass through a second field free drift region (2nd FFDR, length = 33.6 cm) before being detected at a microchannel plate (MCP) detector. For understanding the mode of operation of a reflectron, one can take the space focus of an ion source as a start point for the flight of ions of one distinct mass, with no spatial or temporal distribution, but with different kinetic energies. After the drift length in the 1stFFDR, the ions with higher kinetic energy first enter the ion mirror, followed by those with lower kinetic energy. The former penetrate deeper into the reflecting field than the latter, resulting in a longer residence time within the reflector for the higher energy than for the lower energy ions (see figure below):

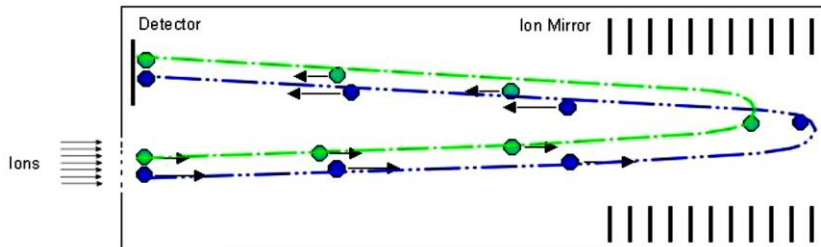


Fig. 22: Representation of a reflector compensating for distributions of initial kinetic energies of analyzed ions: an ion entering with large kinetic energy will have a longer travel distance inside the reflectron (blue dot) than an ion with low kinetic energy (green dot).

The total time-of-flight t_{ToF} is the sum of the flight times in the individual spectrometer areas, according to the equation [143]:

$$t_{\text{ToF}} = t_{A1} + t_{A2} + t_{1\text{FFDR}} + 2t_{\text{dec}} + 2t_{\text{ref}} + t_{2\text{FFDR}} \quad (54)$$

where:

$$t_{A1} = 2 C x_{A1} \sqrt{\frac{m}{U_{A1}}} \quad (55)$$

with t_{A1} the time of flight in the first acceleration region, $C = 0.71986 \mu\text{sV}^{1/2}/\text{cm}$ a constant, U_{A1} the energy of the ions within that region, m the mass of the ion and x_{A1} the path of the ion in the first acceleration zone;

$$t_{A2} = \frac{2 C x_{A2}}{U_{A2}} \sqrt{m} (\sqrt{U} - \sqrt{U_{A1}}) \quad (56)$$

with t_{A2} the time of flight in the second acceleration region, U the total energy of the ions and x_{A2} the path of the ion in the first acceleration zone;

$$t_{1FFDR} = 2 C x_{1FFDR} \sqrt{\frac{m}{U}} \quad (57)$$

with t_{1FFDR} the time of flight in the first field free drift region and x_{1FFDR} the path of the ion in that zone;

$$t_{dec} = \frac{2 C x_{dec}}{U_{dec}} \sqrt{m} (\sqrt{U} - \sqrt{U - U_{dec}}) \quad (58)$$

with t_{dec} the time of flight in the deceleration region of the reflectron, U_{dec} the energy lost from the ion due to the deceleration and x_{dec} the path of the ion in that region;

$$t_{ref} = 2 C x_{ref} \sqrt{\frac{m}{U - U_{ref}}} \quad (59)$$

with t_{ref} the time of flight in the reflection region of the reflectron, U_{ref} the energy gained from the ion due to the reflection and x_{ref} the path of the ion in that region;

$$t_{2FFDR} = 2 C x_{2FFDR} \sqrt{\frac{m}{U}} \quad (60)$$

with t_{2FFDR} the time of flight in the second field free drift region, U the total energy of the ion and x_{2FFDR} the path of the ion in that zone.

In the case of the study conducted in the literature cited above, an extra contribution to the total time of flight needs to be considered, i.e. the “turn-around time”. Ions formed at the same location, within a gas ion source (as in a PEPICO experiment) can have initial velocities in different directions. The time for those ions with the reversed velocities to return to the initial position and to begin their motion towards the detector is the “turn-around time”. However, for a ToF-SIMS experiment this contribution to the total time of flight is not relevant. In a ToF-SIMS instrument, by adjusting the electric fields carefully, all secondary ions of one species can reach the detector practically simultaneously. Optimal reflectron voltage is 20 V for positive ions and – 20 V for negative ones. A parameter that can be changed in order to optimize the mass resolution of the analyzer, and even the most commonly adjusted by a user, is the distance of the extractor tip to the surface of the sample. The optimal distance of the tip is 1.5 mm and this has to be adjusted depending on features of the sample under analysis.

After the reflection, the secondary ions are post-accelerated with energies of 8-10 keV before they reach the detector. The detector consists of a microchannel plate for ions to electron conversion, a scintillator for electron-to-photon conversion, and a photomultiplier, which is placed outside the vacuum chamber. All three steps lead to an amplification of the signal, but the major advantage of this set up is the separation of high-voltage at the detector and low-voltage of the electronics. A constant fraction discriminator converts the incoming signal to a normalized signal, which is further processed in a time to digital converter (TDC). The time resolution of the TDC is adjustable between 50 and 1600 ps, but it is mostly operated at 200 ps. A second detector system is used for the detection of secondary electrons. With this, a secondary electron image similar to those generated in a scanning electron microscope can be obtained by scanning the primary ion beam over the sample.

Electron flood gun

The majority of organic materials are electrically insulating and therefore they will accumulate charge on their surface during a SIMS analysis. Such an effect can reduce or completely suppress the secondary ions reaching the analyzer. The sample charging occurs during the sputtering process after the bombardment of the surface by positive charged primary ions and the simultaneous loss of secondary electrons. The sputtered region will exhibit positive charging unless the material has enough electrical conductivity to carry the electrons to the region in question. In order to neutralize the charge built up during SIMS analysis, a charge compensation system has been developed especially for pulsed primary ion sources used in ToF-SIMS (Hagenhoff *et al.*, 1989). Electrons from a pulsed low-energy electron source reach the target between two primary ion shots. This process is self-regulative due to the low energy (10 eV - 20 eV) of the electrons. The secondary ion extraction field is switched off during the electron pulse.

3.2.3 Analysis modes: mass spectra, surface imaging, depth profiling

There are three analysis modes in ToF SIMS. In the following sections, an overview over the cited modes will be given.

The first one is the *surface spectrometry*, thanks to which high mass resolution spectra can be acquired. For this analysis *static SIMS* condition is used by the application of very low primary ion dose densities. Since the surface is not destroyed, this mode provides detailed elemental and molecular information of the original, non-modified composition from the outer monolayers. With this mode, high mass resolution is provided (8000 m/ Δ m mass resolution).

The second analysis mode is the *surface imaging*. By rastering a fine-focused ion beam over the surface, like an electron beam in an electron microprobe, high spatial resolution secondary ion images (*chemical maps*) can be obtained simultaneously. In this mode, the surface is also not destroyed due to small ion current density. The ToF-SIMS instrument is capable of raster scanning the primary ion beam with a maximum area of 500 x 500 μm^2 . Within the surface imaging mode, more different ways to operate are distinguishable. The three most used modes of operation of the primary ion gun for

surface imaging are the *high current (bunched) mode*, the *burst alignment mode* and the *burst mode* depending on the conditions required from the final images. The *high current mode* requires two beam cross-overs in the deflection systems in order to achieve very short pulse lengths and it can provide good mass resolution ($m/\Delta m \sim 9,000$ at 28 amu) with high beam current (~ 30 nA DC on target) but reduced spatial resolution ($2 \mu\text{m} - 10 \mu\text{m}$ spot size). With only one beam cross-over, the *burst alignment mode* results in a lower current (~ 400 pA DC on target) but enables much better beam focusing and therefore higher spatial resolution (~ 300 nm spot size) but with unit mass resolution. Finally, both good mass and spatial resolution (at the cost of a lower beam current) are provided from the *burst mode*. For all these three analysis modes, a full mass spectrum is recorded per pixel in the raster pattern and the spectra of all pixels are collapsed into one final spectrum representative of the surface under analysis.

The third analysis mode is the *depth profiling*, which operates under *dynamic* conditions and for that is a destructive method. With this mode, one can get elemental or molecular information as a function of depth. Depth profiles are obtained in a *dual-beam mode* where a primary ion beam and a sputter beam are optimized independently. The two beams operate intermittently to provide depth information of secondary ions. The first beam sputters a crater, the second one progressively analyzes the crater bottom, with the precaution that the primary ion gun raster scans a much smaller region than the sputter gun in order to avoid crater wall effects. There are two possible modes of operation for depth profiles: *interlaced mode* and *non-interlaced mode*. In the interlaced mode, mostly used for conductive samples, the sputter beam operates between extraction pulses in a quasi-simultaneous fashion with the primary ion beam. In the non-interlaced mode, ideal for insulating samples, the primary ion beam and analyzer operate separately from the sputter gun, with intervals in the order of seconds that give time for surface relaxation and electron flooding.

3.3 Profilometry

A general depth profile acquired by means of a ToF-SIMS instrument provides the secondary ion intensity as a function of the sputtering time applied. However, the secondary ion intensity as a function of depth is needed to be able to evaluate charge densities or determine diffusion coefficients by normalization procedure. Therefore, a profilometer (Dektak 3ST from Veeco Instruments) has been used in order to transform the sputter time into a sputter depth, by measuring the height of the crater formed as result of the depth profiling.

All profilometers consist of at least two parts: a detector and a sample stage. The detector determines the exact position on the surface of the sample, while the sample stage holds the sample. The stylus profilometer hereby used, consists of a probe which moves along the surface in order to acquire the surface height. This is done mechanically with a feedback loop that monitors the force from the sample pushing up against the probe as it scans along the surface. A feedback system is used to keep the arm with a specific amount of torque on it, known as the “set point”. The changes in the Z position of the arm holder can then be used to reconstruct the surface. Stylus profilometry requires force feedback and physically touching the surface, so although it is extremely sensitive and provides high Z resolution, however, this technique can also be destructive to some surfaces, which are so soft or fragile to be damaged from the motion of the stylus onto them.

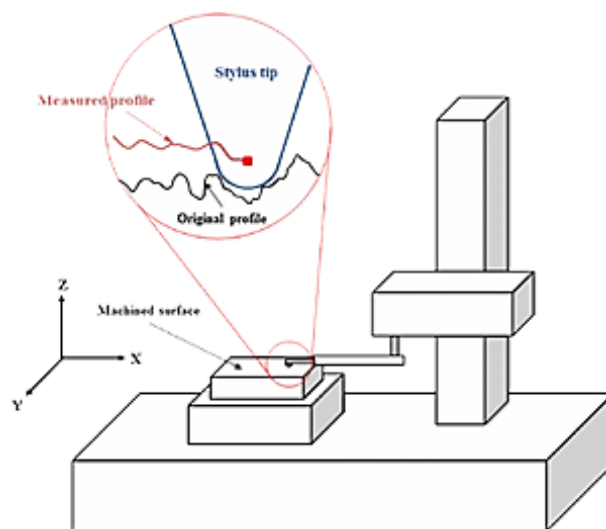


Fig. 23: Schematic of a stylus profilometer. Figure taken from [144].

3.4 Sputter coating

Sputter coating is a widely used technique for depositing thin layers of conductive metal onto non-conducting (or semiconducting) specimens or surfaces for thin film applications. As described in section 4.2 (sample preparation), a coating of thin chromium and gold layers was performed during the procedure of preparation of the PEMs samples. To this aim, a Leica EM ACE600 coating instrument was used, which is configured for the sputtering of a wide range of metal targets and owns a glow discharge capability. A glow discharge is a plasma formed by the passage of electric current through a gas. It is created by applying a voltage between two electrodes in a chamber containing a low-pressure gas. When the voltage exceeds a value called the striking voltage, the gas ionization becomes self-sustaining and it glows. In this specific case, the glow discharge is an optional process useful for cleaning carbon contaminated samples or to clean the sample surface before coating in order to make it hydrophilic. In a conventional sputter coater, the coating is performed using ionized argon to create a plasma. The argon ions are accelerated by high voltage and directed towards the metal target via a magnet where they collide with the source and displace surface atoms. Due to this collision, the surface atoms are directed towards the area below the target and coat the sample. With the quartz thickness measurement, the layer thickness can be calculated as a result of the changed quartz crystal resonance frequency.

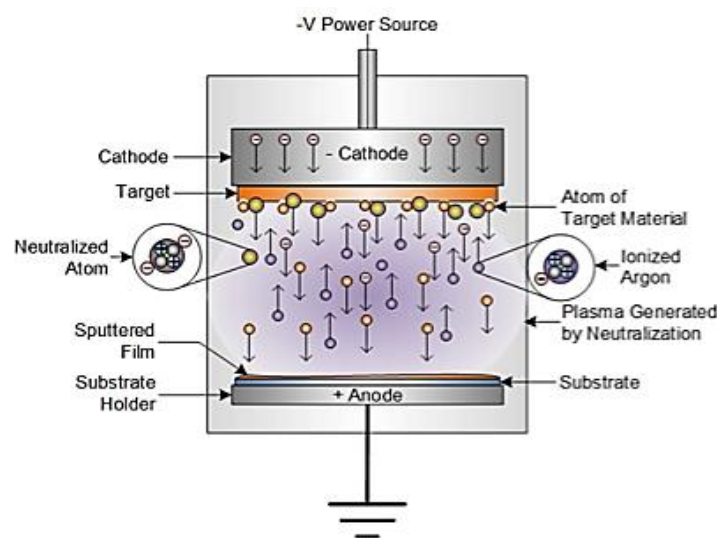


Fig. 24: Diagram of the sputtering process. Taken from [145].

4 Experimental part

4.1 Experimental CAIT setup

The experimental set up for CAIT measurements consists of three main parts: I) the home-made ion emitter, II) the electrostatic ion optics and III) the sample holder. A sketch of the general CAIT experimental setup is schematically depicted in figure 25.

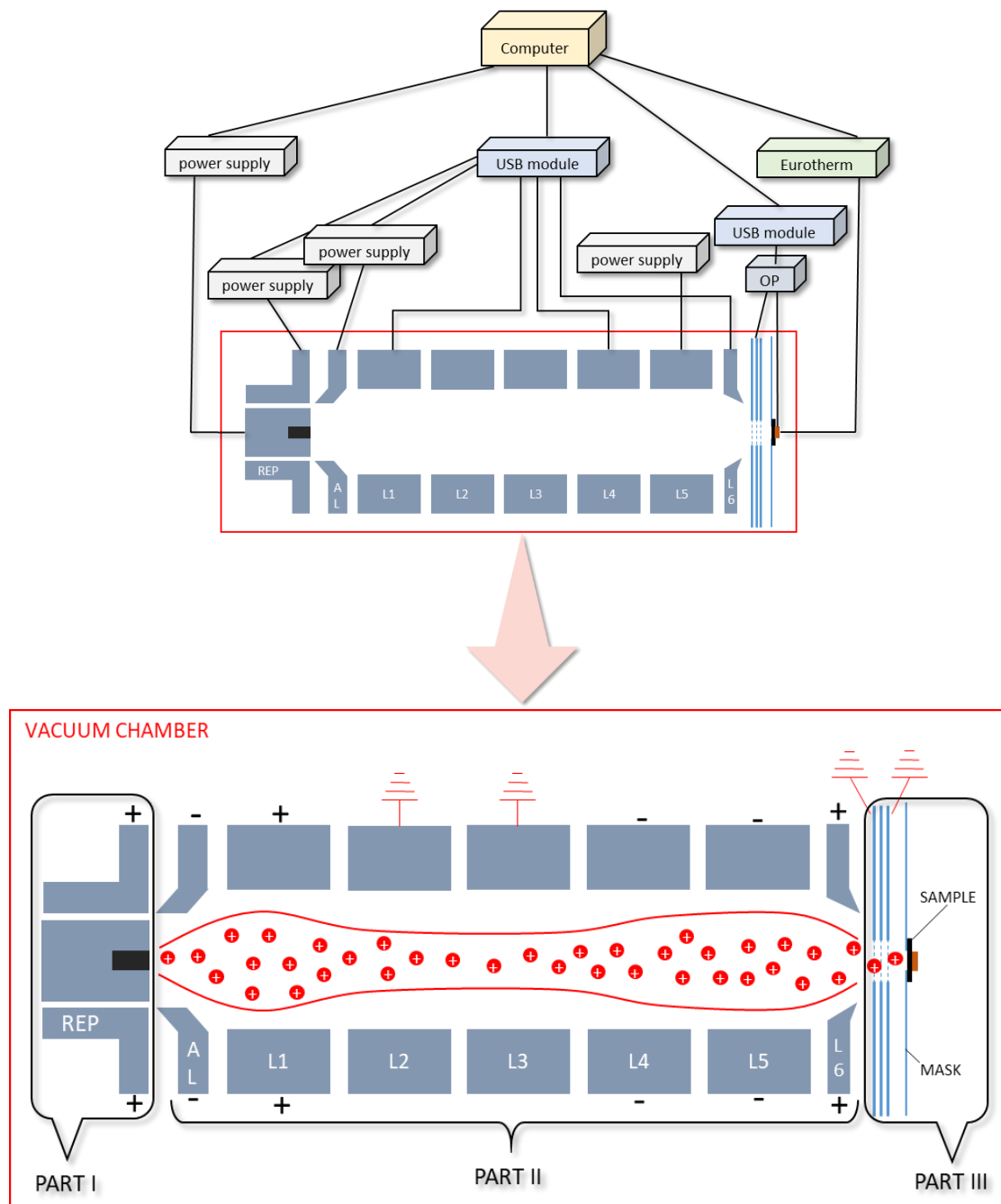


Fig. 25: Sketch of the charge attachment induced transport (CAIT) setup.

A detailed description of the three parts will be presented in the next sections.

4.1.1 Ion emitters

Two emitter designs have been used within the work of this thesis: emitter *type a* for thermionic emission of potassium and rubidium ions and emitter *type b* for lithium ions emission.

Emitter *type a*:

The home-made thermionic emitter of potassium and rubidium aluminosilicates of composition $M[\text{AlSi}_2\text{O}_6]$ ($M = \text{K}, \text{Rb}$) has been used as an ion source in the CAIT experiments. In particular, for potassium ions, the emitting material consisted of a mixture of potassium aluminosilicate (synthetic Leucite). The synthetic Leucite could be prepared by mixing potassium carbonate (K_2CO_3), aluminium oxide (Al_2O_3) and silicon dioxide (SiO_2) in a molar ratio 1 : 1 : 4 [2]. The mixture was then crushed into a corundum tube and heated at 1000 °C for 3 days. After cooling, the material was grounded and assorted with molybdenum (Mo) powder in the ratio of 1:9, in order to guarantee a homogenous temperature of the material. The yield of the product was compressed and annealed at 1200 °C for 12 hours and the mixture was then filled into a steel pot and mounted on an assembly. The home-made thermionic emitter of rubidium aluminosilicate, Leucite($\text{RbAlSi}_2\text{O}_6$) was prepared by mixing stoichiometric amounts of rubidium carbonate (Rb_2CO_3), aluminium oxide (Al_2O_3) and silicon dioxide (SiO_2) in the ratio 1:1:4 [146]. The preparation procedure was the same as the one described for the potassium ion emitter. In both cases, the synthesized emitter materials were placed onto a steel or pot tube which was connected to the heating device. The steel pot and the heating device were covered with a heat shield for homogenous heating of the emitter material. The emission hole of the ion source was 3 mm in diameter and the thermionic emission was caused by a tungsten wire with a heating current, I_{heat} , typically varied between about 4 Amp and 7 Amp, depending on the specific heating device. It is well known that the thermal emission is strongly temperature dependent and becomes more efficient at higher temperatures [96]. As a consequence, a heat shield around the emitter increases the temperature in such a way that the ions were more efficiently emitted and a continuous ion current can be generated at the position of the sample. In general, it is possible to vary the emissivity of the emitter by changing the heating current or the electric field in front of the emitter [93,

98, 99, 147]. The electrical circuit of the ion source, including the emitter and the repeller lens is shown in figure 26, where R is the resistance of the heating circuit.

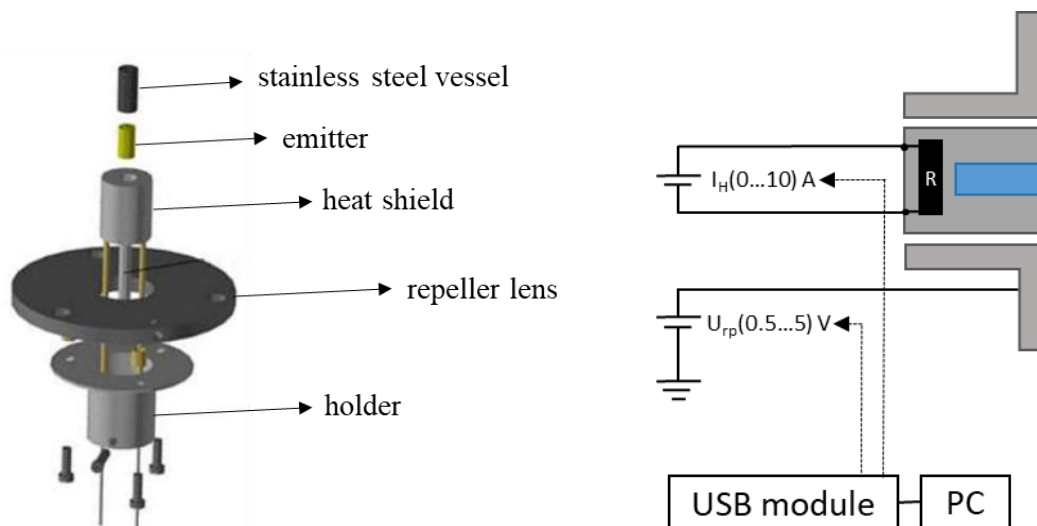


Fig. 26: The assembly of ion sources is presented on the left [148], while the electric circuit diagram on the right.

Emitter type b:

In the present work, synthetic spodumene ($\text{LiAlSi}_2\text{O}_6$) has been chosen as the material for the Li^+ ion emission. The spodumene was prepared by a solid-state reaction, where a stoichiometric mixture of Li_2CO_3 , Al_2O_3 and SiO_2 (1:1:4) was ground in a planetary ball mill and squeezed into a corundum tube. The mixture was heated to $1200\text{ }^\circ\text{C}$ while exposed to air for 24 hours. After grinding, the sample was annealed at $1200\text{ }^\circ\text{C}$ for 48 hours to obtain a homogeneous sample. The spodumene was suspended in isopropanol, which acts as a solvent, and then dropped onto a central spot of $1\text{ mm} \times 5\text{ mm}$ of a molybdenum ribbon (effective dimensions: $1.0\text{ mm} \times 20\text{ mm} \times 0.05\text{ mm}$). After drying at atmosphere (evaporation of isopropanol), the ribbon was assembled onto a resistively heated mount. This constitutes a filament type emitter. The preparation is finished by brief heating the sample in a high vacuum above the melting point in order to improve the contact between the sample and filament (see figure 27). The actual emitter setup consists of stainless steel support, which is equipped with two copper mounts to hold the

filament in place. These copper mounts are electrically insulated from the support plate by ceramic tubes. The emitter is heated by applying a current to the filament. The applied heating voltage is floating on top of the filament voltage (U_{rp}), which is used to accelerate the ions.

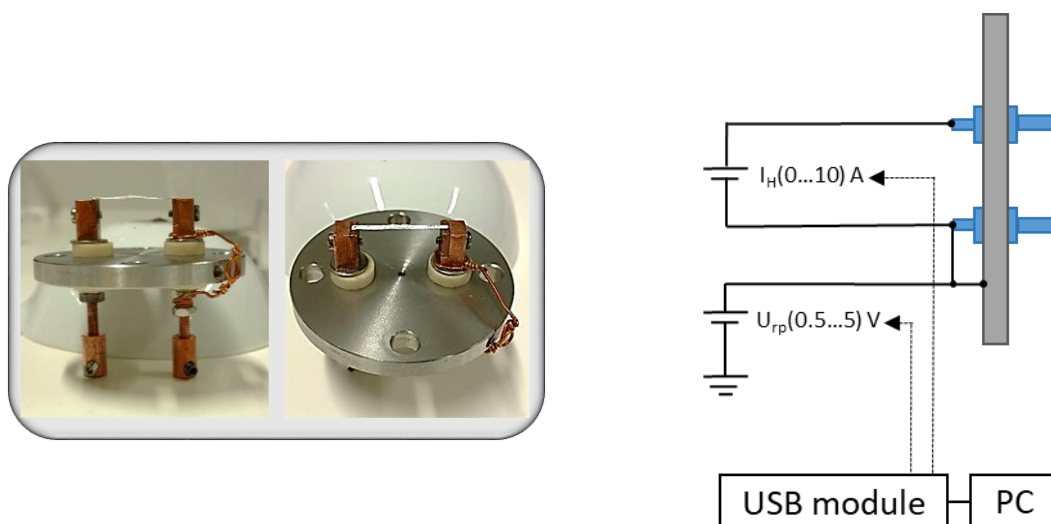


Fig. 27: Pictures of the emitter *type b* is presented on the left, while the electric circuit diagram on the right.

4.1.2 Ion optics and sample holder

Here the focus will be given to the description of the electrostatic lens system, as well as of the sample holder. In a general CAIT experiment, the ions are guided and focused towards the sample via an ion optics consisting of a system of electrostatic lenses. A continuous positively charged ion beam ($M^+ = K^+, Rb^+ \text{ or } Li^+$) is generated from thermionic emission by heating the ion emitter material. The ion beam source is focused directly towards the surface of the sample after the ions are repelled by a positive potential, U_{rp} , applied to a repeller lens. This voltage ultimately defines the initial kinetic energy of the ions in the laboratory frame. The repelled ions are then further accelerated towards the sample via the abstraction lens. The voltage applied to the abstraction lens is chosen in such a way that the field in front of the emitter remains constant. The constant field combined with the appropriate guiding through the electrostatic ion optics (see lens system L1 to L6 in figure 25) guarantees a spatially homogeneous ion beam of constant

intensity. Some of the lenses are powered by electrical power sources that were built from the electronic workshop of the department of chemistry in Marburg. With these power sources, it is possible to provide a heating current for the emitter of up to 10 Ampere and a repeller voltage between 0 V and 200 V. Home-made high voltage power sources are used for the abstraction lens AL and the lens L5, which provide an abstraction voltage between 0 V and -3 kV and a focusing voltage up to +/- 2 kV respectively. After leaving the ion optic, the ions pass through an aperture mounted in front of the sample and set to ground potential. Both sides of the central opening of the aperture are covered with nickel meshes (95% transmission), to guarantee a homogeneous field in front of the sample so that the ions may move freely towards the sample surface with well-defined kinetic energy. A mask is used to define the bombarded area of the sample. The diameter of the mask is 4 mm. The ions impinging on the front surface of the sample lead to the formation of a surface potential and a surface particle density. Since the backside of the sample is glued onto an electrode and that electrode is grounded, a potential and particle density gradient toward the backside of the electrode arises. This induces the ion transport through the sample due to the laws of electrodiffusion. Ions reaching the backside electrode are neutralized and give rise to neutralization current that is detected there. An electrometer amplifier is used to measure the ion currents in the range of nano-Amperes. The detector consists of two components (OP in figure 25): a pre-amplifier Balzers EP 511 together with an amplifier Balzers QME 311 which can detect the ion current in the range between 10^{-5} Amp and 10^{-11} Amp. The amplifier is provided with a range switcher which allows to choose for the more suitable range of detection. In particular, with respect to the measurements conducted within the thesis a range with detection limit of ± 10 nA has been chosen. The current is converted with a 12 digit analog-to-digital converter (A/D) leading to a resolution of the measured current of 4.9 pA. Eventually the detected current is processed in a personal computer. The temperature of the sample can be controlled via a PID-controller (Eurotherm 3216) coupled with a PT-100 and an home-made heating device. This system allows temperature dependent measurements in the range 50 °C - 250 °C. Finally, the set up is placed in a high vacuum chamber and all the measurements are performed at a pressure value of $10^{-6}/10^{-7}$ mbar so that the charged particles can have a mean free path long enough to pass from the ion source to the sample without being scattered. The vacuum chamber is a non-magnetic stainless steel cylinder constructed from stainless steel flanges that are sealed with copper ring gaskets. A turbo

molecular vacuum pump (Edwards, EXT75DX CF63) is connected at one end of the setup which works in the region of molecular flow but cannot operate directly against atmospheric pressure. In principle, the turbo molecular pump requires an initial pressure of about 10^{-2} to 10^{-3} mbar and therefore, a dry and oil-free diaphragm pump (MVP 015) is also used as backing pump. The vacuum pressure of the setup is measured by a cold cathode ionization gauge and displayed with a controller (Pfeiffer Vacuum TPG-300). Finally, the measurement data are recorded in the computer with the help of LabVIEW (laboratory virtual instrument engineering workbench) software programs. LabVIEW is a powerful software system that accommodates data acquisition, instrument control, data processing and data presentation, and can run on PC under Windows.

4.2 Samples preparation

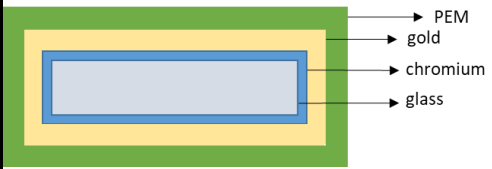
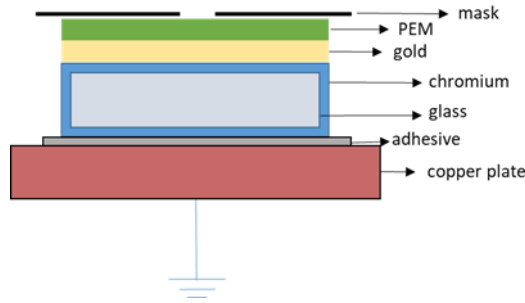
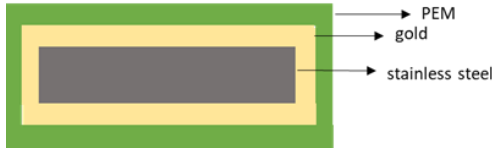
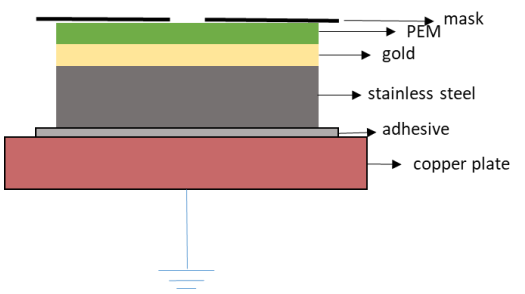
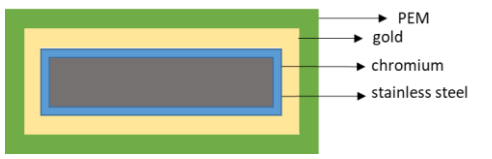
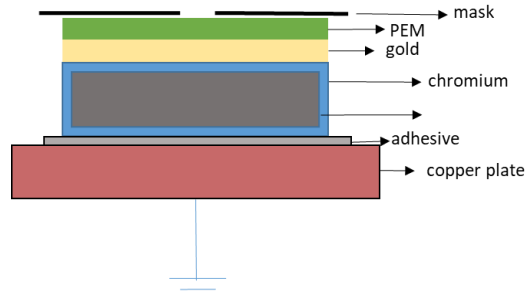
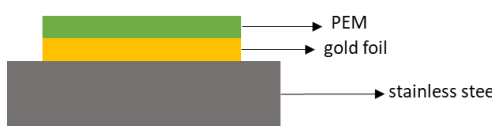
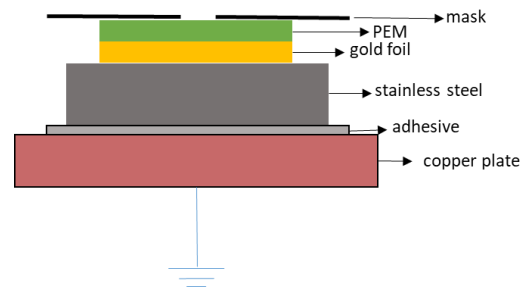
4.2.1 Substrates and polyelectrolyte multilayers preparation

Substrates construction

Within the research of this study, different types of substrates for the preparation of the PEMs have been used. The type of substrate has been adjusted to the special requirements of the sample preparation procedure and the desired CAIT and ToF-SIMS measurements. In the following sections, an overview over the different substrates used for the preparation of the PEMs will be given. For a better visualization, a graphic 2D illustration is provided below, while a more detailed description is given in the relevant subsections. In section 5.2 the results of the experiments conducted using the different substrates will be presented, together with a discussion of the data.

4 Experimental part

Table 1: A graphic representation of the different types of substrates used. On the left column a cut-side view of the PEM-coated substrate; on the right column the same view but after mounting the sample on the sample holder.

DESIGN I	 <p style="text-align: right;"> → PEM → gold → chromium → glass </p>	 <p style="text-align: right;"> → PEM → mask → gold → chromium → glass → adhesive → copper plate </p>
DESIGN II	 <p style="text-align: right;"> → PEM → gold → stainless steel </p>	 <p style="text-align: right;"> → PEM → mask → gold → stainless steel → adhesive → copper plate </p>
DESIGN III	 <p style="text-align: right;"> → PEM → gold → chromium → stainless steel </p>	 <p style="text-align: right;"> → PEM → mask → gold → chromium → stainless steel → adhesive → copper plate </p>
DESIGN IV	 <p style="text-align: right;"> → PEM → gold foil → stainless steel </p>	 <p style="text-align: right;"> → PEM → mask → gold foil → stainless steel → adhesive → copper plate </p>

Design I

Glass slides (producer: Präzisions Glas & Optik GmbH) of size 25 mm x 25 mm x 0.499 mm were used as precursor substrates. The pieces of glass were first treated with a 20 seconds-long plasma discharge to improve the cleaning status of the surface, then a 20 nm chromium adhesion layer was sputter-coated all around the glass slides, followed by a gold layer of 300 nm [Sputter Coater ACE 600 from Leica]. Such substrates represent the support for the preparation of the membranes (see later for details in procedure). From the PEM-coated samples, the back and lateral sides of the coverage were removed by means of sandpaper, in order to avoid any contact between the polymeric film lying on top of the substrate and the copper plate below. The mounting of the samples occurred via a double component resin (PT EC 112-L and PT EC 101; producer: Polytec PT). A copper electrode was used as current collector in the sample holder.

Design II

Stainless steel pieces of dimension 15 mm x 15 mm x 1 mm were used as the precursor substrate, instead of glass. The coverage occurred directly with a 300 nm thick layer of gold. After functionalization with the PEM film, the substrates were partially polished as already mentioned in the Design I and finally mounted on the copper electrode, using the double component resin as the adhesive layer.

Design III

This type of design appears to be identical to the design I, except that the glass has been replaced by steel substrate. A 20 nm thick layer of chromium was sputtered, followed by a 300 nm layer of gold. The samples were fixed to the sample holder via the double component resin glue.

Design IV

The last construction differs from the Design I, II and III in the gold layer, which is no more a sputter-coated coverage, but rather a massive gold foil (purity: 99.99%; producer: HMW Hauner) of dimension 8 mm x 8 mm x 0.5 mm. However, the same procedure illustrated for the previous Designs has been applied to fasten the samples to the sample holder.

Polyelectrolyte multilayers formation

Sample materials

A 3 mg/mL solution of poly(allylamine hydrochloride) was used as cationic polyelectrolyte and a 1.5 mg/mL solution of p-sulfonato-calix[8]arene as anionic counterpart (figure 28).

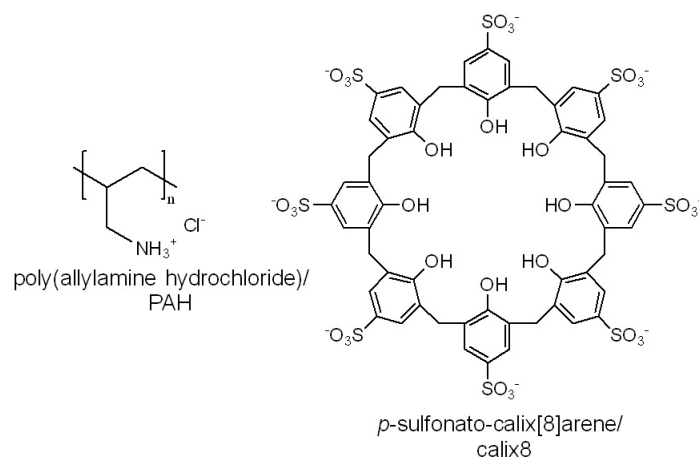


Fig. 28: Representation of cationic polyelectrolyte (PAH) and anionic calixarene (calix8).

The gold layer (see section above for details) was functionalized with 1mM 3-mercaptopropionic acid in ethanol. Water used in all experiments was prepared in a three-stage “Milli-Q” purification system to a conductivity less than 1 μ S/cm.

Table 2: Building blocks for the preparation of PEMs.

<i>Material</i>	<i>Specific.</i>	<i>Producer</i>	<i>Linear formula</i>
poly(allylamine hydrochloride)(PAH)	solution 3 mg/mL	Sigma-Aldrich ref 283223	[CH ₂ CH(CH ₂ NH ₂ ·HCl)] _n
p-sulfonato-calix[8]arene (calix8)	solution 1.5 mg/mL [1489.48	TCI America Product: S0471	C ₅₆ H ₄₈ O ₃₂ S ₈ ·xH ₂ O
3-mercaptopropionic acid (MPA)	solution in ethanol 1.218 g/mL	Sigma-Aldrich ref M5801	HSCH ₂ CH ₂ CO ₂ H
Milli-Q water	conductivity < 1 μ S/cm	[-]*	H ₂ O

*Data not known

Protocol

The first step (figure 29) in the preparation of polyelectrolyte membranes is the functionalization of the gold layer with MPA. Gold substrates were first treated with a 20 seconds-long plasma discharge to clean the substrate surface. The substrates were then anionically functionalized by immersion for 24 hours in MPA, then rinsed with Milli-Q water and finally dried with a soft and continuous stream of nitrogen.

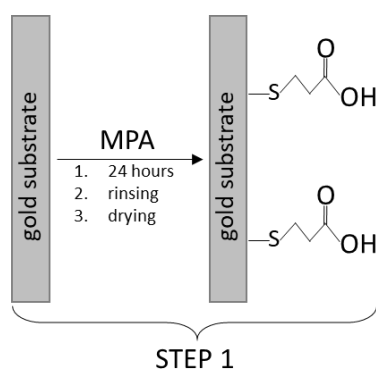


Fig. 29: Functionalization of the gold layer. The thiol group of the MPA binds to the gold surface, while the carboxylate forms, after the loss of H^+ , a negatively charged layer, providing the basic structure for the construction of the PEMs.

After preparing the MPA-modified gold substrates, the polyelectrolyte multilayers were deposited. For that purpose, the second step in the preparation of the membranes was the adsorption of the polyelectrolyte layers. To this aim, the dipping method first reported by Decher *et al.* [149, 36, 60] was used. In figure 30 this process is schematically represented: the functionalized gold substrates were dipped into a solution of PAH for 20 minutes, rinsed with milli-Q water to remove the excess of PAH and dried. The protocol was repeated by immersing the covered substrate into a calix8 solution for 20 minutes, washed again with Milli-Q water and dried. With these two steps, the first bilayer of PEM has been formed. The entire protocol of dipping, rinsing and drying was repeated as many times as wanted, leading to samples with n ($n = 1,3,6,9,\dots,30$) bilayers of $(PAH/calix8)_n$.

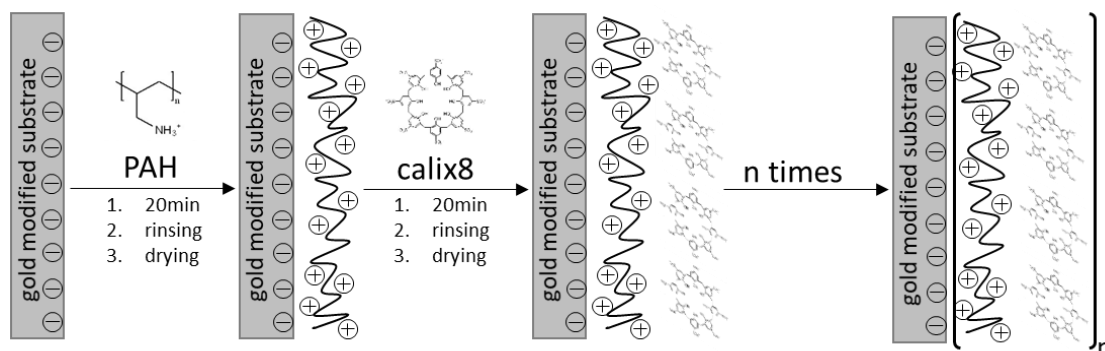


Fig. 30: The second step is based on the alternating adsorption of PAH and calix8.

Part of the functionalized samples has been prepared from Dr Jonas Hühn (AG Biophotonik W.J. Parak) at the physic department of the University of Marburg, within a collaboration project. A list of samples together with some specifications is given in table 3:

Table 3: List of samples produced within the study of this thesis.

<i>Producer</i>	<i>Protocol</i>	<i>Sample type*</i>	<i>Substrate design</i>
Jonas Hühn	161116	2 x (3,6,9,12,15)	I
Jonas Hühn	170220	(1,3,6,9,12,15,20)	I
Jonas Hühn	170516	3 x (3,6,9,12) & 4 x (15,20,30)	I
Jonas Hühn	170814	3 x (1,3,6,9,12,15,20,30)	II
Jonas Hühn	170814	4 x (15)	III
Viviana Motta	180523	6 x (15)	IV
Viviana Motta	180913	6 x (15)	IV
Viviana Motta	180918	6 x (30)	IV
Viviana Motta	181108	6 x (30)	IV

**number of bilayers under brackets*

4.2.2 Mold compounds samples

The mold compounds (MCP) used for this study were provided by Dr Stefan Schwab from the faculty of Technical Chemistry of the University of Vienna, within a collaboration project. In table 4 the specific content, as well as the nomenclature, is illustrated [11].

Table 4: Composition of the mold compounds.

<i>Sample</i>	<i>Supplier</i>	<i>Epoxy resin</i>	<i>Hardener</i>	<i>Filler</i>	<i>Flame retardant</i>
MCP1	A	Ortho cresol novolack	Phenolic	SiO ₂ 80 wt%	Metal(OH) _x
MCP2	A	Multi aromatic	Multi aromatic	SiO ₂ 88 wt%	None
MCP3	B	Ortho cresol novolack	Phenolic	SiO ₂ 82 wt%	Metal _x O _y
MCP4	B	Ortho cresol novolack	Phenolic	SiO ₂ 82 wt%	Metal _x O _y

All the samples were provided in pieces of $10 \times 10 \times 0.5$ mm and glued to a copper electrode by using a silver-containing heat conducting glue (Polytech EC 101), as shown in picture:



Fig. 31: Assembling of the mold compound sample onto a copper electrode via a heat conducting glue.

4.3 ToF-SIMS conditions

The ToF-SIMS measurements were acquired by means of a modified ToF-SIMS IV (IONTOF GmbH Münster). With regard to the mounting of the samples, two different sample holders (figure 32) were used to holder samples with different height and shape: a sample size of 13 mm x 13 mm x 10 mm must not be exceeded with the backmount, while for larger samples the topmount appears to be more suitable.

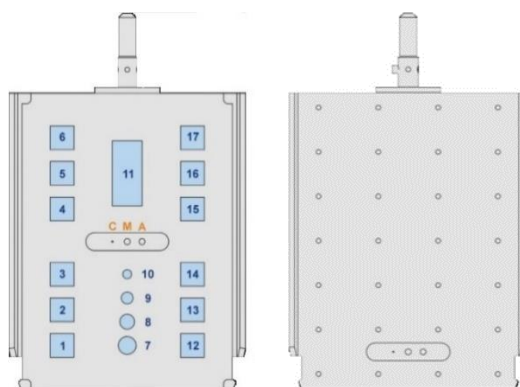


Fig 32: Backmount holder (left) and topmount holder (right). Pictures taken from the instrument manual.

Despite the wide range of sample-types which the instrument can house, in general, the samples must be flat and smooth and should never exceed a height of 20 mm; in addition, the samples require certain vacuum stability since the measurements are performed under reduced pressure in the range 8×10^{-8} to 3×10^{-9} mbar. The sample holder is transferred from the first chamber (pressure in the order of 10^{-7} mbar), to the main one via a lock system, consisting of an intermediate chamber and a series of gates to separate the different rooms.

The measurements were carried out with Bi^+ or Bi^{3+} (for higher carbon sensitivity) as a primary ion in *high current bunched mode* with an energy of 25 keV and an ion current of 0.5 pA - 1 pA. The ion current was pulsed with a pulse width between 6.6 ns and 9.3 ns. The sputtering species used were both O_2^+ with an energy of 3 keV and an ion current in the range of 140 nA - 240 nA and Cs^+ with an energy of 3kV and ion current between 18 nA - 30 nA. To avoid positive charging of the sample surface during the measurements, an electron gun with an energy of 20 eV was used. Before each depth profiling analysis, 10 mass spectra were recorded for calibration: this procedure occurs

by taking into account fragments or peaks of species present in the samples. The depth profiles are recorded after calibration in *non-interlaced mode*: under the conditions of this mode a consecutive measuring process takes place with 1 s - 1.5 s sputtering time and a subsequent pause of 0.5 s after which mass spectra are recorded. It must be noted that the sputtering crater is $300\ \mu\text{m} \times 300\ \mu\text{m}$, while the primary ion analysis beam only scans a range of $100\ \mu\text{m} \times 100\ \mu\text{m}$ in the middle of the sputtering crater, in order to avoid crater edge effects. Eventually, the evaluation of the data occurs with the program SurfaceLab 6.1 and 6.5 (IONTOF GmbH Münster).

4.4 Dektak

As profilometer, a Sloan Dektak3ST from Veeco Instruments was used to determine the crater depth. The instruments provide different levels of high resolution depending on the thickness of the crater to be measured. In the measuring range of $65\ \text{k}\text{\AA}$, a resolution of $1\ \text{\AA}$ can be achieved, while at the measuring ranges of $655\ \text{k}\text{\AA}$ and $1310\ \text{k}\text{\AA}$ resolutions of $10\ \text{\AA}$ and $20\ \text{\AA}$ are achieved. Assuming that craters formed via a ToF-SIMS analysis are rarely deeper than $1\ \mu\text{m}$, then the best resolution for the samples studied in this work could be achieved. Ultimately five measurements were taken to determine a realistic average crater depth and it was assumed that the sputtering rate remained constant during the entire ToF-SIMS measurement.

5 Results and discussion

5.1 MCP results and discussion

This section is divided into two parts. The first part (section 5.1.1) concerns the evaluation of the ionic conductivity and activation energy related to the process of transport of potassium ions through four types of mold compounds MCP1, MCP2, MCP3, MCP4 (see section 4.2.2 for description). In the second part (section 5.1.2) the diffusion of potassium through a mold compound of the type MCP3 has been investigated via an ex-situ ToF-SIMS analysis, which revealed a depth diffusion profile of the potassium into the material. Furthermore, a mathematical theory has been established in order to evaluate a diffusion coefficient for the transport of potassium ion thorough the specific mold compound and in order to suggest a model for the mechanism of the ion transport.

5.1.1 Conductivity measurements and activation energies

In the following section, the steady-state backside current was investigated as a function of the ion kinetic energy for different sample temperatures. First, an overview of the detected ion currents for different repeller voltages is given. Then the activation energy of the ion transport is investigated by analyzing the temperature dependence of the specific conductivity.

The backside current I_{back} has been detected as a function of the kinetic ion energy that is determined by the voltage applied to the repeller lens U_{rp} . Therefore, the time characteristic of the backside current was recorded for each repeller voltage and temperature. As an example, the characteristic for $U_{\text{rp}} = 30 \text{ V}$ and $T = 170 \text{ °C}$ is shown below in figure 33. The increase of the current at about 15 s marks the start of the measurement. After some seconds of decaying current, the backside current reaches a stationary state which yields the current value that has been used for the subsequent analysis of the conductivity and the activation energy.

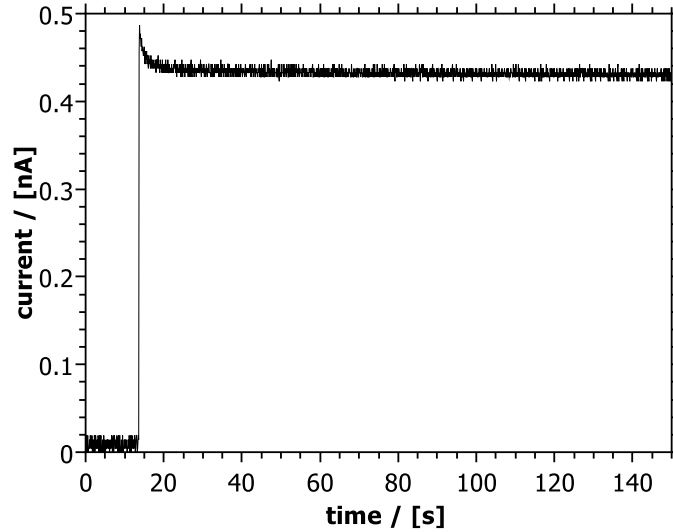


Fig. 33: Time dependence of the backside current for an MCP1 sample at 30 V and 170 °C.

Within the experiments of this work, the backside current was measured for repeller voltages between 5 V and 30 V. In order to guarantee that the surface potential equals U_{rp} everywhere, the corresponding blind current was chosen sufficiently large. Because a homogeneous ion beam leads to the largest backside currents, the voltage applied to the focus lenses has been adjusted such that I_{back} is maximized for each repeller voltage. The results of the measurements are shown in figure 34, where the backside current is depicted for $T = 150$ °C, 155 °C, 160 °C, 165 °C and $T = 170$ °C as a function of the repeller voltage.

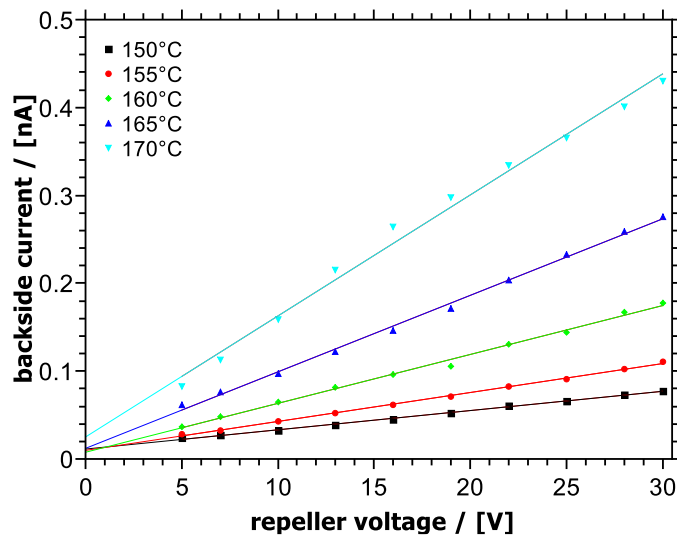


Fig. 34: Temperature dependent current–voltage characteristic of the sample MCP1.

It is observed that the backside current data-points lay on a straight line for every temperature applied in a very good approximation, indicating Ohm's law-like behavior. Therefore, the actual conductance $G = \Delta I_{\text{back}}/\Delta U_{\text{rp}}$ (equation 36) can be derived via the slope of a linear regression of the data points. Combining the conductance with the sample thickness (0.5 mm) and the size of the bombarded area leads to a conductivity of approximately 10^{-12} S/cm. In the table below, the values of the calculated conductance and conductivity are listed for the different temperatures used in the experiment.

Table 5: values of conductance G and conductivity σ evaluated from the slope of the linear regression of figure 34.

T (°C)	Conductance G (S)	Conductivity σ (S/cm)
150 °C	2.19E-12	8.29E-13
155 °C	3.29E-12	1.25E-12
160 °C	5.56E-12	2.11E-12
165 °C	8.71E-12	3.30E-12
170 °C	1.38E-11	5.22E-12

Similar conductivity values have been found in the literature for the same type of mold compound MCP1 [12]. The here determined conductivity values agree with the values given in [12] within the error margins of the CAIT measurement. In [12] the authors affirm that the current values measured at 150 °C are in the range of the detection limit of the measurement setup, verifying that the temperature has a large effect on ion migration, especially when comparing the results found at 150 °C to the ones achieved at higher temperatures. This aspect is not surprising, considering the low ion concentration and low ion mobility characteristic of the mold compounds. Ultimately all four samples show a similar current-voltage characteristic such that only plots for the sample MCP1 are shown in this section (see appendix A2 – A4 for results of samples MCP2, MCP3 and MCP4). From the conductivities, the activation energy for the transport can be calculated via equation 61:

$$\sigma T = \sigma_0 \exp\left(-\frac{E_{act}}{k_B T}\right) \quad (61)$$

Where σ is the conductivity, σ_0 is the pre-exponential factor, k_B is the Boltzmann constant and T is the temperature. Consequently, the slope of a linear regression of the data points where $\ln(\sigma T)$ is plotted as a function of the inverse temperature, yields the activation energy.

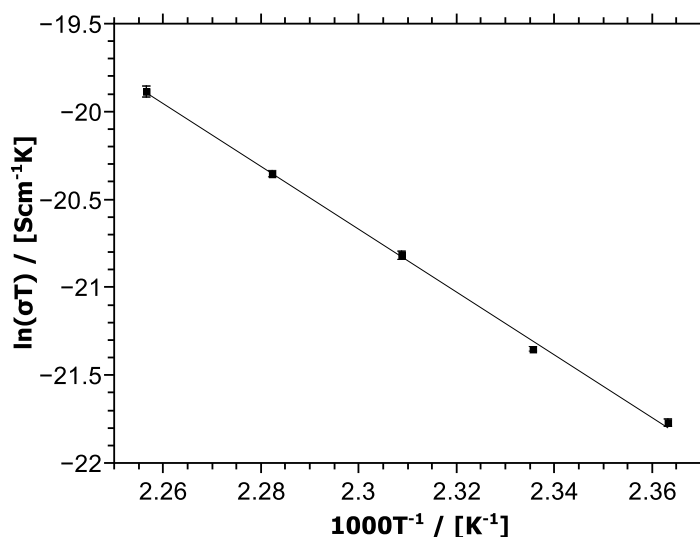


Fig. 35: Temperature dependence of the specific conductivity for MCP1 sample.

The value of E_{act} derived from the slope of the linear regression of figure 35 is 1.54 ± 0.03 eV. The conductivity measurements have been repeated several times to check for the reproducibility, leading to the conclusion that from the same type of mold compounds, e.g. MCP1, slightly different values of conductivity, as well as activation energies, are obtained. In figure 36 the temperature dependence of the specific conductivity for different measurements conducted on the mold compound of type MCP1 is presented:

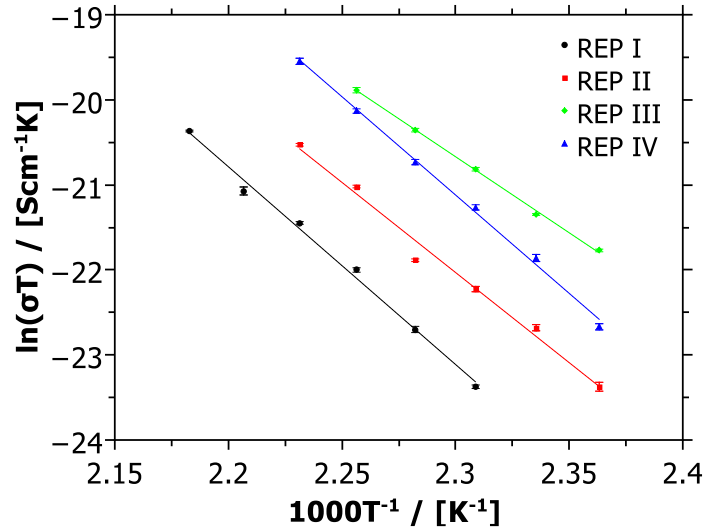


Fig. 36: Temperature dependence of the specific conductivity for different reproduction measurements of the MCP1.

The activation energy values evaluated from the linear regression of the curves are listed in table 6:

Table 6: Activation energy values evaluated for the same type of mold compound MCP1.

	$E_{act} (eV)$
<i>REP I</i>	2.00 ± 0.08 eV
<i>REP II</i>	1.83 ± 0.11 eV
<i>REP III</i>	1.54 ± 0.03 eV
<i>REP IV</i>	1.99 ± 0.05 eV

Previous literature data [12] showed activation energy values of 1.5 eV – 1.6 eV for mold compound of the type MCP1. It is necessary to emphasize that, not only the measurement system used in [12] differs from the CAIT approach, but a crucial point might be the vacuum condition under which the CAIT method operates. It is not automatically known, to which extend the vacuum may influence the possible evaporation of water content or other components out of the mold compound, leading to a change in the ion conduction properties. The last point could give moreover an explanation of the difference in the conductivity and activation energies within the reproduction measurements. In order to verify whether the vacuum system may or may not influence the ion conductivity, an experiment on a mold compound of the type MCP4 has been performed, where the sample

was left into the measuring setup under vacuum conditions for five consecutive days and temperature dependent current-voltage characteristics have been measured each day of permanency in vacuum. The results are shown in figure 37:

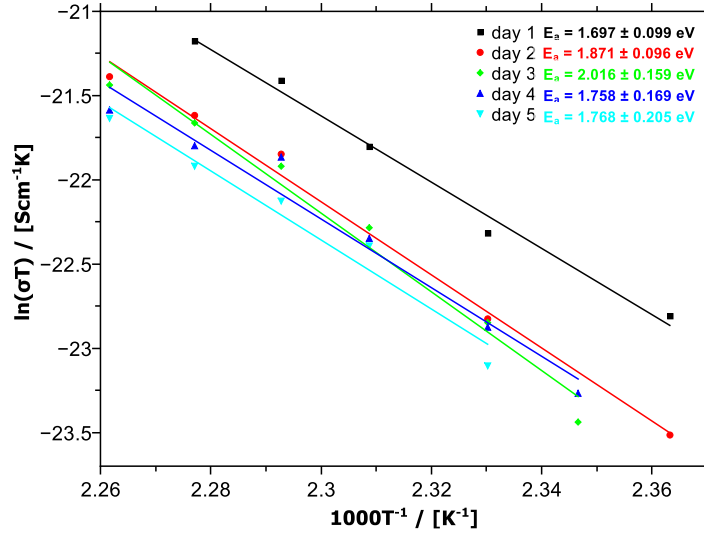


Fig. 37: Temperature dependence of the specific conductivity for an MCP4 measured daily for 5 days while permanency under vacuum conditions.

A dropping on the conductivity can be seen as a result of this analysis, while the activation energies values continue to vary within a certain error margin around an average value of 1.82 eV. However, this analysis is limited in the fact that it does not prove whether the reduction in the conductivity is due to the vacuum solely, or whether the daily variation of the temperature from 150 °C to 170 °C and back again to 150 °C has somehow induced changes in the material such that the ion conduction properties have changed in turn. To shed further light onto possible changes in the material, the results of an extra analysis will be presented subsequently. Some of the samples have been treated with heat, in order to see whether that would have caused modification on the conductivity or on the activation energy values. The heating process consisted of heating the substrate inside an ambient pressure oven from 130 °C up to 250 °C in steps of 5 °C every 5 minutes. Before treating the mold compound with high temperature, conductivity and activation energy values have been measured via CAIT. Right after the thermal treatment of the sample, a new CAIT analysis has been performed. Surprisingly very low backside current has been detected, being close to the detection limit of the detector. For that reason, no temperature dependent current-voltage characteristic could be determined. From the literature, it is

already known that, due to the heterogeneous composition of this kind of materials, the mechanical properties of polymer encapsulating compounds, e.g. mold compounds, change considerably when packages are exposed to elevated temperatures for a long time. Whilst it is generally agreed that after prolonged exposure to high temperatures the polymer chains would break down [150], resulting in a lower glass transition temperature and a lower modulus, however, in literature also studies which show an increase in the glass transition temperature can be found [151]. In a study of the 2010 Jansen *et al.* [152] reported the change in viscoelastic properties of a commercial mold compound which was stored at 175°C for a period of 4 weeks. The study shows that instead of the expected degradation, the modulus and the glass transition temperature increased and these effects are accompanied by a relatively large amount of shrinkage. All effects can be interpreted in terms of the formation of an oxidized layer where extra crosslinking occurred. Therefore, the drop out of the ionic current measured after thermal treatment, could be explained assuming a change in the inner structure of the material which lowered the ion mobility inside the sample. In the frame of product life and reliability, this last observable rises the question of whether mold compound materials remain stable under high temperature conditions. Nowadays indeed electronic packages are also used in automotive applications where they are mounted close to the engine under exposure to temperatures of 200 °C or more.

In the final part of the study regarding conductivity and activation energy values of the mold compounds, a comparison of the data obtained by means of two different techniques is presented: from the one hand the CAIT method and from the other hand the *electrochemical impedance spectroscopy* (EIS) technique conducted from Dr. Schwab at the chemistry department of the University of Vienna (data allowed from the owner).

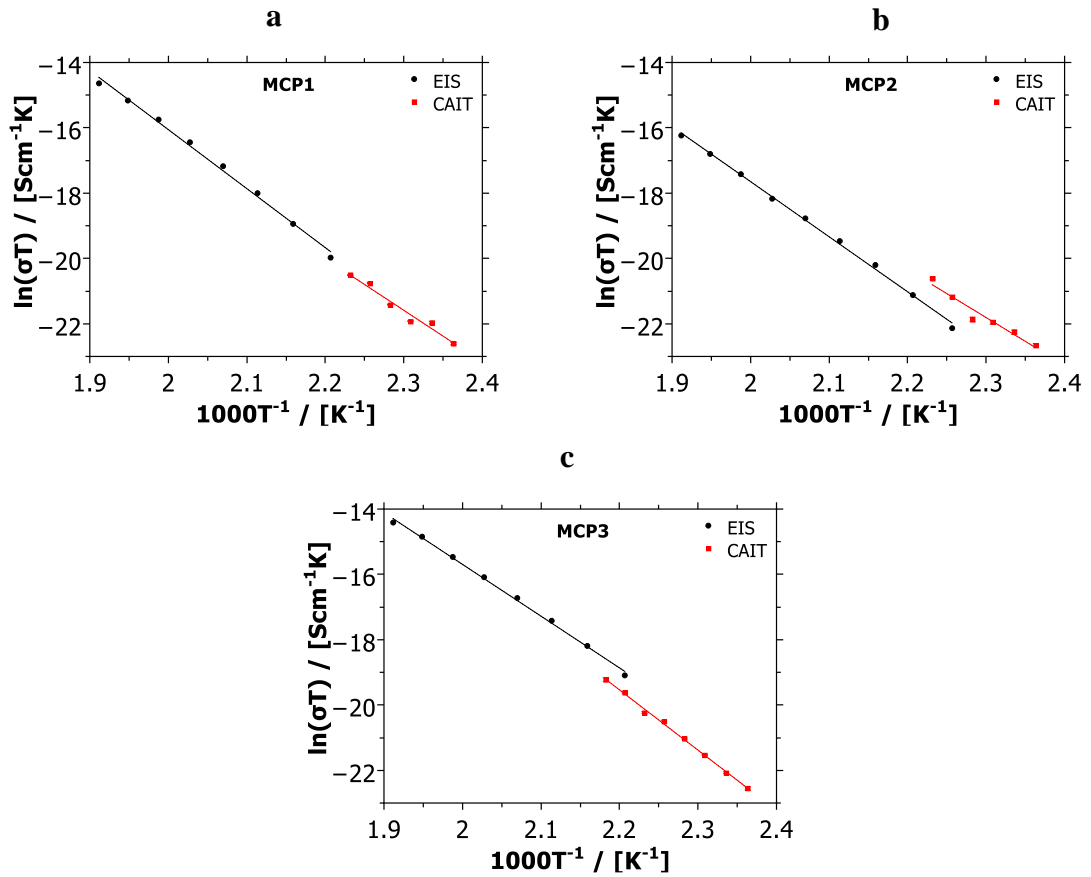


Fig. 38: Temperature dependence of the specific conductivity. Data according to EIS and CAIT methods for samples MCP1 (a), MCP2 (b) and MCP3 (c).

The graphs in figure 38 show that the results achieved with the two different methods are in good agreement, although EIS results measured at temperatures below 170 °C could not be evaluated since the impedance exceeded the limit of the EIS analyzer. In the table below the values of the corresponding activation energies are listed:

Table 7: evaluated activation energies from the slope of the linear regression of curves of fig. 38.

	$E_{act}(\text{eV})$ CAIT*	$E_{act}(\text{eV})$ EIS
<i>MCP1</i>	1.36 ± 0.06 eV	2.00 ± 0.08 eV
<i>MCP2</i>	1.26 ± 0.02 eV	1.45 ± 0.02 eV
<i>MCP3</i>	1.59 ± 0.01 eV	1.37 ± 0.03 eV

*data for MCP4 not available

* E_{act} CAIT values are averaged values over four measurements

5.1.2 Diffusion of potassium through MCP3 and numerical simulations

For a better understanding of the potassium diffusion process into the mold compound, 19 days-long bombardment onto an MCP3 with a potassium ion beam has been performed. The kinetic energy of the potassium beam was set to be 19 V and the temperature was 170 °C throughout the experiment. At the end of the experiment, a circular area of 4 mm as diameter was bombarded and a charge of 0.025 mC was incorporated into the material. The registration of a concentration depth profile was possible via an ex-situ ToF-SIMS analysis. The analysis occurred in positive mode, thus concentration profiles of only positive ions are shown below. In Figure 39 the result of the ToF-SIMS analysis is presented.

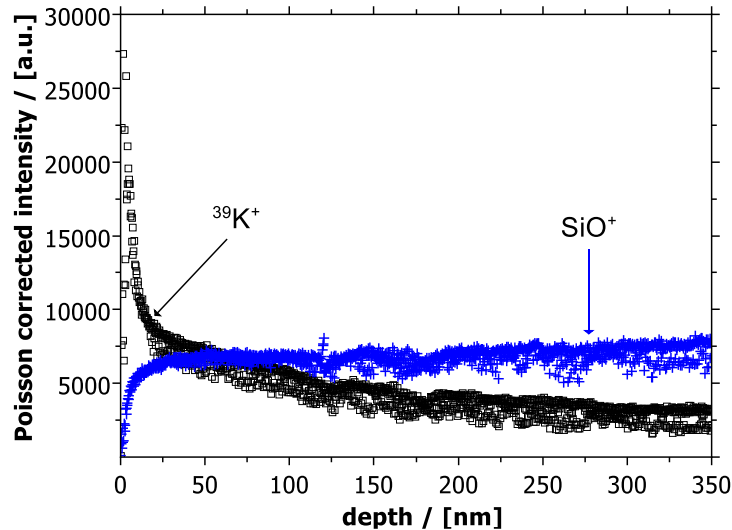


Fig. 39: ToF-SIMS of the MCP3 sample bombarded with a K^+ ion beam of kinetic energy of 19 V. Signal: black squares for $^{39}\text{K}^+$ (bombarder ion), blue crosses for SiO^+ (representative of the MCP).

The black squares show the $^{39}\text{K}^+$ signal which is representative for the potassium diffusion into the mold compound. The blue crosses for SiO^+ are representative of the main component of the MCP3, i.e. SiO_2 . The Dektak 3ST instrument has been used in order to transform the sputter time into a sputter depth, by measuring the height of the ToF-SIMS crater formed as a result of the depth profiling. Assigning the total sputter time to the total crater depth and assuming a constant sputter rate allows determining a real space depth axis. The first 15 nm of the profile are difficult to interpret since the detection probabilities

in the ToF-SIMS may vary in this regime. Except for the first 15 nm, a depth diffusion profile of the potassium through the first 350 nm of the sample can be seen in figure 39.

In order to identify migrated ions which were present into the material already prior to the bombardment, other ions species besides the $^{39}\text{K}^+$ were inspected. Assuming that most of the migrated ions into the mold compounds are alkali metal and halogen [153], traces of the most meaningful species were investigated. For simplicity reasons, the term K^+ will refer to $^{39}\text{K}^+$ along the entire section. The depth profiles for K^+ , Na^+ , F^+ , SiO^+ , SiF^+ and SiCl^+ are depicted in figure 40 in a linear and logarithmic scale.

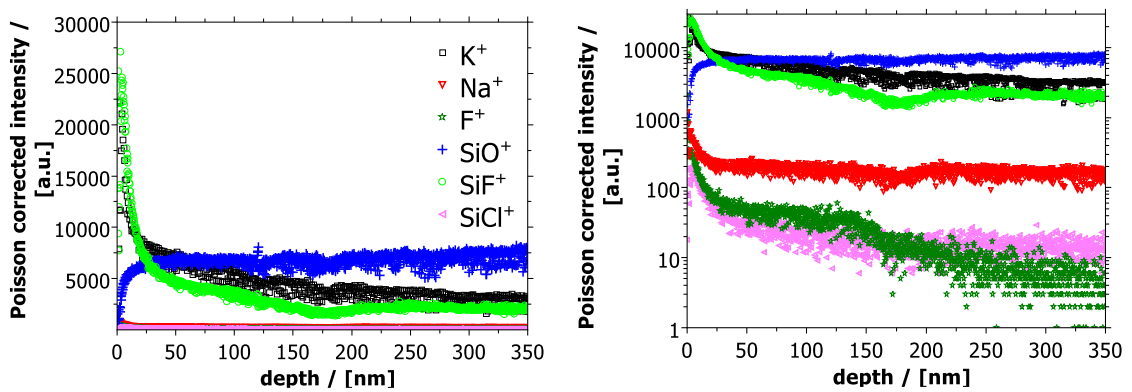


Fig. 40: ToF-SIMS of the MCP3 sample bombarded with a K^+ ion beam of kinetic energy of 19 V. Left: K^+ , Na^+ , F^+ , SiO^+ , SiF^+ and SiCl^+ depth profile in linear scale. Right: same depth profiles in logarithmic scale.

In figure 40 signals for K^+ and SiO^+ are shown for comparison reasons but they have been already discussed in figure 39. The interpretation of the traces of figure 40 is not univocal in the first 15 nm – 20 nm. As already mentioned indeed the detection probabilities in the ToF-SIMS could vary in that regime. The Na^+ signal (red triangles) does not represent a diffusion profile, it rather assumes a flat and constant trend over the depth. The same is not true for the F^+ and SiF^+ signals. On the left plot of figure 40, it can be seen that the SiF^+ signal (green ellipses) resembles somehow the K^+ signal (black squares). The F^+ signal (dark green stars) assumes the same tendency of the SiF^+ (better depicted in the right plot of figure 40). The intensity of the F^+ results to be two orders of magnitude lower than the one of the SiF^+ . The last observable does not surprise considering that the measurement has been conducted in positive mode, although very likely the fluorine is

present as F^- in the mold compound and it is extremely sensitive in negative mode rather than in positive mode. For the same reasons, any Cl^+ signal could be detected in positive mode, although it could have been reasonable to investigate its trace. Despite that, $SiCl^+$ signal has been investigated and the pink triangles show a trend which is similar to the one of the SiF^+ and F^+ . The analysis of the traces of figure 40 does not allow however to conclude whether the trend of the F^+ , SiF^+ and $SiCl^+$ signals is due to a diffusion of the species toward the front side caused from the bombardment, or whether they correlate with the inner structure of the mold compound. If this latter is the case, it is not clear from the analysis of figure 40, whether the trend of the F^+ , SiF^+ and $SiCl^+$ signals is the result of a change in the inner structure of the material due to the bombardment. In a study of the 2017 Hein *et al.* [154] realized that the detection probabilities of some structured related species may change when the structure of the sample is modified due to the introduction of charge carriers from an external source. In order to confirm or exclude any change in the local structure of the mold compound due to the bombardment, a ToF-SIMS analysis onto a fresh and not-bombarded sample of the type MCP3 has been conducted. The result of this analysis is presented below. The plots of figure 41 show intensity signals of K^+ , Na^+ , F^+ , SiF^+ and $SiCl^+$ in a linear and logarithmic scale for an untreated sample MCP3.

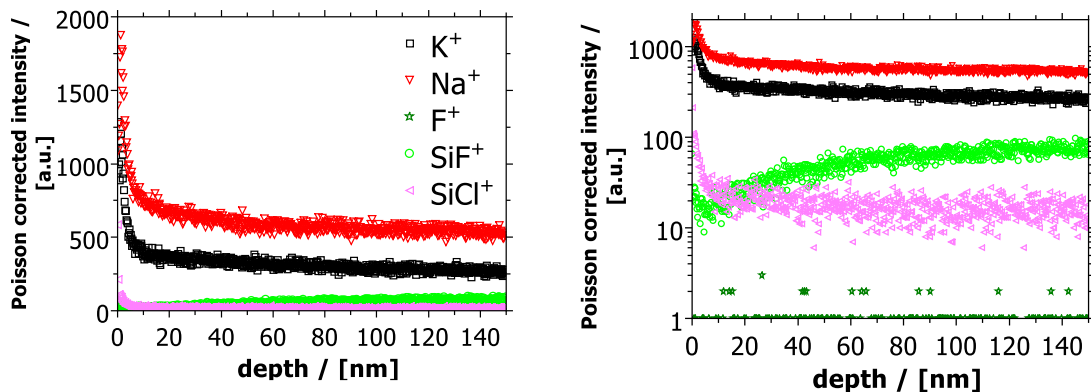


Fig. 41: ToF-SIMS of the fresh MCP3. Left: K^+ , Na^+ , F^+ , SiO^+ , SiF^+ and $SiCl^+$ depth profile in linear scale. Right: same depth profiles in logarithmic scale.

In the plot on the left of figure 41, Na^+ and K^+ signals show a very similar trend and both can be considered as related to the content of sodium and potassium ions inside the mold

compound. The intensity level of the Na^+ signal in figure 41 does not seem to differ significantly from the intensity level of the Na^+ of figure 40. The same is not true for the K^+ . A comparison between the intensity level of the K^+ of figure 40 and 41 shows a difference of more than two orders of magnitude, which reflects the incorporation of potassium ions due to the bombardment. From the right plot of figure 41, a better visualization of the F^+ , SiF^+ and SiCl^+ signals is possible. It is clear how the SiF^+ and F^+ signals differ from the ones of figure 40 in the intensity level: both SiF^+ and F^+ signals show a dropping in the intensity level of two orders of magnitude. Furthermore, none of the two seems to show a migration profile as the one they assumed in figure 40, instead, the intensity level of both SiF^+ and F^+ remains almost constant along the 150 nm of the analyzed fresh sample. The SiCl^+ of figure 41 does not show any significant difference from the one of figure 40 with respect to the intensity level, whereas the diffusion profile shown from the SiCl^+ in figure 40 seems to be less pronounced or even absent in figure 41. From the comparison between the depth profiles of figure 40 and the ones of figures 41, it seems reasonable to exclude the hypothesis of a structural change in the material due to the bombardment. If it was the case, the SiCl^+ signal would differ in the intensity level between the two cases, i.e. from the bombarded to the not-bombarded case, as it happens for the SiF^+ signals. Thus the thesis suggested before, of a possible diffusion process of halogen ions toward the front side of the sample appears to be more reasonable. Considering that the mold compound is an electron conductor (and to a lesser extent an F^- and Cl^- as well), the following explanation can be suggested: when cations are attached to the front of the sample, the surface is transiently electrically charged; this is immediately compensated by the transport of charge carriers in the material, e.g. F^- in addition to electrons. Within the frame of this idea, the depth profiles for SiF^+ , F^+ and SiCl^+ signal can be interpreted as caused from a diffusion toward the front side which occurred inside the sample and which was triggered from the bombardment.

Numerical simulations

Turning back to the question of the potassium concentration profile, from this point a more detailed analysis of the diffusion of potassium through the analyzed MCP3 sample will be discussed. According to equation 9 (see section 2.3.1) a plot of the natural logarithm of the concentration versus the squared depth is linear if bulk diffusion is the dominating diffusion process. The slope of such a linear relation equals $-1/(4Dt)$. From the slope and the diffusion time, a first approximation diffusion coefficient D for the transport can be estimated.

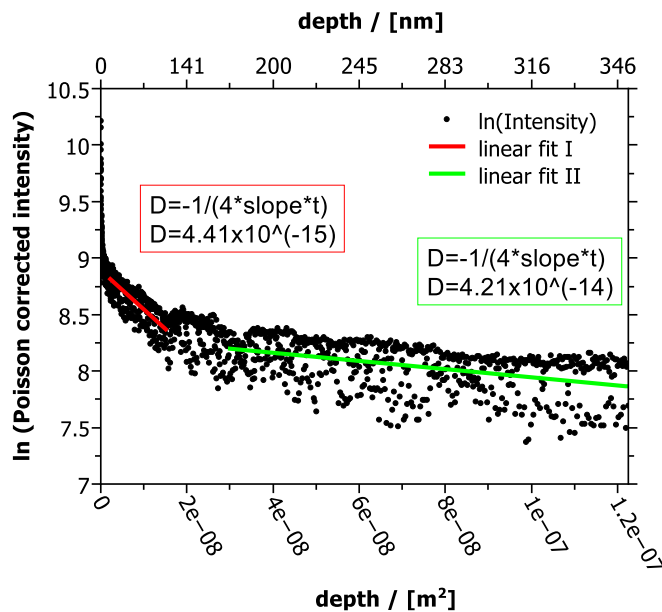


Fig. 42: plot of the logarithm of the $^{39}\text{K}^+$ signal versus the squared depth.

From the graph of figure 42, it is to notice the presence of two slopes and then two upper limiting values of diffusion coefficients associated, leading to the conclusion that the concentration profile cannot be rationalized by assuming a bulk diffusion solely. This raises the question of whether two different transport pathways may be operative. In order to answer this question and get additional information on the mechanism of transport of potassium ions into the mold compound, evaluation of 2D chemical maps collected during the ToF-SIMS analysis has been conducted. In figure 43 and 44 below pictures derived from the 2D analysis for SiO^+ , C^+ (figure 43-a and 43-b) and K^+ (figure 44) are shown. These kind of pictures, named chemical maps, are the top view of the relevant signal integrated into the z-direction. A better description is provided subsequently.

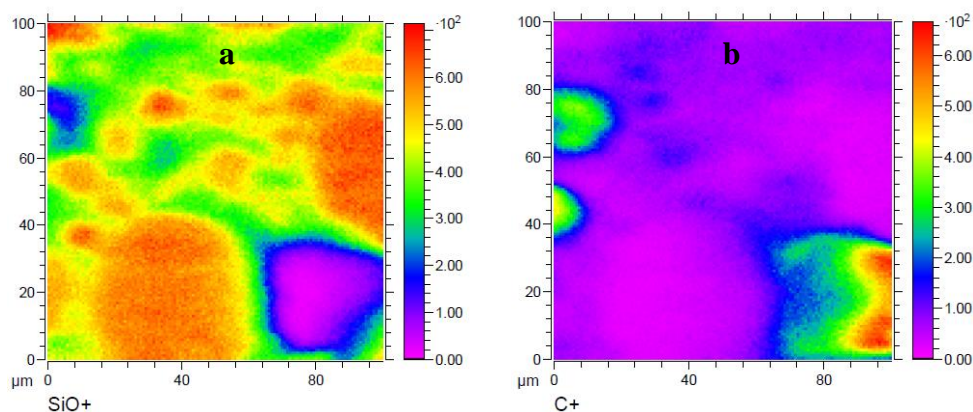


Fig. 43: Chemical maps for SiO^+ (a) and C^+ ion signal (b), i.e. a top view of the signals integrated into the z-direction.

The pictures derived from the 2D analysis employ false color coding, which is indicated next to each graph. It must be emphasized that the colors do not imply an absolute intensity since the ToF-SIMS technique is much more sensitive to potassium and silicon for example than to carbon. The comparison between the picture 43-a and 43-b above, reveals a complementarity of colors between SiO^+ and C^+ signal, which reflects the composition of the mold compound. The composition of the MCP3 consists indeed in 82% of SiO_2 and a mixture of epoxy resin, hardener and flame retardant (see Table I). In picture 43-a there are zones of accumulation of the inorganic component (orange/dark orange regions) which tend to assume a circular form. Since the 2D chemical map is actually the result of the integration of the signal over the depth, it is reasonable to refer to these circular areas as “grains”. Here below the same 2D analysis for the potassium ion signal is shown:

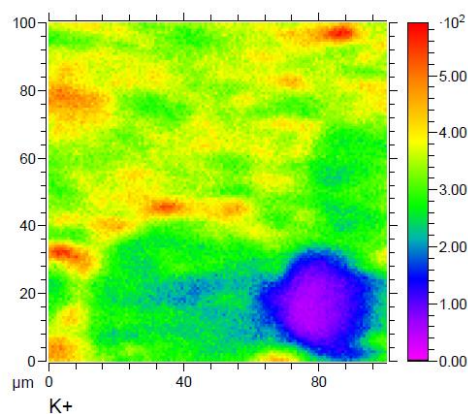


Fig. 44: Top view of the K^+ signal (c) integrated in the z-direction.

A more detailed analysis of the picture in figure 44 shows an accumulation of potassium in small circular spots placed next to the inorganic grains (for a better visualization compare figure 44 with 43-a), in a kind of complementary way. While the rest of the potassium seems to be present all over the surface except for the spot occupied from the carbon component of the mold compound (blue-violet spot in figure 44). Considering these observables, it could be said that part of the potassium diffuses along the boundaries of the inorganic grains, the rest diffuses through the bulk, i.e. through the grains, whereas no potassium passes through the organic components of the mold compound. If this is the case, then two diffusion modes seem to be present, i.e. “grain boundary diffusion” on the one hand and “bulk diffusion” on the other hand. The term bulk diffusion implicitly refers to a preferential diffusion of the potassium through the inorganic component of the mold compound. In order to shed further light on the two different transport pathways, 3D visualizations of the potassium concentration profile are presented below:

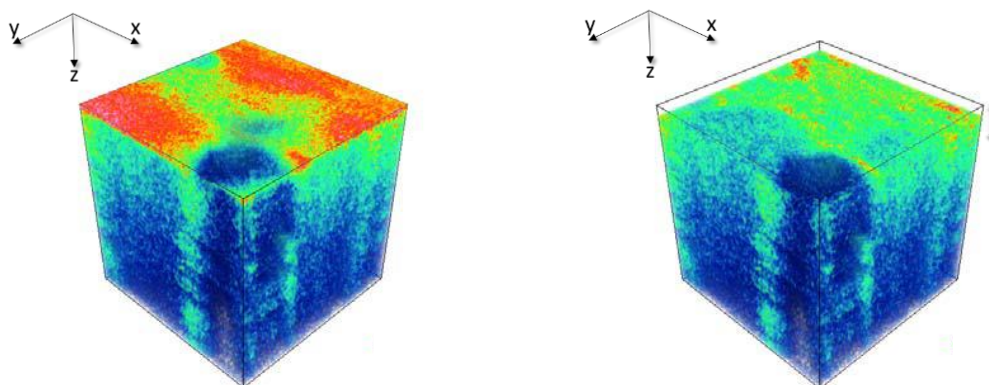


Fig. 45: 3D images of potassium. Left: whole 3D cuboid visualization. Right: same 3D cuboid with a cut of the 10% along the z-direction.

The two axes alongside the sample surface are denoted as x- and y-axis, while the axis perpendicular to the surface is the z-axis. The plots derived from the 3D analysis employ the same false color coding used for the representation of the 2D chemical maps (figure 43 and 44). Figure 45 on the left differs from the one on the right in that here the 10% of the volume rendering from the upper side of the z-direction has been cut, in order to give a better visualization on the potassium diffusion pathways. It is worth noting how the diffusion along the grain boundaries brings to a deeper penetration depth, rather than the one through the bulk. In other words, the diffusion along the grain boundaries seems to

be faster than the bulk diffusion, being in good agreement with the literature regarding bulk *vs* grain boundaries diffusion [71]. The presence of grains within the mold compounds has been validated from a *scanning electron microscopy* (SEM) analysis performed onto a fresh and not-treated sample of MCP3. In figure 46 a SEM picture of a fresh MCP3 is shown. The analysis has been conducted by Dr Noll (AG Hampp) at the chemistry department of the University of Marburg.

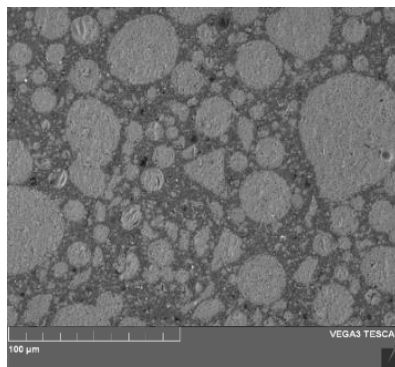


Fig. 46: SEM image of a MCP3 fresh film.

Figure 46 shows a SEM image acquired in backscattered electron mode (BSE), where a typical structure with spherical silica is visible (see circular light grey spots in figure 46). The spherical silica fillers usually have a multimodal particle size distribution to allow for high filler loadings and achieve very high packing densities. The result of the SEM analysis is the evidence that the material is a composite of organic and inorganic compounds clustered in grains. Moreover, there are grains with different diameter, between which grains with a dimension of 50 microns as diameter are visible, being this last observable consistent with the result of the analysis of figure 43-a.

Under this evidence, any theoretical model needs to take into account the diffusion alongside grain boundaries as well as the diffusion through the bulk of the material. ToF-SIMS data show that grains and grain boundaries are present even at the surface, such that the ions from the ion beam may well enter the grain boundaries directly from the surface without first passing through the bulk of the material. The first assumption in order to develop a model is that the transfer of ions from the bulk into the grain boundary, as well as vice versa, is connected with passing a significant energy barrier such that ions that are moving alongside a grain boundary remain between the grains, while ions that

are diffusion through the bulk are remaining in their grains. Therefore, the Nernst-Planck equation could be written as follows:

$$J_v = -D_v \left(\frac{\partial n_v}{\partial z} + n_v \frac{\partial \phi}{\partial z} \frac{e}{k_B T} \right) \quad (62)$$

where J is the ion flux density which depends on the diffusion coefficient D , the gradient of the ion density n and the gradient of the electric potential ϕ . The elementary charge is e and $k_B T$ is Boltzmann's constant times the temperature. The index v refers to ions in bulk ($v = B$) and ions in grain boundaries ($v = GB$) which are treated independently of each other in the Nernst-Planck equation. There is no transfer of population from bulk to the grain boundary and vice versa reflecting the assumption that the ions may not pass the material boundaries. Nevertheless, the movement of the two types of ions is yet coupled as ions positioned between the grains and ions inside the bulk of the grains contribute to the electric field via their charge. The electric potential that is given by a certain ion distribution can be determined using the Poisson equation:

$$\epsilon_0 \epsilon_r \frac{\partial^2 \phi}{\partial z^2} = -e(n_B + n_{GB}) \quad (63)$$

The boundary conditions for the electric field are essentially given by the experimental setup where the potential ϕ is forced to zero at the backside electrode and the potential at the frontside of the sample is implicitly given by the ion density arriving at the sample surface. It is assumed that the dielectric function ϵ_r is space and concentration independent. Eventually, the ion transport is determined calculating Fick's second law:

$$\frac{\partial}{\partial t} n_v = - \frac{\partial J_v}{\partial z} \quad (64)$$

According to the numerical procedure used for the theoretical model, the ions are deposited at the frontside of the sample and enter either the bulk of a grain or a grain boundary. In the calculations, it is assumed that 80 % of the incoming ions enter a grain boundary. The ion population gives rise to an electric field which needs to be calculated. Therefore, equation 63 is linearized and iteratively solved until the electric potential corresponds to the charge carrier distribution inside the sample. Then the ion flux is calculated according to equation 62 and charge carriers are shifted inside the material according to equation 64. Eventually, the modified charge carrier distribution influences the electric potential which needs to be adjusted such that the procedure starts again. Thanks to the theoretical model described above, a fit of the experimental data, i.e. of the potassium concentration profile of figure 39, with numerical data have been performed. The result of this analysis is shown in figure 47 below.

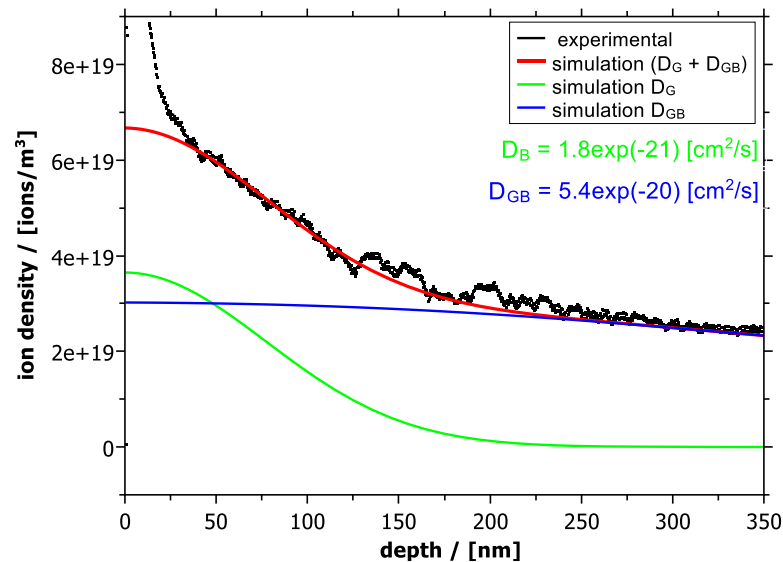


Fig. 47: Ion density vs depth from experimental data (black), simulated mixed pathway diffusion (red), simulated sole bulk diffusion (green) and simulated sole grain boundary diffusion (blue).

In Figure 47 the red line is the sum up of the two contributions, which are shown as blue (simulated sole grain boundary diffusion) and green dots (simulated sole bulk diffusion). The two coefficients associated with the corresponding pathways are presented as well. The highest value of D is associated with the diffusion along the grain boundaries since is usually faster than the bulk diffusion, as already mentioned previously [155]. A good fit is achieved using diffusion coefficients of $D_B = 1.8 \times 10^{-21} \text{ cm}^2 \text{ s}^{-1}$ and $D_{BG} = 5.4 \times 10^{-20} \text{ cm}^2 \text{ s}^{-1}$ for bulk and grain boundary diffusion, respectively.

5.2 Polyelectrolyte multilayers results and discussion

As already described in section 4.2.1 (“Substrates and polyelectrolyte multilayers preparation”), different types of substrates for the preparation of the PEMs have been used within the research of this study. The type of substrate has been adjusted to the special requirements of the sample preparation procedure and the desired CAIT and ToF-SIMS measurements. In the following sections, the results of the experiments conducted using the different substrates will be presented, together with a discussion of the data. A multi-level analysis will show:

- CAIT analysis on the Design I, whose resulting data turned out to be dominated by the influence of the specific substrate used, i.e. the glass D263T (see section 4.2.1 for details on the Design I);
- qualitative comparisons of ToF-SIMS depth profiles of (PAH/calix8)₁₅ bombarded with a potassium homogeneous ion beam for different bombarding time (in section 5.2.2 Design II and 5.2.3 III);
- qualitative and quantitative studies on the transport of Li⁺, K⁺ and Rb⁺ through (PAH/calix8)₃₀ (abbreviated as M⁺@(PAH/calix8)₃₀ with M⁺ = Li⁺, K⁺ and Rb⁺). This final level of analysis will provide a theoretical model and based on the Nernst–Planck–Poisson theory, that yields a quantitative understanding of the transport process of M⁺ through a calix8-based membrane (in section 5.2.4 Design IV).

5.2.1 Design I : glass/Cr/Au/PEMs system

As already anticipated in the first point of the section 5.2, in this section the results of this study will be discussed with the aim to give the reader an example of how meaningful could be the choice of a suitable construction design for performing experimental analysis of membranes such as polyelectrolyte multilayers. The original purpose of this study was indeed the investigation of the conductance of (PAH/calix8)_n with the variation of the number of bilayers. However, from results of the temperature dependence of the conductance, a value of activation energy E_{act} has been derived which turned out to be not consistent with the expected one on the basis of previous literature data. In particular, all the data lent support to the conclusion that the glass resistance, instead of the resistance of the PEMs, has been measured during the experiments.

Conductance measurements and activation energy

In this section details about the experiments conducted, as well as the discussion of the conductance measurements will be presented. For clarity reasons in all the plots shown, the caption under the figures will report the wording “under the influence of the substrate”. At the end of the section, a relevant discussion on how it was possible to trace the experimental data back to the influence of the glass-substrate system will be presented. The CAIT experimental setup previously illustrated (section 3.1) and a home-made potassium ion emitter of *type a* (section 4.1.1) were used for the conductance measurements. The backside current is investigated as a function of the initial ion kinetic energy, i.e. the applied repeller voltage, U_{rp} . Films of $(PAH/calix8)_n$ with different numbers of bilayers n (n from 1 to 30) in a temperature range of temperature of $70\text{ }^\circ\text{C} - 80\text{ }^\circ\text{C}$ were investigated. The ion current has been detected at the backside electrode as a function of the repeller voltage which was varied from 2 V to 10 V, in steps of 1 V. The ion current arriving at the sample position has been detected in a reference experiment where the sample was replaced by a copper plate. The reference current was chosen ≥ 1 nA during the entire experiment, sufficiently large to guarantee that the surface potential reaches the repeller potential everywhere, thus ensuring a homogeneous surface potential. Figure 48 shows the result of current–voltage characteristic for $(PAH/calix8)_{30}$ at different $T(^{\circ}\text{C})$ from $70\text{ }^\circ\text{C}$ to $80\text{ }^\circ\text{C}$ in steps of $2\text{ }^\circ\text{C}$.

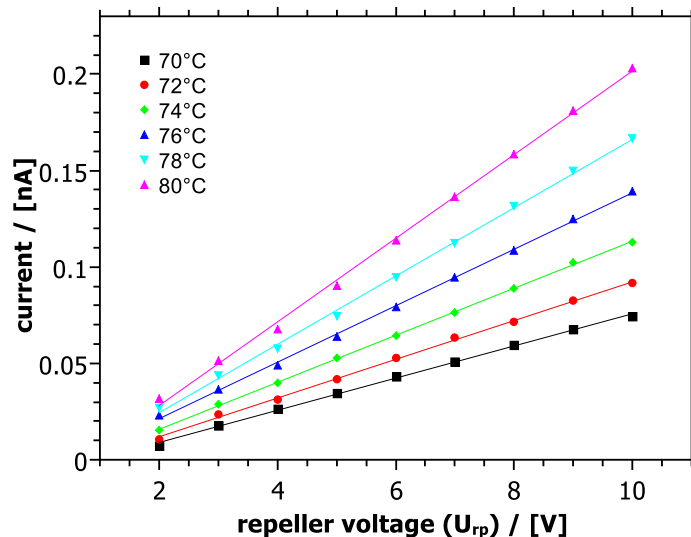


Fig. 48: Current-voltage characteristic of a $(PAH/calix8)_{30}$ under the influence of the substrate.

Conduction characteristic obeying Ohm's law is observed for each curve. The conductance G for each temperature can be determined directly from the slope of the current–voltage curves using the equation (43):

$$G = \frac{\Delta I_{det}}{\Delta U_{rp}} \quad (43)$$

It is observed that the conductance increases with increasing temperature, in particular: raising the temperature by 2 °C from 70 °C to 72 °C, correlates with increasing the conductance by a factor of 20 percent from 8.34×10^{-12} S to 1.01×10^{-11} S. The temperature dependence of the ionic conductance is depicted in figure 49 where $\ln(GT)$ is plotted as a function of the inverse temperature.

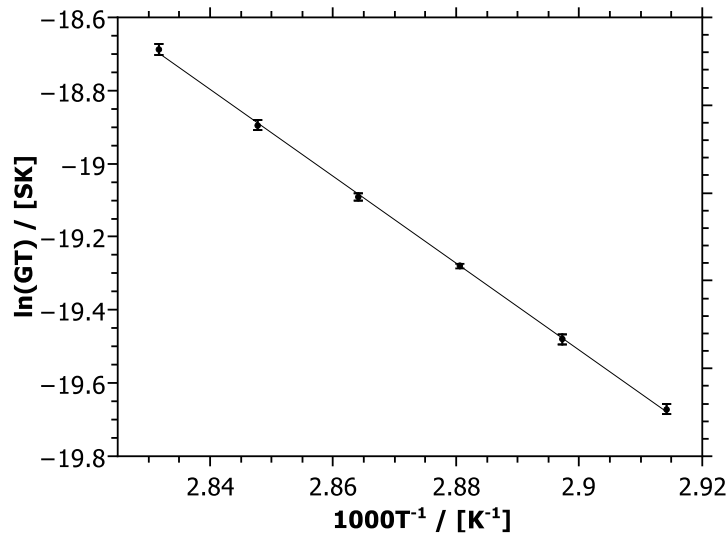


Fig. 49: Temperature dependence of the ionic conductance for (PAH/calix8)₃₀ under the influence of the substrate. A value of activation energy of $1.025 \text{ eV} \pm 0.04 \text{ eV}$ has been calculated from the slope.

The value of E_{act} has been derived from the slope of the linear regression of figure 49, according to the eq. (61) in section 5.1, leading to a value of $E_{act} = 1.03 \text{ eV} \pm 0.04 \text{ eV}$.

In order to determine the conductance of (PAH/calix8)_n as a function of the number of bilayers, samples with $n = 1, 3, 6, 9, 12, 15, 20, 30$ bilayers have been bombarded with a spatially homogeneous potassium ion beam using voltages between 2

V and 10 V and a temperature range from 70 °C to 80 °C (see Appendix B for relevant current-voltage characteristic curves). In figures 50 summary plots of the measurements are shown:

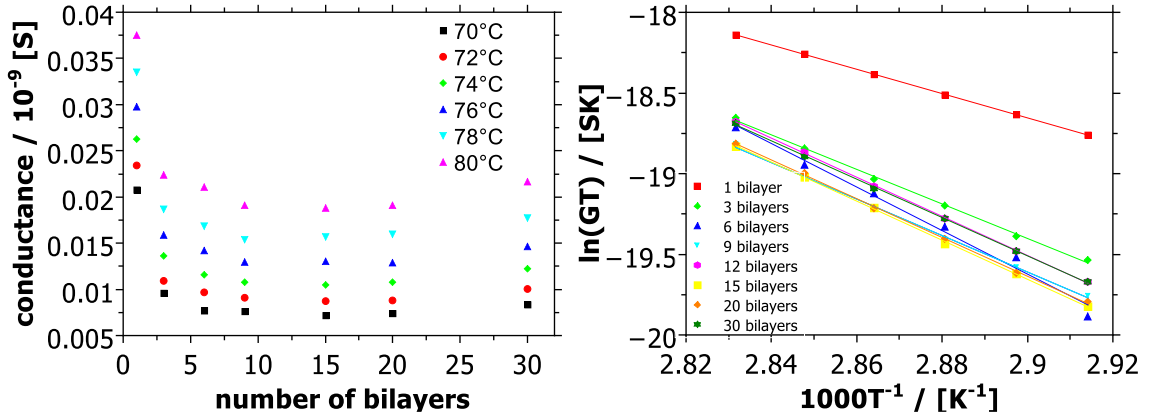


Fig. 50: Representation of the conductance G vs. the number of bilayers (left) and temperature dependence of the conductance (right) under the influence of the substrate.

The calculated activation energies are summarized in figure 51:

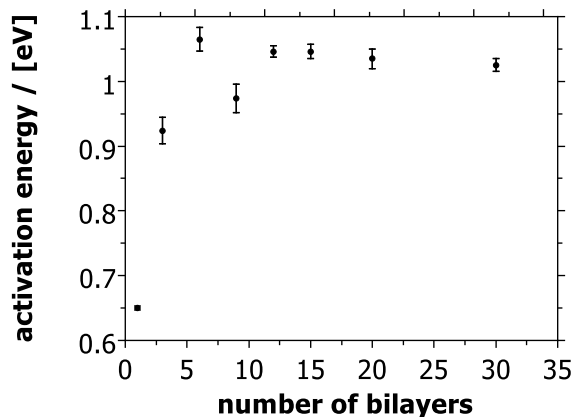


Fig. 51: E_{act} of $(PAH/calix8)_n$ with $n = 1, 3, 6, 9, 12, 15, 20, 30$ under the influence of the substrate.

The conductance values shown in figure 50 barely vary from 3 to 30 bilayers, only for 1 bilayer a higher value can be seen. This observable does not seem to be in agreement with the CAIT theory described in section 3.1, according to which the conductance should scale inversely with the thickness of the sample, how is e.g. observed for ion conducting glasses [2, 120]. In the frame of the CAIT theory indeed, a purely ohmic conductor with

homogenous charge carrier density and homogenous diffusion coefficient would exhibit a neutralization current according to the relation (equation 35, section 2.3.3):

$$G = \frac{I_{det}}{U_{rp}} = \frac{U_{rp} \cdot Z^2 \cdot e^2 \cdot A \cdot D \cdot n}{L \cdot k_B \cdot T} \quad (35)$$

where Z is the charge of the ion, e is the elementary charge, A is the bombarded area, D is the temperature dependent diffusion constant, n the number density of the charge carriers inside the film, L is the thickness of the PEM multilayer (which depends on the number of bilayer n), k_B is the Boltzmann constant and T the temperature.

In a recent work of Wesp *et al.* [7], the dependence of the ionic conductance of (PAH/PSS)_x films on the number of bilayers has been investigated by means of the CAIT method. In their work, it has been found a variation of the detected neutralization current with the repeller voltage similar to the variation adapted from the PEMs under analysis in the work of this thesis, i.e. an ohmic behavior has been seen, where the current scales linearly with the acceleration voltage of the ion beam. Despite this similarity, in their work Wesp *et al.* found that the conductance of (PAH/PSS)_x multilayers system (with $x = 1, 2, 4, 6, 8, 10, 12, 14, 16, 18$ bilayers) varies with the number of bilayers, contrary to the result of the study of this thesis (displayed in figure 50). In particular, Wesp *et al.* found that the conductance of their film varies non-monotonically with the number of bilayers. Between 2 and 8 bilayers, the conductance is observed to increase exponentially with the number of bilayers, showing a maximum for $x = 8$. For more than 8 bilayers, the conductance decreases with a $1/x$ function in agreement with equation (35). On the contrary, As already pointed out, the conductance for (PAH/calix8)_n does not vary with the number of bilayers from 3 to 30 bilayers. The only observable which is in common between the two studies is the experimental conductance for the single bilayer, which is found to be higher than the predicted one in both systems. As an explanation, they claim that the conductance of the single bilayer may well be strongly influenced by the close neighborhood to the substrate and most likely the structural characteristic of the single bilayer differs from the multilayers.

In order to better understand why the trend of the conductance for (PAH/calix8)_n with the number of bilayers does not follow the theoretical description (equation 35), a further discussion seems to be appropriate. Subsequently, a series of ideas as possible explanations will be considered. According to the literature, PEM films may show a variation in their fundamental conduction behavior when a certain number of bilayers is overcome. Wesp et al., for instance, found a fundamental change in the conduction behavior between 6 and 8 bilayers. In general, in literature, there have been different attempts to explain the change of properties for a certain number of bilayers and most of them account for a non-homogeneous growth of the multilayers. In section 2.1 of this thesis, two models were presented, i.e. the *Ladam Model* and the *Capillary Membrane Model (CMM)*. From the one hand, Ladam *et al.* introduced a three-zone model, where an approximately 6 bilayers thick zone I is determined by the vicinity of the substrate. There, the substrate influences the PEM properties. Zone II represents the bulk of the sample while the sample in zone III is influenced by the solution environment. From the other hand, the capillary membrane model, introduced by Silva *et al.*, assumes that the coverage of the layers is not complete at the early stage of the multilayer growth process. Uncovered spots remain through which the transport is favored. The more layers are added, the less important the spots become. Beyond about 10 layers, the membranes behave like a homogeneous material. Besides these two models, it is known that the growth of PEM multilayers occurs non-homogeneously, i.e. the first layers are thinner than the layers deposited consecutively [156, 157, 158, 159]. Thus, from a conceptual point of view, the trend of the conductance for (PAH/calix8)_n membranes with the number of bilayers could be traced back to structural changes of the membrane which occur during the growth process of the film. Although this last point may represent a possible explanation, however, it seems to be unrealistic that a variation in the inner structure of the film with the number of bilayers is able to compensate any variation in the measured conductance, such that the latter is observed to maintain a constant trend over a range 3 to 30 bilayers. To put it another way, the trend of the conductance for (PAH/calix8)_n with the number of bilayers cannot be understood from the physical justification of the variation of properties within the growth process of the PEMs. If this is the case, then a different idea which could explain the results of figure 50, is required: under the assumption that the system investigated could have been influenced from external conditions, a more detailed analysis on the design and the construction of the sample

appears to be appropriate. It is to remember that in the Design I (glass/Cr/Au/PEMs) the sputtered chromium layer acts as coverage in order to isolate the glass support to the rest of the system, while the gold layer is needed for the growth of the PEMs. Before mounting the so constructed sample, i.e. glass/Cr/Au/PEMs, onto the copper electrode, the back and lateral sides of the Au/PEMs coverage were removed by means of sandpaper, in order to avoid any contact between the polymeric film lying on top of the substrate and the copper plate below (see section 4.2.1 “Substrates and polyelectrolyte multilayers preparation” for graphical illustration). Under the hypothesis that the treatment with the sandpaper scratched away the lateral chromium coverage as well, then the entire system would have acted as if it was made by two resistances in series, as illustrated in figure 52 below:

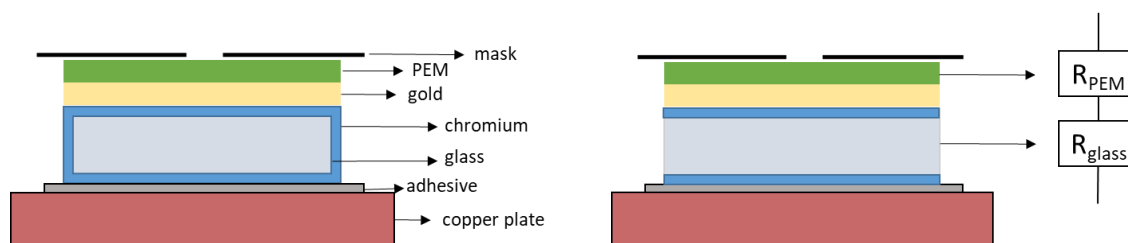


Fig. 52: Illustration of the construction Design I in the case of a desired final system (left) and an undesired scratching of the lateral coverage of chromium (right).

In favor of such idea, it is worth noting that the values of activation energies shown in figure 51 are very similar to the one reported from the literature [160] of 0.98 eV for the technical D263T glass. The latter is indeed the same type of glass used as support substrate in the experiments conducted within this thesis. Under this evidence, it seems as if the glass resistance instead of the resistance of the sample has been measured during the experiments. In conclusion, it is clear from these considerations that the design I was not the most suitable one in order to investigate the conductance of such membranes, hence a different kind of approach has been chosen and a new substrate design has taken into account.

5.2.2 Design II : steel/Au/PEMs system

The design II involves the use of steel instead of glass as support substrate. The pictures below show the gold layer right after the sputter coating process (figure 53-a) and after the functionalization with PEMs (figure 53-b). The last picture instead shows the same sample but subjected to a peeling off phenomenon (figure 53-c), which occurred at room temperature and ambient pressure in a timescale of few days.

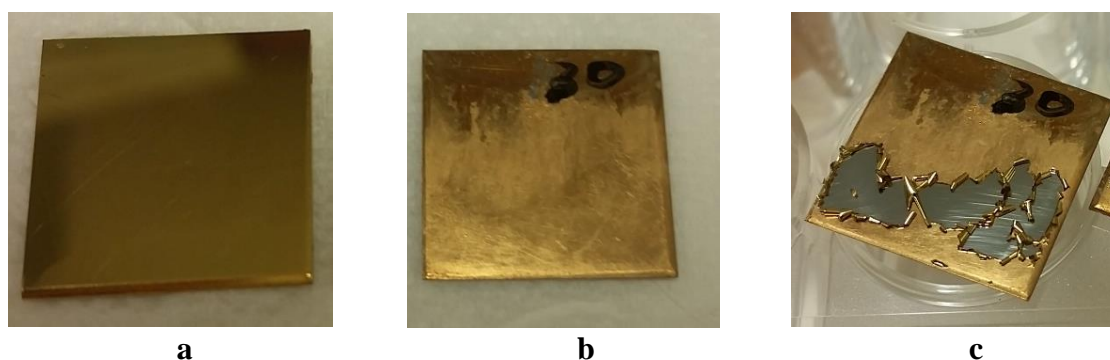


Fig. 53: Top view of a fresh gold-sputtered steel substrate (a), a PEM-functionalized sample (b) and the same sample after some days into storage (c).

A possible explanation to this phenomenon could rely on the fact that the sputtered gold layer did not stick onto the steel firmly. For that, a slightly different design of the substrates has been thought, where a 20 nm thick chromium layer has been sputtered in between steel and gold layer. Due to the better adhesive capacity of the chromium on steel and of the gold on chromium, the new substrates resulted to be permanently stable. The results of the experiments conducted on these new samples are shown in the next section.

5.2.3 Design III : steel/Cr/Au/PEMs system

Ion conductance studies by means of the CAIT technique have been conducted as first experiment. Figure 54 shows the result of current–voltage characteristic for PAH/calix8 with 9 bilayers from 70 °C to 100 °C.

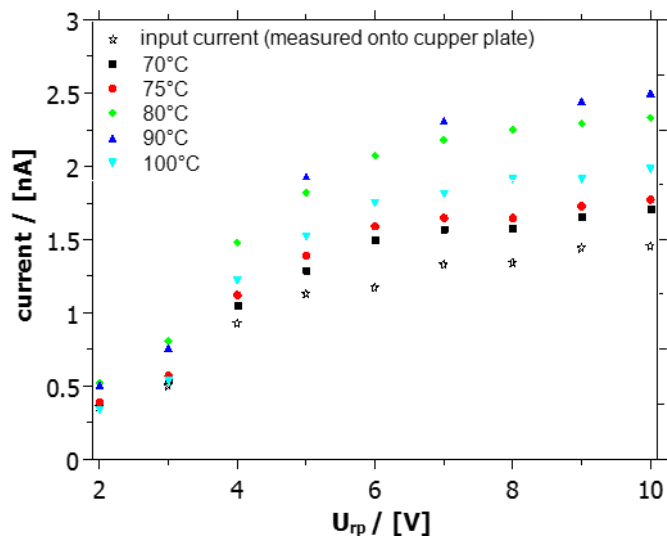


Fig. 54: Current–voltage characteristic for (PAH/calix8)₉ at a temperature range from 70 °C to 100 °C. Black stars rely on the input current measured in the same range of voltages.

In The plot of figure 54 the black empty stars show the current measured on a copper plate in order to detect the input current which arrives at the sample surface position. The full symbols in figure 54 show instead the result of another measurement where the copper plate has been replaced with a (PAH/calix8)₉ sample and current-voltage curves for different temperatures of the sample have been registered. It is worth noting that for both measurements (with the copper plate and with the real sample) the heating current chosen in order to heat the emitter till a certain temperature was the same, i.e. 5800 mA. From the comparison between the measurement of the input current and the measurement for the sample, it is clear that all the impinging ions arriving at the surface of the real sample are detected at the back of the membrane. A similar current indeed has been detected in both measurements. To be precise the current measured in the input experiment has a slightly lower intensity. This does not surprise since the two measurements were not conducted consecutively, but the entire system has been shut down in order to replace the copper plate with the (PAH/calix8)₉ sample. It is very often observed indeed that between different CAIT experiments, even using the same heating current for the emitter and the same set of voltages for the lenses, the input current could slightly vary. Another observable of figure 54 is that the current-voltage curves for different sample temperature show no correlation between the measured backside current with the variation of the temperature. The observables described up to now led to the conclusion that the sample

does not seem to show any resistance. In order to confirm that all the impinging ions arriving at the surface of the real sample are detected at the backside, the measure shown in figure 54 conducted at 100 °C has been repeated increasing the emitter temperature by raising the heating current for the ion beam from 5800 mA to 6200 mA. The result of this experiment is presented in figure 55.

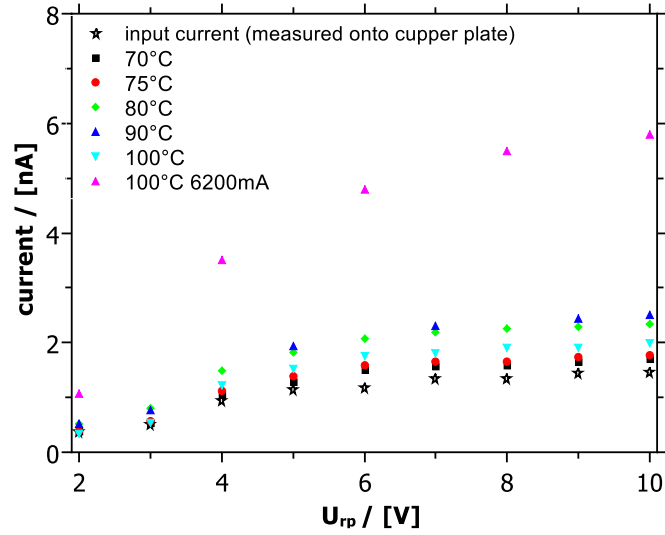


Fig. 55: Current–voltage characteristic for (PAH/calix8)₉ in a temperature range from 70 °C to 100 °C. Pink triangles rely on the measured backside corresponding to an ion beam with heating current of 6200 mA instead of 5800 mA.

As a result of this measurement (see pink triangles in figure 55), the increase in the input current is reflected in the change of the detected backside current. All these observables bring to the conclusion that the surface potential of the sample remained well below the repeller voltage applied, implying a very high sample conductivity. Turning back to the theory illustrated in section 2.3.3, this means that:

$$J_{blind} < J_{sample}^{max} \quad \text{and} \quad \phi_{surf} < U_{rp} \quad (28)$$

which corresponds to the case a) described in the theoretical section 2.3.3.

In several publications DC conductivities of PEMs have been reported ranging from $10^{-12} \text{ Scm}^{-1}$ to 10^{-5} Scm^{-1} [161, 162, 163, 164]. Studies of the conductivities of PEM started with the work of Durstock and Rubner [161]: they investigated films of PSS/PAH or PAA/PAH, respectively, where PAA denotes poly(acrylic acid), PSS is

poly(styrene sulfonate sodium salt), and PAH is poly(allylamine hydrochloride). They found DC conductivities, σ_{dc} , in the range of $10^{-12} \text{ Scm}^{-1}$ to 10^{-7} Scm^{-1} , where the maximum of 10^{-7} Scm^{-1} was achieved only at strong hydration. Further studies of conductivities in polyelectrolyte multilayers suggested the PEMs as potential ion conductive materials for battery applications [162, 163]: employing poly(2-acrylamido-2-methyl-1-propanesulfonic acid) (PAMPS) as a polyanion, at high humidity a value of the DC conductivity of $\sigma_{dc} \approx 10^{-5} \text{ Scm}^{-1}$ was achieved, which is already in a realistic range for applications. Different polyelectrolyte pairs tested for their conductivity already involved polymers known as ion conductors, such as: Nafion as an established proton conductor [162], poly(ethylene oxide) (PEO) as a classical polymer electrolyte [163], or polyphosphazenes as polymer electrolytes [164, 165]. A major problem in the interpretation of conductivity is the lack of knowledge about the composition of the films. It is well known indeed that PEMs are materials of unknown stoichiometry. In a study of the 2008 Argun *et al.* reported the highest ionic conductivity ever obtained from a layer-by-layer assembled thin film, i.e. $3.5 \times 10^{-2} \text{ S cm}^{-1}$ at 98% relative humidity and 25 °C. This value is of three orders of magnitude higher than the one reported in the best conducting system up to this point and it is already of the same order of magnitude as commercially relevant membranes such as Nafion. However, it is true that the PEMs prepared within this the study of this thesis should be free from water, and for that their conductivity should not be influenced by the humidity content. It must be remembered indeed, that one of the preparation steps of the was drying the film with inert nitrogen after each absorption step.

It is known from the literature that the PEMs layer thickness can be tuned in the nm to μm range and that a low film thickness yields low overall resistance and fast loading. In order to gain info regarding the thickness of the $(\text{PAH/calix8})_n$ films, ellipsometry measurements have been conducted. Samples with number of bilayers $n = 3, 6, 9, 12, 15, 20$ and 30 were analyzed by the AG Biophotonic at the Center for Hybrid Nanostructures of the University of Hamburg. The result is plotted in figure 56:

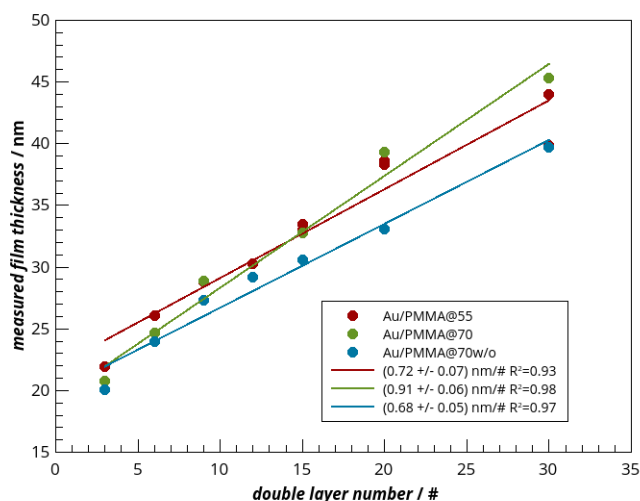


Fig. 56: Ellipsometry measurements conducted onto $(\text{PAH/calix8})_n$ with $n = 3, 6, 9, 12, 15, 20$ and 30 (*original raw data from the analysis conducted in Hamburg).

The figure 56 shows values of thickness relatively low if compared with the one reported from Caruso *et al.* [156] of 9.7 nm per bilayer, based onto a $(\text{PAH/PSS})_n$ system built under similar conditions. However, in the context of polyelectrolyte multilayers prepared by layer-by-layer technique, external parameters such as salt concentration [35], pH value [166] or temperature [167] provide control of the layer thickness. In a work of the 2010 [168] Ashcraft *et al.* studied layer-by-layer films composed of poly(diallyl dimethyl ammonium chloride) (PDAC) and sulfonated poly(2,6-dimethyl 1,4-phenylene oxide) (sPPO), i.e. $(\text{PDAC/sPPO})_n$, as a result of the variation of the ionic strength of the assembly solutions. They found that the film growth is modulated from 6.91 nm/bilayer when assembled with no salt, to 62.2 nm/bilayer when assembled with 0.5 M salt.

All the data presented lend support to the conclusion that it was not possible to determine the conductivity as well as activation energy values for $(\text{PAH/calix8})_n$ system. This is why from now the focus of the discussion is to try to understand the ion transport via the analysis of depth profiles. In order to do that, the transport of macroscopic amounts of potassium ions through $(\text{PAH/calix8})_{15}$ membrane is discussed in this section from a qualitative point of view. Ultimately, the transport of potassium through the PEMs gives rise to concentration profiles characteristic of diffusion, which can be determined by means of time-of-flight secondary ion mass spectrometry (ToF-SIMS). For that, two

samples of (PAH/calix8)₁₅ have been bombarded with a homogeneous potassium ion beam, using different bombarding time, leading to the incorporation of different amount of charge within the PEMs film. In the case of 1-hour bombardment (1-hB) the charge incorporated was $Q = 6.6 \mu\text{C}$, while the case of 300-s bombardment (300-sB) led to an incorporated charge of $Q = 0.64 \mu\text{C}$. A comparison of the corresponding concentration profiles is presented subsequently.

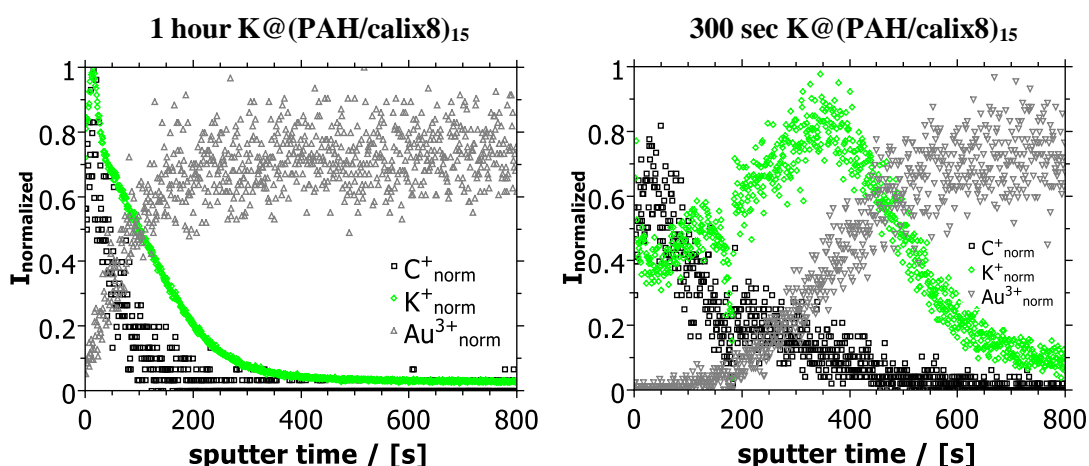


Fig. 57: Concentration profiles of the bombarded (PAH/calix8)₁₅. The ion signals are normalized to the maximum ion signal of the corresponding species. Left: depth profile for 1-hour long-time bombardment. Right: depth profile for 300-sec long-time bombardment.

As the original order of the layers upon preparation was PEMs onto Au, this order is also reflected in the concentration profiles: here the carbon signal is taken as the indicator of the polymer film and the gold signal reflects the backside electrode. For standardization of the intensity data obtained by ToF-SIMS analysis, a normalization procedure was performed. The x-axis displays the sputter time originating from the raw data. A transformation of the x-scale into a depth one was not possible in this case, due to the limitation of the profilometer instrument. The Sloan Dektak3ST indeed is not suitable to work with soft surfaces, else the integrity of the surface itself would be compromised. The two concentration profiles of figure 57 differ from multiple points of view.

One result of this analysis regards the profile of the carbon signal associated with the PEM. It is notable how the carbon signal extends along with different sputter time ranges: from 200 in case 1-hB, till 600 sputter second for 300-sB. Parallel to this observation, the

gold signal rises already at the beginning of the measurement in the 1-hB case. Such trend reflects a different sputter rate associated with the sputtering process of the polymeric film, i.e. in the case of 300-sB the sputter rate is higher. Granted that the conditions under which all the measurements have been acquired are the same (Cs^+ sputter beam, with ion current between 18 nA - 30 nA), the reason of a difference in the sputter rate can come from the inner structure of the film. In order to verify this supposition a ToF-SIMS analysis onto a not-bombarded $(\text{PAH/calix8})_{15}$ was taken and the result is shown below:

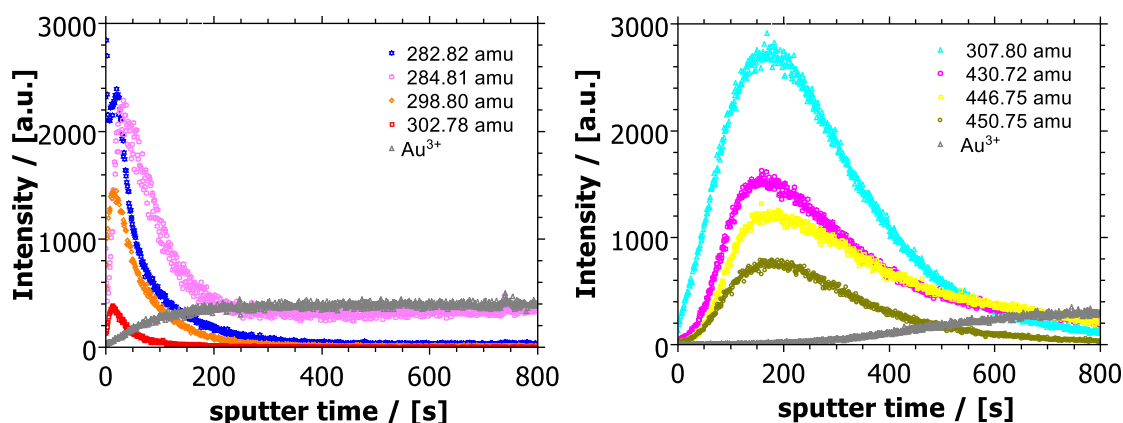


Fig. 58: Depth profiles of position B (left) and position C (right) taken from a fresh sample of $(\text{PAH/calix8})_{15}$. In both cases, fragments of the film were taken as reference for the PEM layer.

Two trends seem to be present. In the left plot of figure 58, the signals associated with fragments of the PEMs (see index in the plot) present high intensity since the first seconds of analysis, while they drop down to low intensity within the first 200 sputter seconds. This trend appears to be similar to the one already described for the plot on the left of figure 57. The second trend which comes out of figure 58 is the one visible on the right plot. Here the signals (see index in the plot) extend across the first 600 sputter seconds likewise the case of the carbon signal in the right plot of figure 57. Provided that the two profiles of figure 58 belong to the same samples, it might be said that the film is not homogeneously distributed onto the surface. There are rather regions where either the growth of the PEMs did not proceed linearly, or the rinsing protocol did not occur properly, such that different spots on the surface appear more swollen than others. In figure 59 a picture of the analyzed reference $(\text{PAH/calix8})_{15}$ reveals visible heterogeneity of the film.

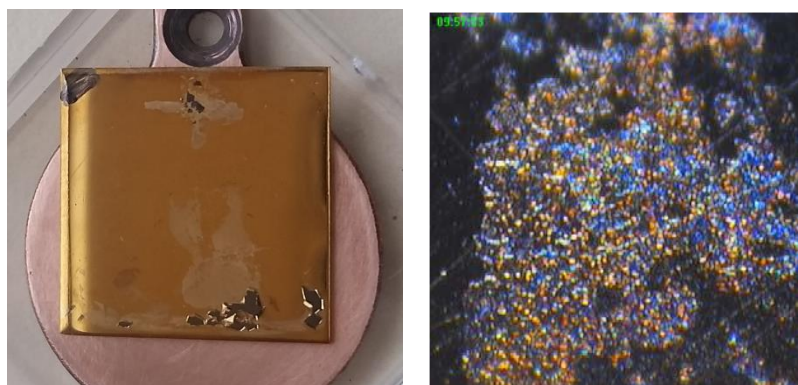


Fig. 59: (PAH/calix8)₁₅ picture with visible inhomogenous spots (left); picture taken by a ToF-SIMS camera showing the same inhomogeneity in microscale (right).

Another result of figure 57 comes from the comparison of the potassium depth profiles in both plots. The two concentration profiles indeed do not seem to have the same trend. In the right plot of figure 57, the potassium signal follows the same tendency of the carbon. In this case, most likely a charge incorporated of $Q = 6.6 \mu\text{C}$ led to a complete filling up of the membrane. In the case of 300-sB the charge incorporated was lower, i.e. $Q = 0.64 \mu\text{C}$. By looking at the right plot of figure 57, it is clear how the potassium signal does not follow the carbon, but rather assumes a trend which could be rationalized as due to the diffusion of potassium ions through the membrane and to the accumulation of the neutralized potassium at the interface between membrane and gold electrode.

5.2.4 Design IV : steel/Au-foil/PEMs system

As already described in section 4.2.1 the Design IV differs from the Design I, II and III in the gold layer, which is no more a sputter-coated coverage, but rather a massive gold foil. Since their preparation the films of (PAH/calix8)₃₀ remained stable: the samples did not change form nor color, despite the fact that the preparation and then the storage of the membranes took place at room temperature and ambient pressure. The reason for that is mainly due to the choice of the building components such as PAH as cationic polyelectrolyte from one side and calix8 as anionic counterpart from the other side. PAH is known to be used as model system in studies of multilayers stability [169, 170], while calix8 seems to be more suited for adsorption rather than the parent calix4 or calix6, i.e.

p-sulfonato-calix[4]arene and p-sulfonato-calix[6]arene, respectively. The calix8 has indeed a higher number of ionic binding sites and the adsorption/desorption equilibrium is determined from the number of binding sites per ring (eight sulfonates group for the calix8). Moreover, the ring conformation of the three mentioned calixarenes is different and calix8 attains mainly the flat-plane conformation, being well suited for adsorption [171]. In table 8 some peaks from the mass spectra obtained by means of a ToF-SIMS analysis onto a (PAH/calix8)₃₀ are listed. The peaks are associated with fragments of the polymeric compounds used to prepare the PEMs:

Table 8: Main fragments taken as reference of the PEMs. Nominal mass, experimental mass at which the peak has been found and the location of origin of the fragment are listed in table.

<i>fragment association</i>	<i>nominal mass m/z</i>	<i>experimental mass m/z</i>	<i>location</i>
NH ₃ ⁺	17.026 amu	17.027 amu	PAH
NH ₄ ⁺	18.034 amu	18.037 amu	PAH
S ⁺	31.972 amu	31.968 amu	calix8
CH ₃ NH ₃ ⁺	32.050 amu	32.048 amu	PAH
SO ₃ ⁺	79.957 amu	80.060 amu	calix8
HSCH ₂ CH ₂ CO ₂ H (MPA) ⁺	106.009 amu	106.075 amu	MPA
(1/8 calix8) ⁺	188.014 amu	188.057 amu	calix8

Subsequently, ion transport studies of Li⁺, K⁺ and Rb⁺ through (PAH/calix8)₃₀ will be presented. Li⁺ and Rb⁺ were chosen because a ToF-SIMS analysis on a reference fresh (PAH/calix8)₃₀ revealed the absence of both Li⁺ and Rb⁺ ions within the PEMs, ensuring that the post evaluation of the data will not be somehow compromised from the original conditions of the sample. The same is not completely true for the K⁺ ions, which were found to be present into the PEMs already prior to the bombardment. The source of this contamination was actually the same gold layer used as substrate. A ToF-SIMS analysis conducted onto the gold foil showed indeed the presence of K⁺ within the gold. Neither Li⁺ nor Rb⁺ ions were found within the gold layer (see appendix C1 for relevant depth profile). However, results concerning the K⁺-bombardment will be presented here with the only aim to give a qualitative comparison in the series Li⁺, K⁺, Rb⁺ but a quantitative evaluation of the data for the K⁺ case was not conducted.

The experimental set up used has been already illustrated in section 4.1. For the emission of potassium and rubidium, aluminosilicates of composition $M[\text{AlSi}_2\text{O}_6]$ ($M = \text{K}, \text{Rb}$) has been used together with an emitter *type a* (see section 4.1.1), while synthetic spodumene ($\text{LiAlSi}_2\text{O}_6$) has been chosen as the material for the Li^+ ion emission together with a filament type emitter. In all cases, the ion current reaching the sample surface has been set to a value lower than 1nA , between 0.3 nA and 0.7 nA depending on the specific emitter. For each ion beam (Li^+ , K^+ , Rb^+) two kind of experiments have been performed, varying the time for the bombardment: 5 seconds in one case (5-secB) and 100 seconds in the other (100-secB), whereas the repeller voltage used for the ion beam was 5 V and the temperature of the sample 80°C in both experiments. In figure 60 below depth profiles as result of these experiments are shown:

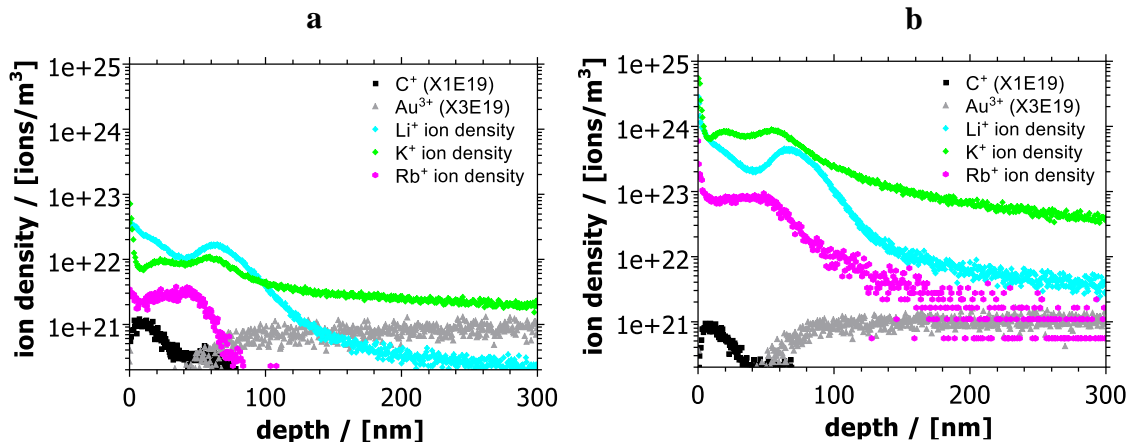


Fig. 60: Plots of ion densities vs depth for $[\text{Li}^+, \text{K}^+, \text{Rb}^+]@(\text{PAH}/\text{calix8})_{30}$ after bombarding time of 5 seconds (a) and 100 seconds (b).

In order to convert the sputter time from the raw data into a physical depth axis, it is assumed that the thickness of the $(\text{PAH}/\text{calix8})_{30}$ film is 40 nm , which accords to the value measured by ellipsometry (see figure 55). The carbon signal has been chosen as representative for the film. The decay of the carbon signal and the onset of the Au^{3+} signal, that represents the gold backside electrode, have been identified as the end of the film. As a consequence, the point on the x-axis where the gold signal and the carbon signal intersect has been set to 40 nm . The entire normalization of the x-axis has then been derived assuming a constant sputter rate over the entire range of sputter seconds. In the plots of figure 60 the raw original intensity in arbitrary units (a.u.) has been transformed

into an ion density by taking into account the integral under the intensities curves of each ion signal, the charge accumulated after each bombardment (calculated from the current time characteristic curves), and the dimension of the bombarded area:

$$ion\ density = \frac{I}{\int Idx} \frac{Q(C)}{A e} \quad (65)$$

where I is the raw intensity in a.u., Q stands for the charge accumulated in Coulomb, A is the bombarded area in square meter and e is the elemental charge of the electron. It must be highlighted that the diffusion profiles for Li^+ , K^+ , and Rb^+ are plotted in the same graph for comparison reasons, but they are related to different measurements and hence different amount of incorporated charge. As representative for the film and the backside electrode, the C^+ and Au^{3+} signals from the profile generated by the Li^+ -bombardment are shown. The corresponding profiles from the K^+ and Rb^+ -bombardment are very similar in size and shape such that this simplification does not imply a crucial approximation. A comparison between the depth profiles of Li^+ , K^+ , and Rb^+ of figure 60-**a** and the ones of figure 60-**b** shows that the intensity level of the curves from **(a)** to **(b)** increases. This observable appears to be consistent with higher values for the charge accumulated after the bombardment (see table 9).

Table 9: charge accumulated for [Li^+ , K^+ , Rb^+]@($PAH/calix8$)₃₀ after bombarding time of 5 seconds and 100 seconds.

<i>alkali ion</i>	<i>charge accumulated</i>	
	<i>5 sec experiment</i>	<i>100 sec experiment</i>
Li^+	3.08 nC	79.82 nC
K^+	2.17 nC	163.00 nC
Rb^+	0.35 nC	12.67 nC

A comparison of the depth profiles within the same graph, either within figure 60-**a** or within figure 60-**b**, shows that only the Li^+ signal presents a space dependent concentration profile, whereas the other two alkali signals show no diffusion profile in the same depth range but an almost constant tendency. In first approximation, the Li^+ signal shows an exponential decay with increasing space, where its intensity drops exponentially from the very beginning of the membrane layer to the end of the film at 40

nm. Such profiles can typically be found if diffusion processes are relevant. Another aspect is the maximum at circa 70 nm exhibited from the Li^+ signal. This maximum can be associated with an accumulation of lithium ions which were neutralized and thus accumulate at the interface between film and gold substrate. Such an accumulation is not visible in the case of the Rb^+ curve, whereas the K^+ signal shows a hint of accumulation at the gold interface. However, for the K^+ case, the complication of any argument would be the contamination of the original gold substrate with potassium. It is not known indeed which fraction of K^+ comes from the gold and which has been introduced from the bombardment. For this reason, the transport mechanism of K^+ through the film will not be further discussed, whereas in the next sections simulations and a theoretical model will be presented, in order to better describe the ion transport of Li^+ and Rb^+ ions through $(\text{PAH}/\text{calix8})_{30}$ film.

Numerical analysis of 5-secB Li^+ @ $(\text{PAH}/\text{calix8})_{30}$ and 5-secB Rb^+ @ $(\text{PAH}/\text{calix8})_{30}$

In this section, a detailed analysis of the lithium concentration profile for 5 seconds long bombardment is presented. In Figure 61 a comparison between experimental and theoretical data is shown.

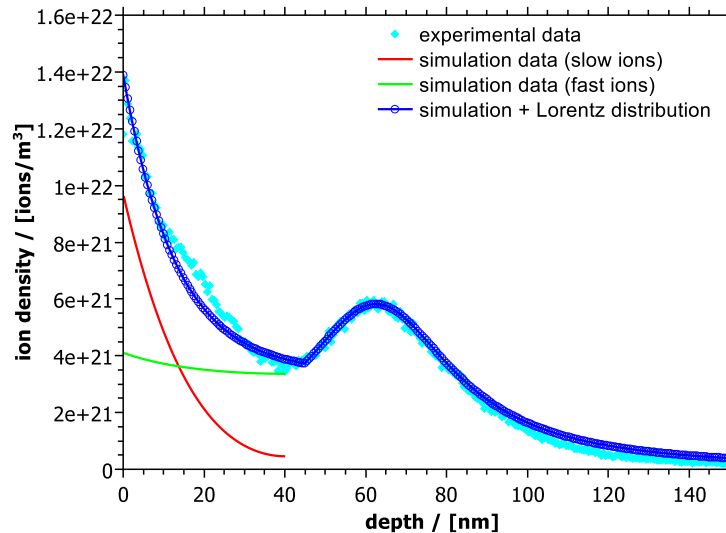


Fig. 61: Ion density versus depth of experimental data (light blue), simulated slow pathway diffusion (red) and fast pathway one (green) together with total contribution (blue).

As already anticipated in section 2.3.3, calculations of the simulated curves have been performed by solving the coupled set of NPP-equations. In each time step the potential is calculated self-consistently to the carrier distributions. For the calculations, the z-axis is discretized into space elements Δz . The space grid used for the simulations shown in figure 61 has been chosen with space increments of $\Delta z = 0.04$ nm and number of increments $z = 100$. While the time grid has been set to $\Delta t = 5 \times 10^{-5}$ s and number of time increments $t = 100.000$. As material constant, the dielectric function associated to the PEMs was $\epsilon_r = 10$. The plot of figure 61 shows two regions of interest: the first region contains the first 40 nm below the bombarded surface and corresponds to the region where the PEM is present; the second region from 40 nm to 150 nm shows a local maximum of the Li^+ signal. As possible explanation one may think to a process where ions enter from the front side, then two possible diffusion pathways could be operative inside the membrane, one accounting for slow lithium ions diffusion and the other one for fast lithium ions diffusion. Eventually, the ions reaching the gold electrode are neutralized and they accumulate at the interface between membrane and substrate (see the second region of interest in figure 61). Thus, the model used to examine the ion transport across the membrane results in a combination of two diffusion pathways: the diffusion of slow lithium ions (associated with the simulated curve in red in figure 61) and diffusion of fast lithium ions (see green line in figure 61). The total contribution of the two simulated curves (in red and green) is displayed from the first part of the blue dots-line of figure 61. A good fit is achieved using diffusion coefficients of $D_{\text{slow}} = 0.4 \times 10^{-16}$ cm²/s and $D_{\text{fast}} = 1.2 \times 10^{-15}$ cm²/s and assuming that 40% of the incoming ions enter the slow pathway, whereas the rest of the ions is transported via a fast pathway. The second region of interest of figure 61 has been fitted with a Lorentz distribution (see the second part of the blue dots-line). A good agreement between model and experimental data comes from the observation of the amount of charge transported within the film and the amount of charge accumulated beyond it: considering the experimental concentration lithium profile, one is able to calculate the amount of charge transported inside the film (from the integral of the intensity data along the depth) and the amount of lithium deposited at the backside electrode (always from the integral of the intensity data along the depth). The ratio between the two quantities gives an experimental indication of the *charge factor* (*c.f.*) between ions located inside the membrane and lithium accumulated at the interface. In the case of the experimental Li^+ depth profile a *c.f.* = 1.33 has been found. From the

theoretical calculation a value of *charge factor* has been calculated, i.e. $c.f. = 1.59$. This value seems to be in agreement with the one provided from the experimental data, with a deviation of 20% between the two values. An explanation for such deviation comes from the fact that in the reality there is not a net separation between charge inside the film and atoms accumulated and the limit is better described from a smeared boundary region, such that values of experimental *charge factor* can be considered as approximate values. In order to discuss the accuracy of the values of the diffusion coefficient associated with the two pathways, further discussion will be conducted subsequently. The plot shown in figure 62 below displays experimental data (light blue diamond symbols) together with some of the simulation test conducted within the theoretical studies.

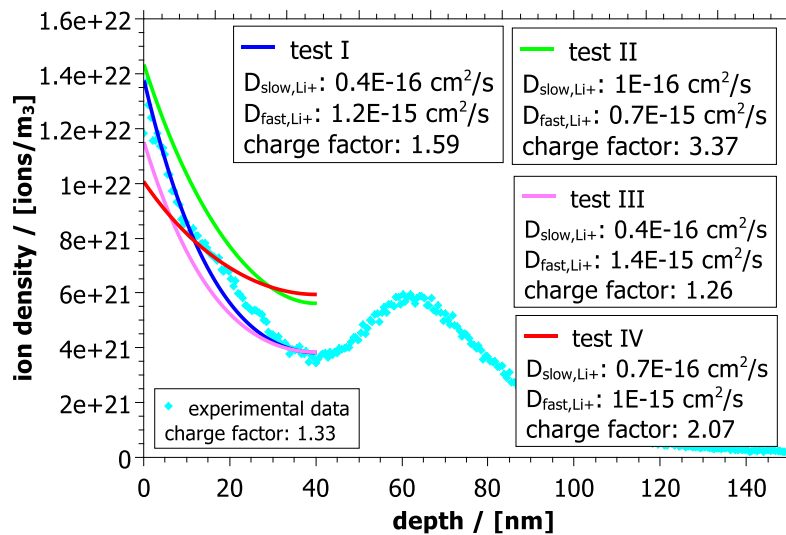


Fig. 62: Ion density versus depth of experimental data (light blue) and simulated curves from different calculation test. More details regarding the appendix are given in the text.

The test have been named test I, II, III and IV for simplicity reasons. The curves of figure 62 are the sum up of simulated slow and fast pathway curves. The blue line under the name test I refers to the already discussed curve of figure 61 and it was reported again here in order to provide a comparison between different simulated curves. Each curve is associated with an appendix box where are listed all the meaningful parameters which led to the simulated curve, i.e. the diffusion coefficients for fast and slow ions and the theoretical *charge factor* (calculated in the way already described). An accurate look at the curves and at the relative set of parameters shows how the test I seems to provide the

better match. In particular a comparison between test I and test III (pink curve) reveals how a variation from $D_{\text{fast, Li}^+} = 1.2 \times 10^{-15} \text{ cm}^2/\text{s}$ to $D_{\text{fast, Li}^+} = 1.4 \times 10^{-15} \text{ cm}^2/\text{s}$ leads to a worsening of the match between calculated and experimental data, although the test III could be considered better with respect to the agreement between experimental and theoretical *charge factor*. Finding the best set of parameters in order to achieve the best match is not always straightforward and the plot of figure 62 only shows some of the test conducted within this study. Although, it is clear that even a small variation in one of the parameters could bring to a deviation from the best fitting.

Turning back to the outcome of figure 61, a discussion of the data together with some literature reference will be presented here below. Ion transport across PEMs containing calixarenes has been investigated by Toutianoush *et al.* [14] where p-sulfonato-calix[n]arene / poly(vinilamine) (PVA) multilayers were used as model system for studies of permeation rates of various electrolytes in aqueous solution; the author verified that the permeation of monovalent alkali-metal chlorides (Li, Na, K, Cs) across the calixarene/polyelectrolyte multilayer films is retarded compared with the all-PEM membranes, i.e. membranes without ring units from calixarenes. They claim that in addition to the Donnan effect (which refers to the rejection of permeating cations at the positively charged parts of the film) [172], the presence of the calixarenes units may influence the type of transport. The cyclic arrangement induces indeed a highly negative charge density at the ring units, which can attract the cations depending on their size and charge density. In the frame of the model used in the work of this thesis, two pathways are taken into account one being slower than the other, leading to a diffusion profile as a combination of the two. The presence of the ring units may play a role not indifferent in defining the kind of transport across the (PAH/calix8)₃₀. Part of the lithium ions (according to the numerical calculation 40%) are retarded on their transport, due to the interaction with the negative pendant groups of the calixarenes, while the rest of the ions pass through the membrane via hopping transport between discrete sites [173]. In order to shed further light on the mechanism of transport suggested from this theoretical model, numerical simulation for the rubidium diffusion profile has been conducted as well. In figure 63 the simulated data, as well as the experimental concentration profile, is plotted over the depth:

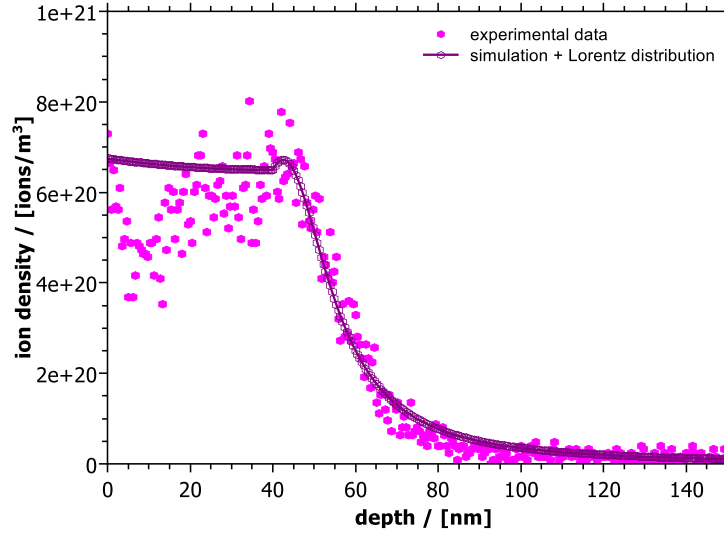


Fig. 63: Ion density versus depth. Experimental data (pink dots) and numerical data (simulated till 40nm plus Lorentz distribution) are plotted.

The space grid used for the simulations shown in figure 63 has been chosen with space increments of $\Delta z = 0.04$ nm and number of increments $z = 100$. While the time grid has been set to $\Delta t = 5 \times 10^{-6}$ s and number of time increments $t = 1.000.000$. The main difference from the lithium case is the trend of the rubidium diffusion profile across the film: an almost flat curve is found to be characteristic of the transport. The numerical calculation reveals that actually, only the fast diffusion pathway is relevant for the transport of rubidium. The plot displays a simulated curve which is actually a sum up of two contributions, slow diffusion and fast one, where the latter one is predominant. From the results of the model, only the 0.01% of the rubidium ions enter the slow pathway, whereas the rest is dominated from the faster one. The value of the diffusion coefficient associated with this fast pathway is of $D_{\text{fast}} = 7 \times 10^{-15} (\pm 1.5 \times 10^{-15})$ cm²/s. Even in this case the comparison between experimental *charge factor* and theoretical one brings to a good agreement ($c.f.\text{exp} = 1.55$ and $c.f.\text{theo} = 1.54$). It is noticeable that the D_{fast} for the rubidium is higher than the one found for the lithium ($D_{\text{fast,Li}^+} = 1.2 \times 10^{-15}$ cm²/s vs $D_{\text{fast,Rb}^+} = 7 \times 10^{-15} (\pm 1.5 \times 10^{-15})$ cm²/s), leading to the suggestion that the rubidium ions are less influenced, i.e. attracted, from the negative calixarene units. In the previous section, fast pathway was indeed associated with the polar properties of the membrane and the slow pathway with the influence of the calixarenes. If this is the case, then the rubidium ions are not only less (or even none) attracted from the negative rings, but the

hopping mechanism which controls the fast pathway seems to be enhanced in the case of the rubidium with respect to the lithium ions. This remark appears to be consistent with the results of the study conducted by Toutianoush *et al.*, where the permeation rate values of alkali-metal chlorides across calix8/PVA films increase in the series from LiCl to CsCl. According to their explanation, the higher size of the rubidium cations (0.148 nm versus 0.068 nm) and its consequent lower charge density, seems to have a crucial role on the electrostatic rejection of the ions from the equally charged parts of the membrane. To return to an earlier point, i.e. the lack of accumulation beyond the membrane in the case of the rubidium ions, the model would suggest that the dominating fast pathway makes the ions be trapped homogeneously across the film by means of the polymer-bound exchange sites, as described from the hopping mechanism. Contrary to this case, lithium ions are distributed with 40% to the slow pathway and 60% to the fast one, giving rise to a diffusion profile which reflects the combination of the two and not the predominance of one.

Finally, a discussion regarding the accuracy of the value of diffusion coefficient associated with the fast rubidium ions is presented subsequently. In figure 64 below a plot similar to the one displayed in figure 63 is shown:

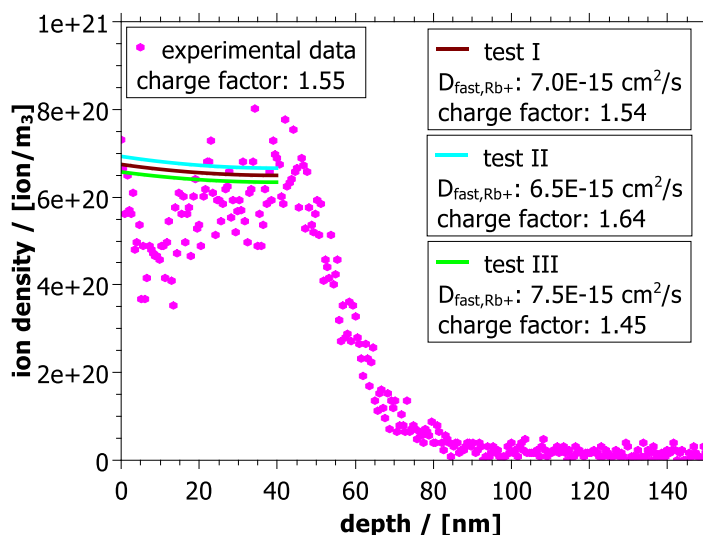


Fig. 64: Ion density versus depth of experimental data (magenta symbols) and simulated curves from different calculation test. More details regarding the appendix are given in the text.

The plot shown in figure 64 displays experimental data (magenta symbols) together with some of the simulation test conducted within this study. As already described for the figure 63, also the curves of figure 64 refer to the fast ions diffusion pathway, being indeed this the predominant one in the case of the rubidium ions. The test I of figure 64 refers to the simulation curve of figure 63 already discussed. Differently from figure 62 for the lithium ions case, the accuracy of the diffusion coefficient seems to be more easily derived here. A comparison between test I, II and III shows indeed how a variation of $\pm 7\%$ in the value chosen for the fast diffusion coefficient (from $D_{\text{fast}} = 7 \times 10^{-15}$ to $D_{\text{fast}} = 6.5 \times 10^{-15}$ in test II and to $D_{\text{fast}} = 7.5 \times 10^{-15}$ in test III) brings to a respective variation of the *charge factor*, whereas the profile of the simulated curves does not vary significantly. This is way it seems to be reasonable to conclude with a final value for the transport of fast rubidium ions of $D_{\text{fast}} = 7 \times 10^{-15} (\pm 1.5 \times 10^{-15}) \text{ cm}^2/\text{s}$.

5.3 Measurements of offsets in CAIT detection process

In a typical CAIT experiment, the surface of the sample is electrically charged after bombardment with thermionic emitted particles (ions and in principle also electrons). In analogy to a DC-transport experiment, the charged surface induces transport such that the resistance of the sample can be detected. The registered current leads then to the determination of values of DC conductivity from the slope m of the recorded current-voltage characteristic, according to the equation (36) and (37). However, a deep analysis of this kind of I_{back} vs U_{rp} curves, shows that they are not lines with $I_{\text{back}} = 0$ for $U_{\text{rp}} = 0$, but physically the current-voltage data have finite offsets on the order of few Volt (see schematic graph in figure 65).

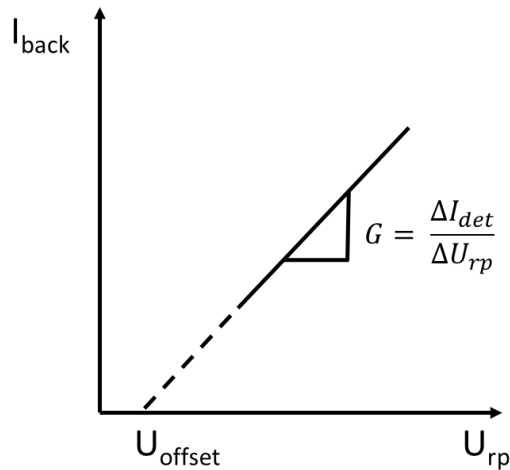


Fig 65: Schematic graph of a generic I_{back} vs U_{rp} curve. The intercept with the x-axis represents the offset voltage.

This offset is the analogue to offsets observed in classical thermionic electron emission from a metal detected by some other metal plate. In a classical experiment, electrons are generated by thermionic emission from a metal 1 and the current is detected by a metal 2. In this basic experiment, it is observed that the current-voltage graph exhibits an offset, which originates from the difference in the electronic work functions of metals 1 and 2, i.e., the classical quantification of the Volta effect [174, 175].

Within the research of this thesis, the focus was so far given to the slope of the current-voltage data, i.e. the conductance, which is not affected by these offsets.

However, this last study aims to give a better understanding of the process beyond the measured voltage offset. In order to do that, a basic CAIT experiment has been performed, where a metal plate has been bombarded with an ion beam from a potassium emitter of the composition KAlSi_2O_6 : Mo (1: 9). The basic setup looks very similar to the one used by Schuld *et al.* in [176] where it was investigated the thermionic emission of Li^+ ions from synthetic spodumene ($\text{LiAlSi}_2\text{O}_6$) as a function of temperature and electric field. One of the outcomes of that work was that the thermionic current exhibits a voltage offset of 1.760 eV. This offset was related to the energy balance required from the Li^+ ions to recombine on the detector plate. The goal of this study is to shed further light on the offset topic. From one hand, a theoretical model based onto the combination of required energy quantities will be taken into account, from the other hand, a comparison with the theoretical model developed from Schuld *et al.* will be discussed. In the following sections experimental data set (5.3.1 section), evaluation of the ionic and electronic work functions (5.3.2 section), as well as a theoretical description of the detection process (5.3.3 section) will be presented.

5.3.1 Current-voltage curves

The set up used for the detection of the current-voltage curves is represented in figure 66 (top), while figure 66 (bottom) shows pictures of the same setup with the meaningful components pointed out via red arrows.

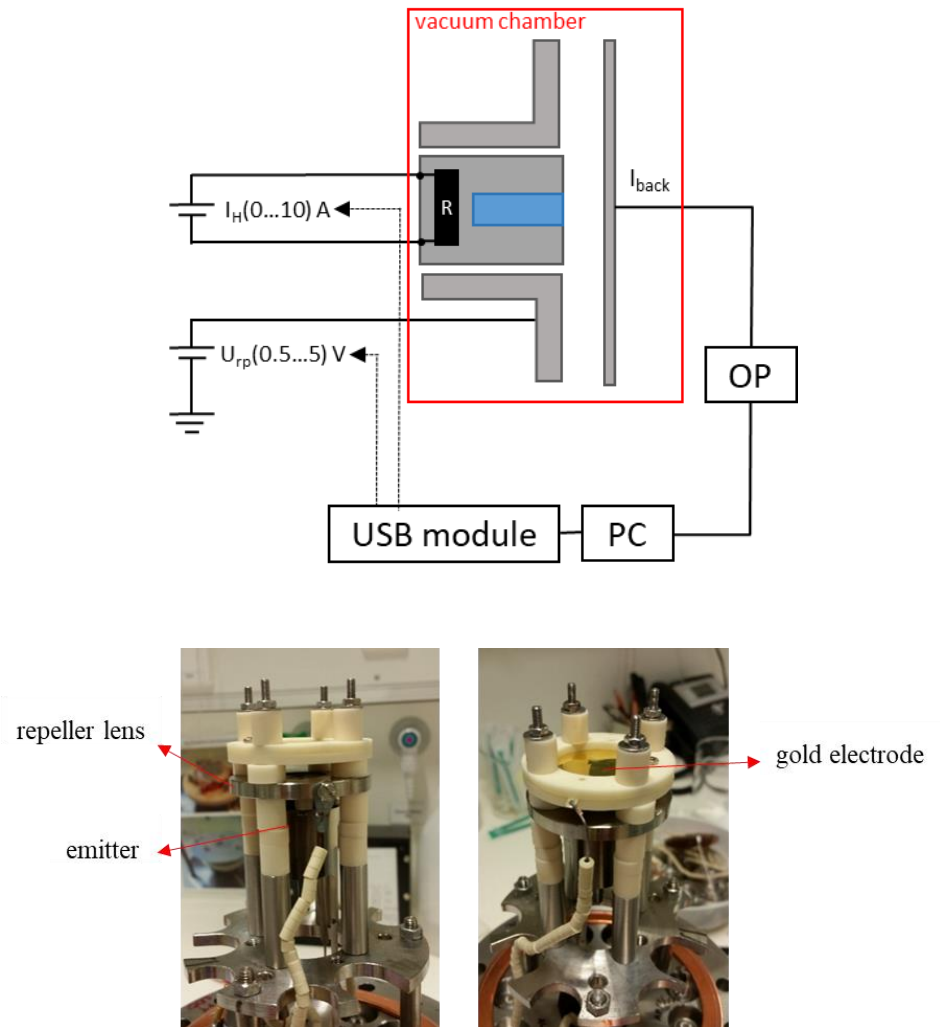


Fig. 66: Sketch of the experimental setup for measuring thermionic ion currents. The upper graph shows the electrical circuit. The bottom graph shows pictures of the set up.

The ion beam source shined directly towards the surface of the metal electrode. As emitter, a home-made potassium emitter of the composition $\text{KAlSi}_2\text{O}_6:\text{Mo}$ (1: 9) has been used. The metal electrode consisted of a gold foil (purity: 99.99%; producer: HMW Hauner). The ions were repelled by a positive potential, U_{rp} , applied to a repeller lens. Ions reaching the surface of the electrode were then neutralized and gave rise to

neutralization current that was detected. An electrometer amplifier has been used to measure the ionic current (see section 4.1 for further details regarding the electronics). It is worth noting that neither an ion optic, nor a blind current measurement system, nor a temperature measurement system for the sample was present. The setup has been maintained on purpose as simple as possible. It is important to emphasize that the aim of this experiment is the detection of the entire potassium ion current flux, in order to register the neutralization current and to study from that the voltage offset characteristic of the detection process in a typical CAIT experiment. Eventually, the setup was placed in a high vacuum chamber and all measurements were performed at a pressure value of $10^{-6}/10^{-7}$ mbar. For each experiment the repeller voltage has been varied in a range 0.5 V – 5 V, in steps of 0.2 V. The measurements were repeated several times to test for the reproducibility, taking care each time to use a cleaned gold surface. The heating current for the emission process was chosen to be 5100 mA for each experiment. In figure 67 a comparison plot of the measurements conducted using the gold electrode is shown:

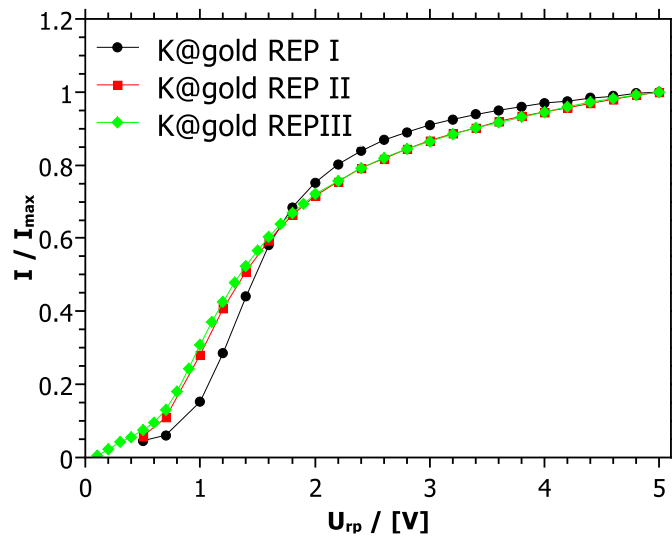


Fig. 67: Normalized ion current vs voltage plots of different measurements. A gold electrode was used as metal detector plate.

The y-axis plots the current normalized to the maximum value, in order to optimize the comparison between different reproduction experiments. The choice of plotting dots-line curves seems to be appropriate in this case, to make the reader comfortable in following the trend of each set of measured points. In order to quantify the voltage offset in a

systematic manner, the part of the curves which showed a linear trend has been fitted via a linear function. From the intercept with the x-axis, a value of offset voltage has been determined. In figure 68 and table 10 below the results of this analysis are listed:

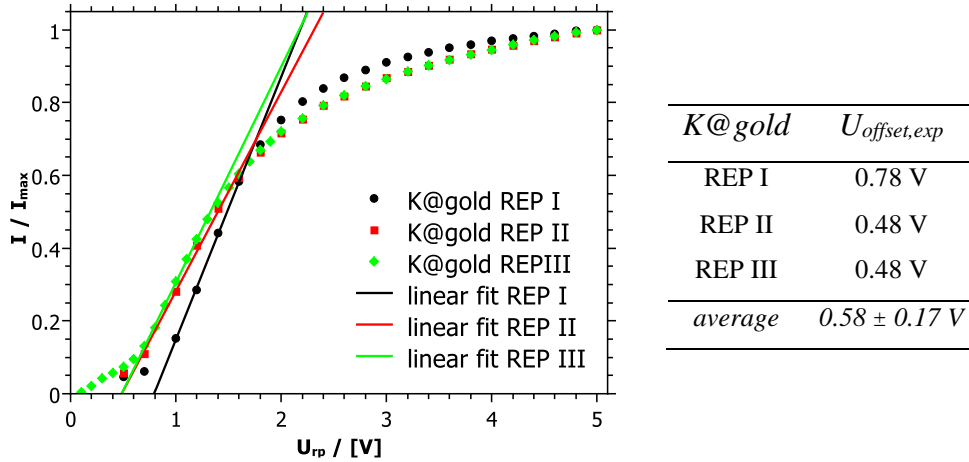


Fig. 68: Evaluation of the experimental U_{offset} from the linear fit of the curves. Listed in table 10 the values for each reproduction measurement as well as the average value of $U_{offset,exp}$.

In order to verify whether the metal electrode could have had a relevant influence in the measured offset, different experiments were performed, where the gold metal electrode was replaced with an electrode made of stainless steel. Reproduction measurements were performed, each time assuring that the surface of the steel was cleaned in advance of the experiment. The results of this analysis are plotted in figure 69.

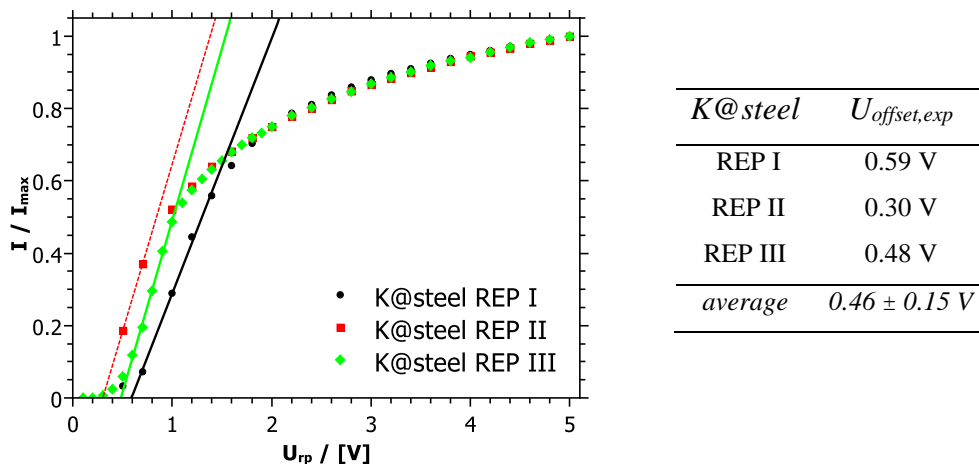


Fig. 69: Normalized ion current vs voltage plots of different measurements. A steel electrode was used as metal detector plate. Listed in table 11 the values for each reproduction measurement as well as the average value of $U_{offset,exp}$.

The plot shows the normalized ion current and the linear fit curves. The values of offset listed in table 11 are close to the ones obtained in the case of the gold electrode. A difference of 0.64eV between the offsets employing the gold and the steel electrode would have been expected if the electrode material contributes to the offset (value of work function for gold and steel is indeed 5.1 eV and 4.46 eV respectively). The measurements performed in this work do not show any indication of such a difference. That is to say: no meaningful influence comes from the type of metal electrode used as detector plate.

If the electrode material does not play a role it should be possible to treat the electrode by shining a K^+ beam in advance. The advantage is that the backside electrode does not change during the experiment. In order to do that, a series of experiments were conducted, where the surface of the gold electrode (and the steel as well) has been previously shined with potassium for a period long enough to lead to the formation of a potassium layer onto the surface. The thickness of such layer has been quantified by means of the following formula:

$$ion\ density = \frac{ions}{thickness\ [m] \cdot area\ [m^2]} \quad (66)$$

Where the ion density value for metal potassium is 1.318×10^{28} ions/m³, while the number of ions has been evaluated according to:

$$ions = \frac{\int I \cdot dt}{e} \quad (67)$$

With I being the intensity of the registered current in Ampere, and e the elementary charge 1.6×10^{-19} C. It must be said that the area was approximated to the lower limit value of 7.07×10^{-6} m², which corresponds to the area of the emitting surface of the emitter. The bombarded area in this kind of experiment is indeed not defined via a mask, however, due to the vicinity of the detector to the emitter, such approximation seems to be reasonable.

The experimental conditions used did not change from the previous ones, i.e. the repeller voltage range used is 0.5 V – 5 V and the heating current 5100 mA.

Below are plotted results of this analysis conducted onto gold and steel electrodes:

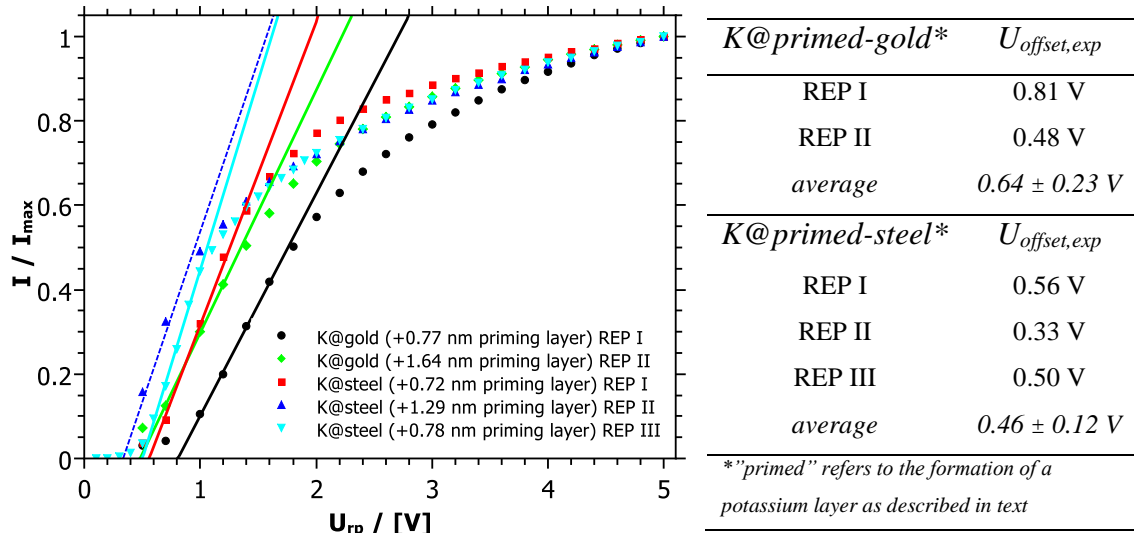


Fig. 70: Normalized ion current vs voltage plots of different measurements after treating the surface of the electrode (both gold and steel data shown). Listed in table 12 the values for each reproduction measurement as well as the average value of $U_{offset,exp}$.

In plot of figure 70 normalized values for y-axes are used. The thickness for the priming layer is displayed on the graph. As result of this analysis, the voltage offset is not influenced by the pre-treatment of the surface. However, the study is limited to the fact that the actual temperature of the electrode is not taken into account. Due to the vicinity of the emitter to the position of the electrode (7 mm distance), the temperature there is very high (order of hundred of Celsius degree). This is a crucial aspect when it comes to the formation of an elemental layer of a substance onto a grounded metal plate. An effect of the high temperature could be, for instance, the melting and / or evaporation of the alkali metal which was deposited on the detector plate. Elemental potassium melts at 62.85 °C, while its vapor pressure at melting point is 1.4×10^{-6} mbar.

The last analysis performed within this study regards the temperature dependence of the measured offset. In figure 71 the registered current vs voltage curves for three different heating currents of the emitter are plotted.

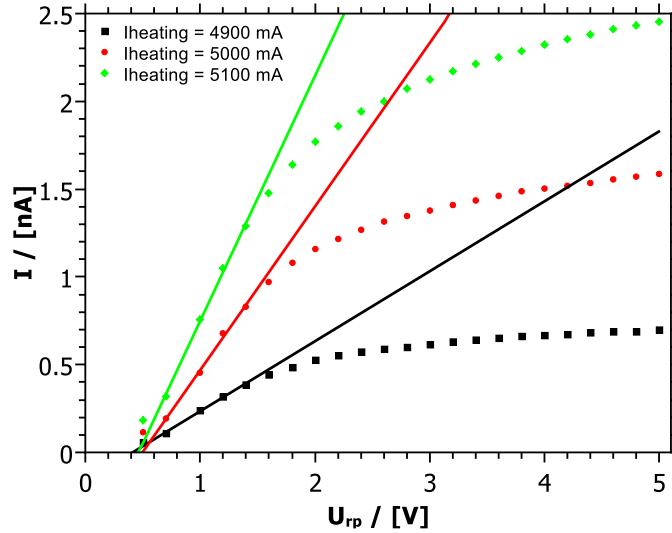


Fig. 71: Ion current vs voltage curves for different heating current. A gold electrode was used as metal detector plate.

As a result of this analysis, it is clear that there is no dependence of the measured voltage offset on the heating current.

5.3.2 Measurements of ionic and electronic work function of a Leucite potassium emitter

As already introduced at the beginning of this section, the detection of K^+ ions by a metal plate implies a balance of the relevant energies, which will show up as an offset in the current-voltage data. In the previous section, a series of experiment have been presented, while in this section the results of ionic and electronic work function measurements will be shown below. When it comes to emitter like a home-made potassium Leucite, it is not given for granted which values of either ionic work function or electronic work function are associated with the specific emitter material. These two contributions appear to be crucial for the energy balance of the detection process investigated (as better elucidated in following section 5.3.3). Provided that, it appeared to be meaningful to perform measurements of ionic and electronic work function for the specific emitter used within

the experiments of this study, i.e. a potassium emitter of the composition $\text{KAlSi}_2\text{O}_6 : \text{Mo}$ (1:9). The investigation of the temperature dependence of the emission current brings to the evaluation of material constants, such as the work function, according to the Richardson-Dushman law:

$$J_0 = A_R T^2 \exp\left\{-\frac{W}{k_B T}\right\} \quad (24)$$

Thus, the temperature dependent ion current has been measured at a constant electric field in front of the emitter (7.14 Vcm^{-1} and -28.57 Vcm^{-1} for ionic and electronic workfunction measurements respectively). Figure 72 shows an example of the trend of the ion current density as a function of the temperature registered in case of a measurement for the evaluation of the ionic work function.

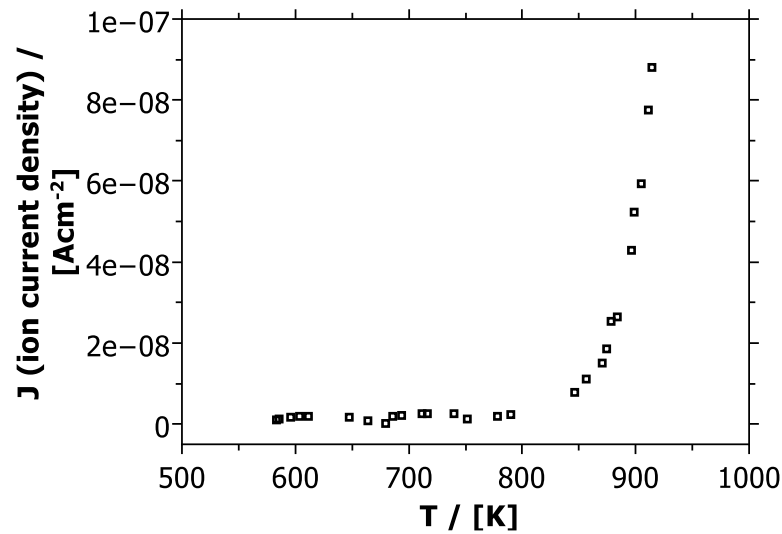


Fig. 72: Representation of the ion current density as a function of the temperature.

It is clear the increase of the ion current density with the temperature. To determine the work function, a plot of $\ln(J/T^2)$ depending on $1/T$ needs to be evaluated. This relationship is shown in figure 72. It results in a straight line whose slope gives the work function $W = \text{slope} \cdot k_B$.

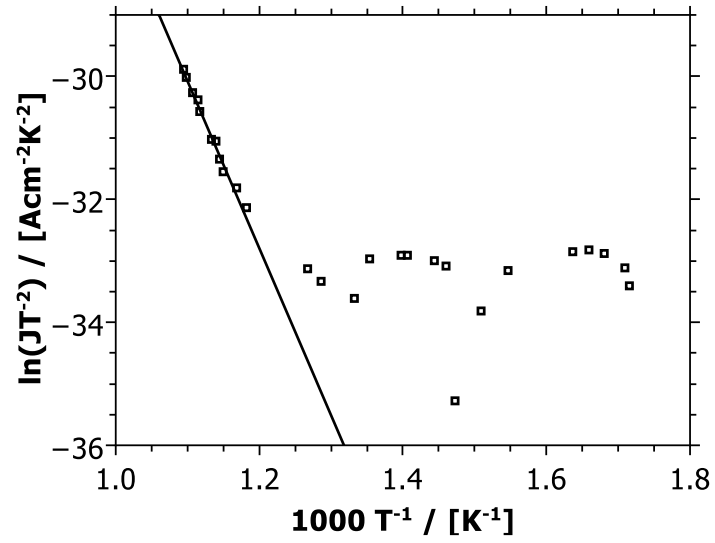


Fig. 73: Evaluation of the ionic work function W_{ion} , from the slope of the linear fit curve.

Multiple reproduction measurements were performed in order to get a mean value of work function. Results of this analysis are summarized below, both for the evaluation of ionic and electronic work function, respectively.

Evaluation of ionic work function according to Richardson-Dushman

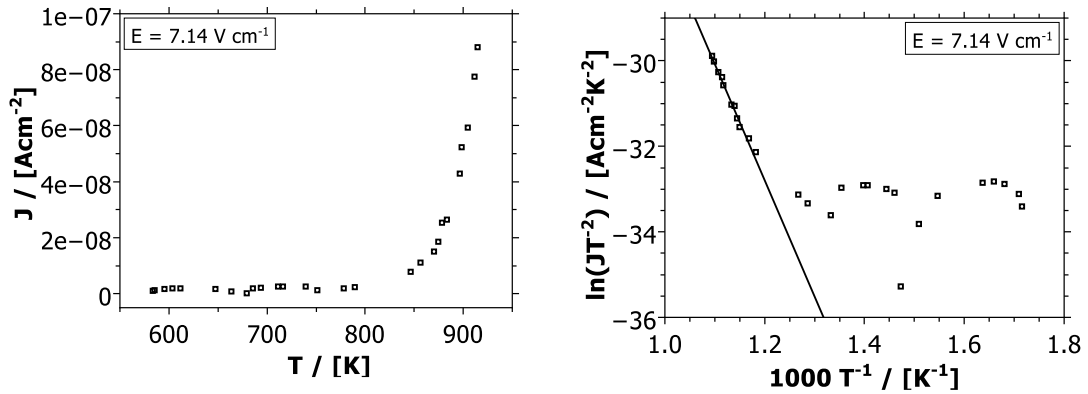


Fig. 74: Evaluation of data for determining the work function according to Richardson-Dushman.
Measurement: REP I (reproduction I).

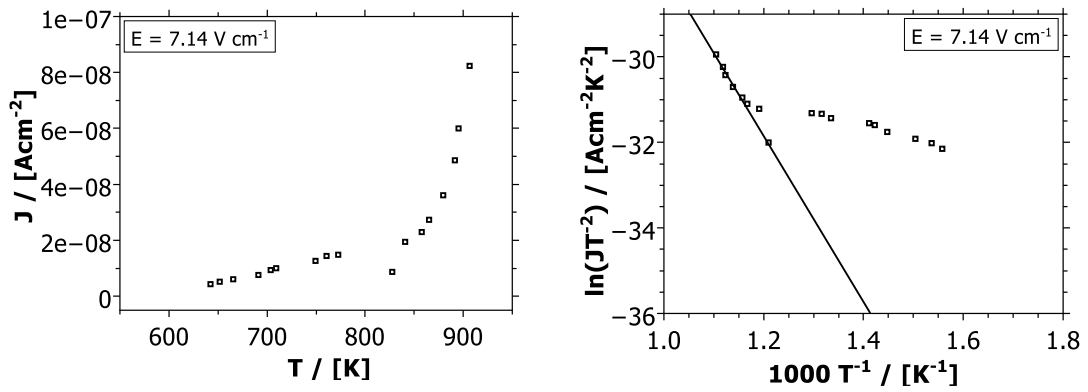


Fig. 75: Evaluation of data for determining the work function according to Richardson-Dushman.
Measurement: REP II (reproduction II).

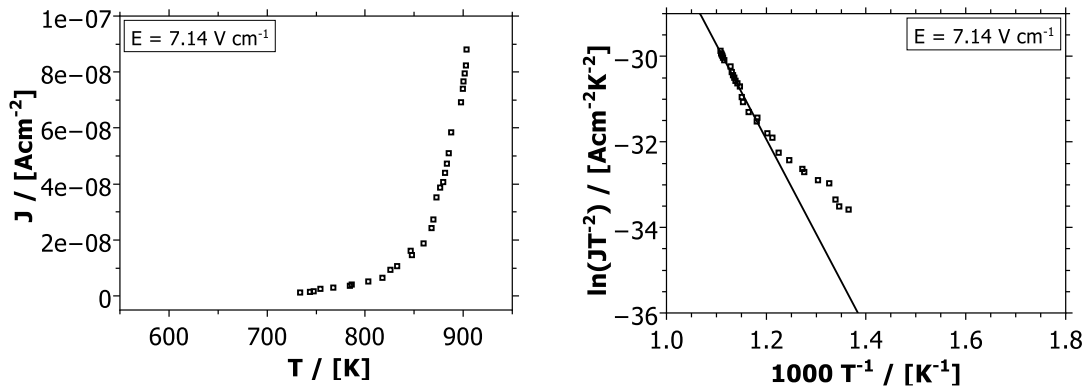


Fig. 76: Evaluation of data for determining the work function according to Richardson-Dushman.
Measurement: REP III (reproduction III)

Table 13: Summary of the results of the linear regressions from the figures 74-76.

<i>measurement</i>	<i>m (slope)</i>	<i>ionic work function</i>	R^2
REP I	-27.18	2.33	0.987
REP II	-19.39	1.64	0.975
REP III	-22.13	1.89	0.982
<i>average value = 1.95 ± 0.35 eV</i>			

Evaluation of electronic work function according to Richardson-Dushman

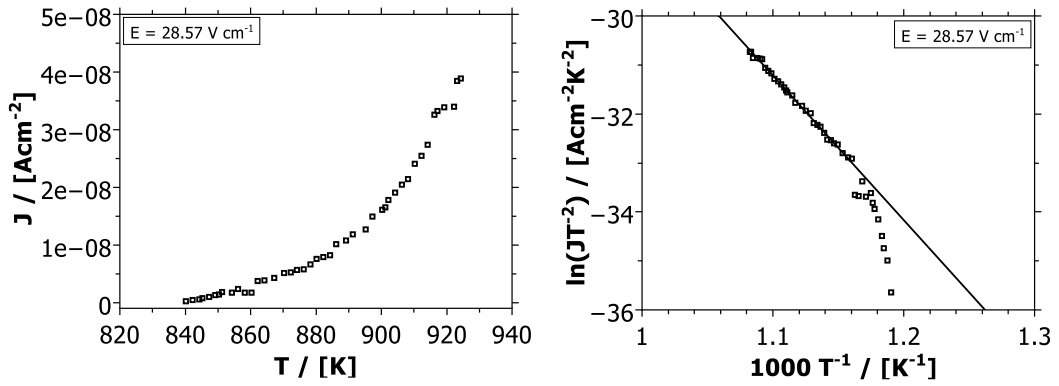


Fig. 77: Evaluation of data for determining the e- work function according to Richardson-Dushman measurement: REP I (reproduction I).

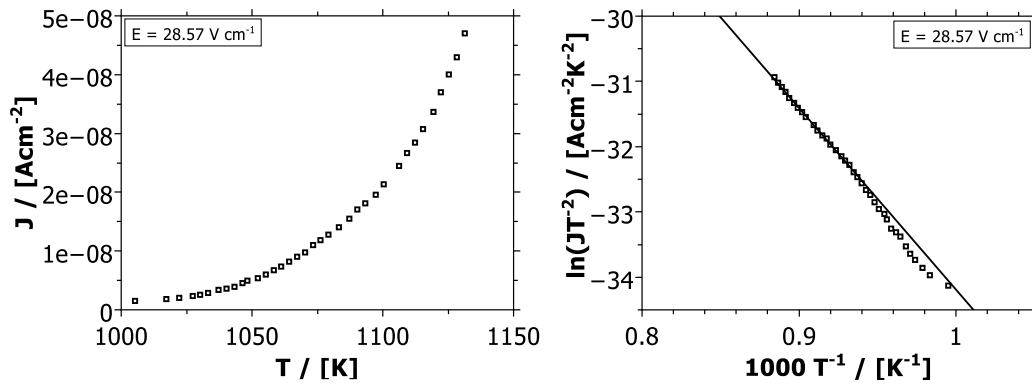


Fig. 78: Evaluation of data for determining the e- work function according to Richardson-Dushman. Measurement: REP II (reproduction II).

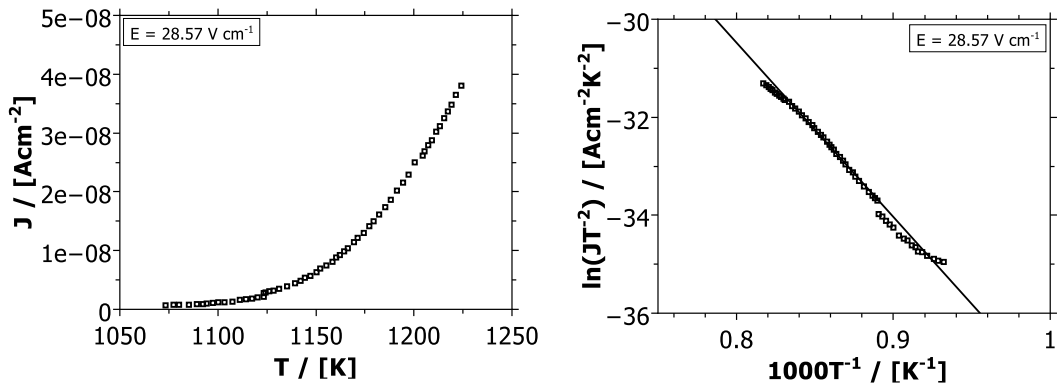


Fig. 79: Evaluation of data for determining the e- work function according to Richardson-Dushman measurement: REP III (reproduction III).

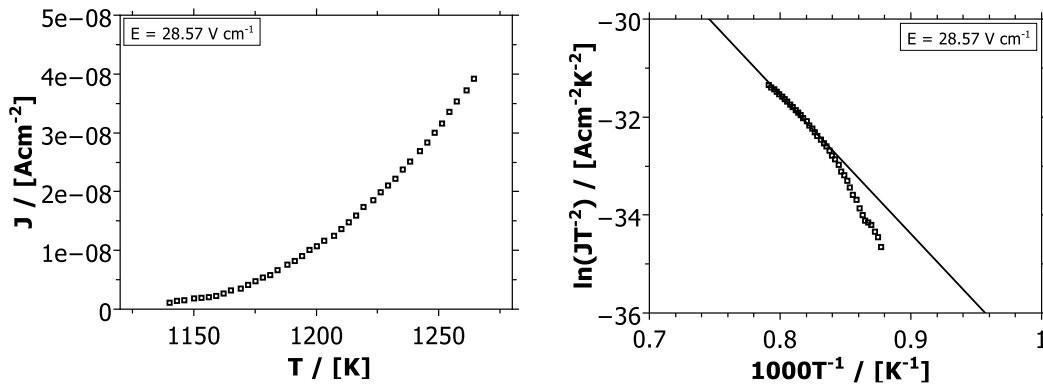


Fig. 80: Evaluation of data for determining the e- work function according to Richardson-Dushman measurement: REP IV (reproduction IV).

Table 14: Summary of the results of the linear regressions from the figures 77-80.

<i>measurement</i>	<i>m (slope)</i>	<i>electronic work function</i>	<i>R²</i>
REP I	-29.51	2.54	0.995
REP II	-27.83	2.40	0.998
REP III	-35.57	3.06	1.000
REP IV	-28.41	2.45	0.995
<i>average value = 2.61 ± 0.31 eV</i>			

5.3.3 Theoretical model

In this section, the detection process will be further discussed from a theoretical point of view. In order to give a better description of the process, the emission process and the subsequent recombination of K^+ ions on the detector plate can be illustrated via an energy Born cycle.

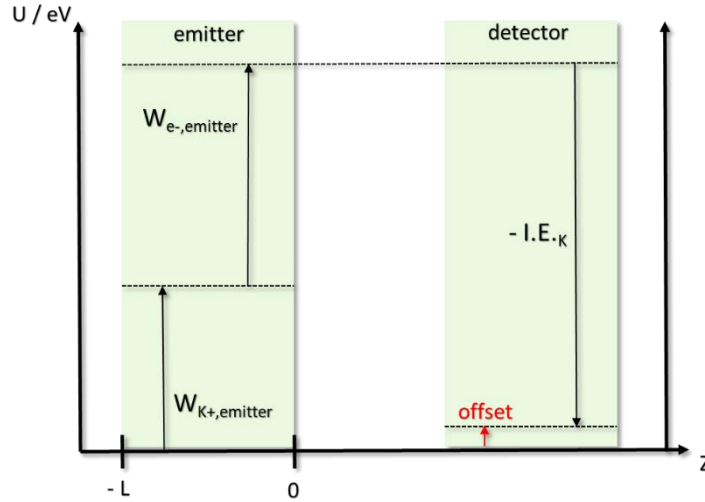


Fig. 81: Sketch of the relevant distances and the energy landscape for the thermionic emission and detection of K^+ ions from a $KAlSi_2O_6 : Mo$ (1:9) emitter.

On the graph of figure 81 the surface of the emitter is positioned at $z = 0$, the backside of the emitter material at $z = -L$ and afterwards is positioned the detection plate (either gold or steel). The process illustrated in figure 81, can be better described as follow: first, the ionic work function for the emission of potassium ions, $W_{K^+,emitter}$, needs to be overcome. At the same time, electrons are emitted from the emitter material, thus the electronic work function of the Leucite $KAlSi_2O_6 : Mo$ (1:9), $W_{e^-,emitter}$ must be exceeded. The electrons emitted from the emitter material are neutralized at the surrounding walls of the setup. Upon recombination of K^+ ions with electrons at the detector surface, the corresponding ionization energy of atomic potassium is gained $I.E.K = 4.341$ eV. Thus, the offset can be expressed as given in equation 68:

$$U_{Offset} = W_{K^+,emitter} + W_{e^-,emitter} - I.E.K \quad (68)$$

From the data of table 15 and according to the equation 68 a theoretical value of $U_{\text{Offset}} = 0.22$ eV is expected for the emission of potassium ions from $\text{KAlSi}_2\text{O}_6 : \text{Mo}$ (1:9).

Table 15: Data for the evaluation of the U_{Offset} , according to the equation (68).

<i>quantity</i>	<i>value</i>
$W_{K^+,emitter}$	1.95 ± 0.35 eV
$W_{e^-,emitter}$	2.61 ± 0.31 eV
$I.E._K$	4.341 eV*
* [177]	

Although the approach used to provide a theoretical model is similar between the case of this study and the case illustrated in literature from Schuld, however, the two theories seem to differ. As anticipated at the beginning of this section, the offset observed from Schuld *et al.* relies on the balance of the relevant energies involved in the process of the detection of Li^+ -ion current on a metal plate (i.e. the detector). At this point, it is important to emphasize that the emitter used within this literature work is a filament-type emitter, whereas the one used for this study is a pellet-type emitter (see section 4.1.1 for details and differences). According to their model, the U_{Offset} can be expressed as given in equations:

$$U_{\text{Offset}} (\text{Schuld}) = W_{\text{Li}^+,emitter} + W_{e^-,detector} + \Psi_{\text{fil}/det} - I.E._{\text{Li}} \quad (69)$$

with:

$$W_{e^-,detector} + \Psi_{\text{fil}/det} = W_{e^-,filament} \quad (70)$$

thus:

$$U_{\text{Offset}} (\text{Schuld}) = W_{\text{Li}^+,emitter} + W_{e^-,filament} - I.E._{\text{Li}} \quad (71)$$

By looking at the equation 69, the recombination of Li^+ ions onto a metal detector can be traced to a combination of: ionic work function of the emitter, electronic work function of the detector, contact potential between detector and filament and recombination energy $I.E_{Li}$. The same equation 69 can be rewritten considering the equation 70 to give the equation 71. A comparison between the two models will show up as follows:

$$U_{Offset} = W_{ionic,emitter} + W_{e^-,emitter} - I.E_{atom} \quad (72)$$

$$U_{Offset} (Schuld) = W_{ionic,emitter} + W_{e^-,filament} - I.E_{atom} \quad (73)$$

The difference between the two models is evident: in one case, it is the electronic work function of the emitting material which contributes, in the second case (Schuld *et al.*) the electronic work function of the filament needs to be taken into account. In order to understand the reason for the incongruity between the two cases, it could be useful to highlight the difference between a filament-type and a pellet-type emitter by means of a graphical illustration:

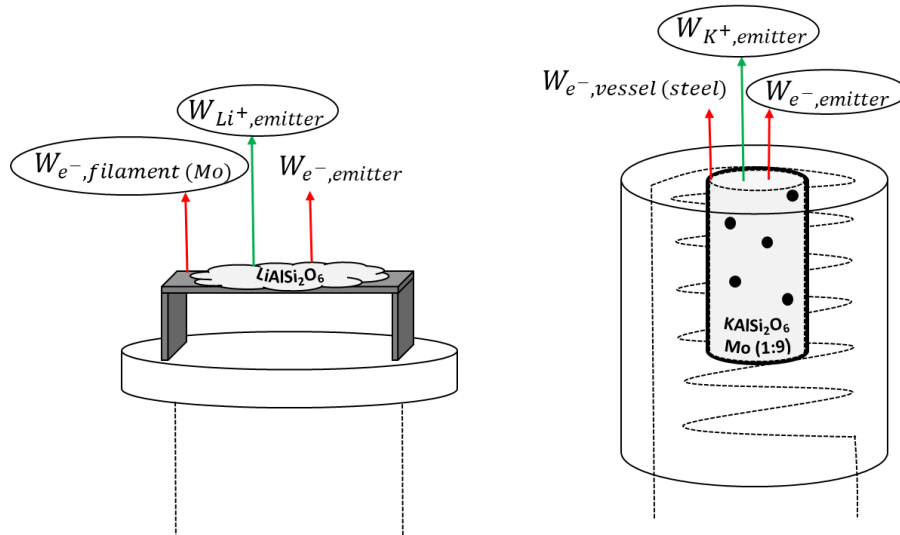


Fig. 82: Simple illustration of the emitter filament-type (left) and pellet-type (right). Arrows indicate the hypothetical emission of species (ions and e^-), whereas encircled indicate only the emission which occurs in the two cases respectively. More details in text.

Due to the high temperatures reached from the material, i.e. 750 °C to 800 °C, emission of ions and of electrons from the emitter material is expected in both cases, filament- and pellet-type emitter. Arrows sketched in figure 81 rely on the process of emission from the surface to the vacuum: each process is associated with a different work function, ionic work function for ion emission process and electronic work function for electron emission process. In addition to the emission of electrons from the material, emission of electrons from the surrounding metallic support could be considered as well. In case of a filament-emitter, the surrounding metallic support is represented from the filament itself, which is specifically made by molybdenum; in the case of a pellet-emitter, this is represented by the stainless steel vessel which contains the emitter material. If this is the case, then it would be meaningful to understand, why in the energy balance process of the pellet-type emitter the electronic work function of the Leucite $\text{KAlSi}_2\text{O}_6 : \text{Mo} (1:9)$ needs to be taken into account, whereas this is not the case for the filament-type emitter. Considering the values of electronic work functions:

Table 16: Electronic work function for the different elements mentioned.

<i>quantity</i>	<i>value</i>
$W_{e^-, \text{KAlSi}_2\text{O}_6 : \text{Mo}(1:9)}$	$2.61 \pm 0.31 \text{ eV}$
$W_{e^-, \text{LiAlSi}_2\text{O}_6}$	N/A*
$W_{e^-, \text{Mo}}$	4.6 eV
$W_{e^-, \text{steel}}$	4.46 eV
*not available	

The electronic work function for the Leucite is the lowest between the listed ones, but in particular is lower than $W_{e^-, \text{Mo}}$. Granted that, the reason why the energy balance contributions are different in the two models could rely on such low value of electronic work function. Even though the value for $W_{e^-, \text{LiAlSi}_2\text{O}_6}$ is not known, one could expect it to be not much different from the electronic work function of the molybdenum, perhaps even higher, since the $W_{e^-, \text{Mo}}$ is the relevant one. By looking at the right sketch of figure 82, black dots have been drawn within the emitter material. As already described in

section 4.1.1, the molybdenum has been added in order to guarantee a homogenous temperature of the material. Here the molybdenum content has been illustrated as conglomerates for simplicity reasons. A possible suggestion would be that the presence of the molybdenum could have played a role such that the actual electronic work function of the Leucite was lowered to a measured value of 2.61 eV. *Chow et al.* investigated Li^+ emission from spodumene mixed with molybdenum. The ionic work function was demonstrated to strongly depend on the molybdenum content of the emitter. Ionic work functions varying from 1.07 eV (85% Mo) to 3.26 eV (96% Mo) have been reported [178]. Although this study regards the influence of the molybdenum content on the ionic work function, however, it is not known to which extend the molybdenum content could influence the electronic work function as well. At this point in the discussion, it would be advantageous to perform extra experiments in order to measure the actual electronic work function for the spodumene ($\text{LiAlSi}_2\text{O}_6$). Further analyses seem to be needed in order to give a fuller understanding of the incongruities between the two models and this could be object of future research. With this study the author wants to stimulate further efforts in deriving thermodynamic quantities connected with the emission process of species from home-made emitter material such as Leucite KAlSi_2O_6 : Mo (1:x) and spodumene ($\text{LiAlSi}_2\text{O}_6$) : Mo (1:x).

6 Conclusions and outlook

Mold compounds

Mold compounds of the type MCP1, MCP2, MCP3, MCP4 have been analyzed by means of the CAIT technique, leading to the evaluation of values of ionic conductivity and activation energy related to the process of transport of potassium ions through the material under analysis. The four different types of MCP were bombarded by a continuous potassium ion beam in a range of repeller voltage of 5 eV - 30 eV. In the experiment, the backside current was investigated as a function of the ion kinetic energy for different temperatures of the sample: $T = 150\text{ }^{\circ}\text{C}$, $155\text{ }^{\circ}\text{C}$, $160\text{ }^{\circ}\text{C}$, $165\text{ }^{\circ}\text{C}$ and $T = 170\text{ }^{\circ}\text{C}$. The same tendency of current voltage characteristics, obeying to an Ohm's law like behavior, have been found for every kind of mold compounds analyzed. The ionic conductivity of the MCP compounds was on the order of $10^{-12}/10^{-13}$ S/cm. The activation energy for the ionic transport was determined by plotting the logarithm of the conductivity times the temperature as a function of the inverse temperature. The slope of the resulting curve yielded the activation energy which was found to be 1.5 eV – 2 eV for a MCP1 sample. The activation energy values for the rest of the mold compounds MCP2, MCP3, MCP4 was found to be similar, i.e. in a range of 1.3 eV - 2.7 eV. Measurements of conductivities and activation energies were repeated several times to check for the reproducibility, leading to the conclusion that from the same type of mold compounds, e.g. MCP1, slightly different values of conductivity, as well as activation energies, are obtained. Some of the samples have been treated with heat in order to see whether the treatment of the material would have caused modification on the conductivity or activation energy values. The heating process consisted of heating up the substrate into an ambient pressure oven from $130\text{ }^{\circ}\text{C}$ up to $250\text{ }^{\circ}\text{C}$, in steps of $5\text{ }^{\circ}\text{C}$ each 5 minutes. Right after the thermal treatment of the sample a CAIT analysis has been performed, showing very low detected backside current, thus any temperature dependent current-voltage characteristic could not be determined. This effect was justified taking into account a change in the inner structure of the material which lowered the ion mobility inside the sample. As the final part of the study regarding conductivity and activation energy, a comparison of the data obtained by means of two different techniques has been presented. Results achieved with electrochemical impedance spectroscopy (EIS) and CAIT methods were found to be in good agreement.

For a better understanding of the potassium diffusion process into the mold compounds, the diffusion of potassium through MCP3 sample has been investigated via a combination of CAIT method and an ex-situ ToF-SIMS analysis. The sample has been bombarded using a potassium ion beam with an energy of 19 eV for 19 days at a temperature of 170 °C. A ToF-SIMS analysis was successively performed, revealing a depth diffusion profile of the potassium into the material. The ToF-SIMS analysis revealed a similar profile in the signals F^+ and SiF^+ which could be interpreted as caused from a diffusion of those species toward the surface which was triggered from the bombardment. ToF-SIMS analysis onto a fresh and not treated sample of the same type of mold compound MCP3 confirmed the lack of a migration profile for SiF^+ and F^+ signals in a not-bombarded sample. With respect to the potassium concentration profile, the evaluation of a plot of the natural logarithm of the intensity versus the squared depth revealed two upper limiting values of diffusion coefficients associated with the transport of potassium through the MCP3 sample. The evaluation of the 2D chemical maps collected during the ToF-SIMS analysis showed the presence of two different transport pathways operative inside the material. Part of the potassium diffuses along the boundaries of grains, i.e. zones of accumulation of the inorganic component of the mold compounds, whereas the rest of the potassium diffuses through the bulk, i.e. through the inorganic component of the mold compound. The presence of grains within the mold compounds has been validated from a SEM analysis performed onto a fresh and not-treated sample of MCP3, where a typical structure of a mold compound with spherical silica was visible. A mathematical theory has been established in order to evaluate the diffusion coefficients for the transport of potassium ion through the specific mold compound MCP3. The numerical simulations have been performed based on the Nernst-Planck-Poisson equations: the ion flux density which depends on the diffusion coefficient D , the electric potential given by a certain ion distribution and Fick's second law were taken into account in the mathematical procedure. According to the numerical procedure used for the theoretical model, the ions are deposited at the frontside of the sample and enter either the bulk of a grain or a grain boundary. In the specific case, a good fit between experimental and theoretical data was achieved assuming that 80 % of the incoming ions enter a grain boundary and assuming diffusion coefficients of $D_B = 1.8 \times 10^{-21} \text{ cm}^2\text{s}^{-1}$ and $D_{BG} = 5.4 \times 10^{-20} \text{ cm}^2\text{s}^{-1}$ for bulk and grain boundary diffusion, respectively. The highest value of D is associated with the diffusion along the grain boundaries (GB) since is usually faster than the bulk diffusion.

With the study conducted within this thesis, investigation of ion diffusion in microcircuit encapsulation materials, e.g. mold compounds, has been performed. A combination of charge attachment induced transport technique (CAIT) and time-of-flight-secondary-ion-mass-spectrometry (TOF-SIMS) allowed qualitative and quantitative analysis. Provided that the issue of ion contamination represents a well-known concern in the field of electronic packages, the analysis conducted within this study leads to the determination of information regarding the transport properties of potassium ions through the specific mold compounds.

Polyelectrolyte multilayers

PEM films studied in this work were prepared from the layer-by-layer assembly of ionic *p*-sulfonato-calix[8]arene (calix8) and cationic poly(allylamine hydrochloride) (PAH) onto functionalized gold substrates. Discussions on the dependence of the conductance with the number of bilayers, as well as on the temperature dependence of the conductance for a (PAH/calix8)₃₀, led to the conclusion that the system investigated could have been influenced from external conditions, i.e. from the type of construction design used as support for the (PAH/calix8)_n multilayers. However, results of conductance study were presented as a meaningful example on how the choice of a suitable substrate system could be crucial for the realization of the CAIT analysis. In order to determine the conductance of (PAH/calix8)_n as a function of the number of bilayers, samples with $n = 1, 3, 6, 9, 12, 15, 20, 30$ bilayers were analyzed. The samples have been bombarded with a spatially homogeneous potassium ion beam using voltages between 2 V and 10 V and a temperature range from 70 °C to 80 °C. From results of the temperature dependence of the conductance, a value of activation energy E_{act} has been derived which turned out to be not consistent with the expected one on the basis of previous literature data. In particular, all the data lent support to the conclusion that the glass resistance, instead of the resistance of the PEMs, has been measured during the experiments. Using a different construction as a support system, new ion conductance studies by means of the CAIT technique have been performed. Results of current–voltage characteristic for PAH/calix8 with 9 bilayers were shown, where no correlation between the measured backside current with the variation of the temperature was found. The data lent support to the conclusion that conductivity, as well as activation energy measurements for (PAH/calix8)_n, could not be acquired under the conditions of the CAIT method, due to the low resistivity shown

from the PEMs. Qualitatively analysis of ToF-SIMS depth profiles of (PAH/calix8)₁₅ was presented. Two samples of (PAH/calix8)₁₅ have been bombarded with a homogeneous potassium ion beam, using different bombarding time, leading to the incorporation of a different amount of charge within the PEMs film. The trend of the two concentration profiles reflects the different charge incorporated. In one case an incorporated charge of $Q = 6.6 \mu\text{C}$ led to a complete filling up of the membrane, in the other case $0.64 \mu\text{C}$ of charge incorporated led to the formation of a diffusion profile within the first 50 sputter second. However, the interpretation of the depth profiles could not be univocal, since the (PAH/calix8)₁₅ film was found to have heterogeneity at the surface, compromising the conditions of acquisition for the ToF-SIMS analysis. Finally, studies on the transport of Li^+ , K^+ and Rb^+ through (PAH/calix8)₃₀ were presented. Evaluation of ToF-SIMS depth profiles, together with a theoretical model and numerical simulations based on the Nernst–Planck–Poisson theory, provided a full quantitative understanding of the transport process of Li^+ and Rb^+ through (PAH/calix8)₃₀ multilayer. For the K^+ case, a quantitative evaluation of the data was not conducted: K^+ ions were found to be present into the PEMs already prior to the bombardment as a contaminant. For each ion beam (Li^+ , K^+ , Rb^+) two kind of experiments have been performed: (PAH/calix8)₃₀ samples were bombarded with the three different alkali ions varying the time for the bombardment, i.e. 5 seconds in one case and 100 seconds in the other, leading consequently to a different amount of charge accumulated into the membrane. A comparison of diffusion profiles showed a different behavior for Li^+ , K^+ and Rb^+ . On the one hand, the difference between the 5 seconds and the 100 seconds bombardment appears to be consistent with higher values for the charge accumulated. On the other hands the diffusion profiles within the series Li^+ , K^+ and Rb^+ differ in their trend. Only the Li^+ signal showed a diffusion profile with its intensity dropping exponentially from the very beginning of the membrane layer to the end of the film at 40 nm, whereas the Rb^+ signal showed in the same depth range no diffusion profile but an almost constant tendency. For the K^+ the trend fell in between the two previous cases. Finally, numerical analysis of the lithium and rubidium concentration profiles for 5 seconds long bombardment onto (PAH/calix8)₃₀ were presented. By means of a theoretical model, the concentration profiles were modelled within the thickness of the film. For the lithium case, the model used to examine the ion transport across the membrane resulted in a combination of two diffusion pathways accounting for diffusion of slow lithium ions and fast lithium ions. A good fit was achieved using diffusion

coefficients of $D_{\text{slow}} = 0.4 \times 10^{-16} \text{ cm}^2/\text{s}$ and $D_{\text{fast}} = 1.2 \times 10^{-15} \text{ cm}^2/\text{s}$ and assuming that 40% of the incoming ions enter the slow pathway, whereas the rest of the ions is transported via a fast pathway. For the rubidium case, the numerical calculation revealed that the fast diffusion pathway is predominant: only the 0.01% of the rubidium ions enter the slow pathway, whereas the rest is dominated from the faster one. The D_{fast} for the rubidium, i.e. $D_{\text{fast,Rb}^+} = 7 \times 10^{-15} (\pm 1.5 \times 10^{-15}) \text{ cm}^2/\text{s}$, was found to be higher than the D_{fast} for the lithium, due to the fact that hopping mechanisms, which control the fast pathway, are enhanced in the case of the rubidium. The study of ion transport of alkali ions Li^+ and Rb^+ across PEMs containing calixarenes leads thus to the conclusion that the presence of the calixarenes units may influence the type of transport: part of the ions is retarded on their transport, due to the interaction with the negative pendant groups of the calixarenes, while the rest of the ions passes through the membrane via hopping transport between discrete sites. This study wanted to shed further light on the mechanism of transport of alkali ions through polyelectrolytes multilayers based on calixarenes, being the latter one of the most important macrocyclic host molecules and important building blocks in supramolecular chemistry.

Measurements of offsets in the CAIT detection process

This study aimed to give a better understanding of the process beyond the voltage offset measured on a typical current-voltage curve in a charge attachment induced transport experiment. In order to do that, a basic experiment has been performed, where a metal plate has been bombarded with an ion beam from a potassium emitter of the composition $\text{KAlSi}_2\text{O}_6 : \text{Mo}$ (1: 9). For each experiment the repeller voltage has been varied in a range 0.5 V – 5 V, in steps of 0.2 V. Two different metal plates were used as a detector, i.e. gold and stainless steel and for both cases the current–voltage curves showed finite offsets in the order of 0.5 eV, leading to the conclusion that no meaningful influence comes from the type of metal electrode used as detector plate. In order to investigate the detection process of the specific $\text{KAlSi}_2\text{O}_6 : \text{Mo}$ (1:9) emitter, ionic and electronic work function measurements were performed. The investigation of the temperature dependence of the emission current brought to the evaluation of the work function, according to the Richardson-Dushman law. A value of $1.95 \pm 0.35 \text{ eV}$ and $2.61 \pm 0.31 \text{ eV}$ have been found for the ionic work function and the electronic work function, respectively. Ultimately a theoretical model based onto recombination of energy quantities has been suggested. The

recombination of K^+ ions from Leucite $KAlSi_2O_6 : Mo (1:9)$ onto a metal detector has been traced to a combination of the ionic work function of the emitter material, the electronic work function of the emitter material and the recombination energy of the elemental potassium I.E._K. A comparison of this model with another model developed in the literature has been discussed. The two model rely on different energy balance contributions of the emission/detection process of ions from a home-made emitter to a metal detector. The incongruities between the two models have been traced back to the different composition of the two emitter material, i.e. pure syntetic spodumene ($LiAlSi_2O_6$) from the one hand and a mixer of molybdenum and Leucite, $KAlSi_2O_6 : Mo (1:9)$, from the other hand. With this study, the author wants to stimulate further efforts in deriving thermodynamic quantities connected with the emission process of species from home-made emitter materials such as Leucite $KAlSi_2O_6 : Mo (1:x)$ and spodumene ($LiAlSi_2O_6$) : $Mo (1:x)$.

7 References

- [1] M. Schäfer, K. Lange, K. Rohmann, A. Schlemmer, B. Roling and K. M. Weitzel, *Proceedings 2010 IEEE ICSD*, 655-658, (2010).
- [2] P. Menezes, J. Martin, M. Schäfer, B. Staesche, B. Roling and K. M. Weitzel, *Physical Chemistry Chemical Physics*, 13, 20123-20128, (2011).
- [3] M. Schäfer and K. M. Weitzel, *Phys. Chem. Chem. Phys.*, 13, 20112-20122, (2011).
- [4] L. Rossrucker, P. Menezes, J. Zakel, B. Roling and K. M. Weitzel, *Z. Phys. Chem.*, 341-353, (2012).
- [5] S. Schulze, J. Zakel, M. Schäfer and K. M. Weitzel, *IEEE-TDEI*, 19, 1167-1174, (2012).
- [6] S. Carregal-Romero, Rinklin P., S. Schulze, M. Schäfer, A. Ott, D. Hühn, B. Wolfrum, K. M. Weitzel and W. J. Parak, *Macromolecular Rapid Communications*, 34, 1820, (2013).
- [7] V. Wesp, M. Hermann, M. Schäfer, J. Hühn, W. J. Parak and K. M. Weitzel, *Physical chemistry chemical physics: PCCP*, 18(6), 4345-4351, (2016).
- [8] Y. Nishi and R. Doering, *Handbook of Semiconductor Manufacturing Technology*, Second Edition, 28 - 31: CRC Press, (2007).
- [9] M. Pecht and L. Lantz, *IEEE Transactions on Components and Packaging Technologies*, 26(1), 199, (2003).
- [10] L. Lantz, M. Pecht and M. Wood, *IEEE Transactions on Components and Packaging Technologies*, 31(3), 527, (2008).
- [11] S. Schwab, J. Jung, S. Gruber, M. Bauer, S. Miethaner, M. Neihiebel and H. Hutter, *ECS Journal of Solid State Science and Technology*, 5, N72-N76, (2016).

- [12] S. Schwab, J. Appenroth, M. Bonta, S. Holzer, M. Bauer, S. Miethaner, A. Limbeck, M. Nelhiebel and P. Weinberger, in *IEEE 67th Electronic Components and Technology Conference*, Orlando, FL, USA, (2017).
- [13] W. Jin, A. Toutianoush and B. Tieke, *Langmuir*, 19, 2550, (2003).
- [14] A. Toutianoush, W. Jin, H. Deligöz and B. Tieke, *Appl. Surf. Sci.*, 246:437, (2005).
- [15] W. Jin, A. Toutianoush and B. Tieke, *Appl Surf Sci*, 246:444, (2005).
- [16] J. Cheug, A. Fou and M. Rubner, *Thin Solid Film*, 284, 985, (1995).
- [17] P. Hammond and G. Whitesides, *Macromolecules*, 28, 7569, (1995).
- [18] W. Huck, L. Yan, A. Stroock, R. Haag and G. Whitesides, *Langmuir*, 15, 6862, (1999).
- [19] Y. Lvov, K. Ariga, M. Onda, I. Ichinose and T. Kunitake, *Langmuir*, 13, 6195, (1997).
- [20] J. Harris and M. Bruening, *Langmuir*, 16, 2006, (2000).
- [21] Z. Asfari, V. Boehmer, J. Harrowfield and J. Vicens, *Calixarenes 2001*, The Netherlands: Kluwer, Dordrecht, (2001).
- [22] X. Yan, V. Janout, J. Hsu and S. Regen, *J. Am. Chem. Soc.*, 124, 10962, (2002).
- [23] M. Conner, V. Janout, I. Kudelka, P. Dedek, J. Zhu and S. Regen, *Langmuir*, 9, 2389, (1993).
- [24] X. Yang, S. Johnson, J. Shi, T. Holesinger and B. Swanson, *Sens. Actuators B*, 45, 87, (1997).
- [25] A. Toutianoush, J. Schnefp, A. El Hashani and B. Tieke, *Adv Funct Mater*, 15:700, (2005).

-
- [26] Y. Lvov, A. Antipov, A. Mamedov, H. Moehwald and G. Sukhorukov, *Nano Lett.*, 3, 125-128, (2001).
- [27] H. Moehwald and Y. Lvov, *Protein Architecture: Interfacial Molecular Assembly and Immobilization Biotechnology*, M.Dekker Publ., NY, 125-167, (2000).
- [28] F. Shi, Z. Wang, N. Zhao and X. Zhang, *Langmuir*, 21, 1599-1602, (2005).
- [29] A. Rogach, D. Koktysh, M. Harrison and N. Kotov, *Chem. Mater.*, 12, 1526-1528, (2000).
- [30] J. Xu, Y. Wiezmann, N. Kriekhely, R. Baron and I. Willner, *Small*, 2, 1178-1182, (2006).
- [31] J. Harris, P. De Rose and M. Bruening, *J. Am. Chem. Soc.*, 121, 1978-1979, (1999).
- [32] X. Roy, P. Sarazin and B. Favis, *Adv. Mater.*, 18, 1015-1019, (2006).
- [33] E. Vázquez, D. Dewitt, P. Hammond and D. Lynn, *J. Am. Chem. Soc.*, 124, 13992-13993, (2002).
- [34] R. Iler, *Colloid Interface Sci.*, 21, 569-594, (1966).
- [35] G. Decher, J. Hong and J. Schmitt, *Thin Solid Films*, 210-211, 831-835, (1992).
- [36] G. Decher and J. Hong, *Macromol. Chem. Macromol. Symp.*, 46, 321-327, (1991).
- [37] G. Decher and J. Schlenoff, *Multilayer Thin Films Sequential Assembly of Nanocomposite Materials*, Wiley-VCH, (2012).
- [38] P. Hammond, *AIChE J.*, 16, 1271-1293, (2011).
- [39] P. Patel, J. Jeon, P. Mather and A. Dobrynin, *Langmuir*, 22, 9994-10002, (2006).
- [40] J. Schlenoff, H. Ly and M. Li, *J. Am. Chem. Soc.*, 120, 7626-7634, (1998).

- [41] M. Lösche, J. Schmitt, G. Decher, W. Bouwman and K. Kjae, *Macromolecules*, 31, 8893-8906, (1998).
- [42] E. Hubsch, V. Ball, B. Senger, G. Decher, J. Voegel and P. Schaaf, *Langmuir*, 20, 1980-1985, (2004).
- [43] B. Schoeler, G. Kumaraswamy and F. Caruso, *Macromolecules*, 35, 889-897, (2002).
- [44] A. Dobrynin and M. Rubinstein, *Polym. Sci.*, 30, 1049-1118, (2005).
- [45] G. Liu, S. Zou, L. Fu and G. Zhang, *J. Phys. Chem. B*, 112, 4167-4171, (2008).
- [46] G. Liu, Y. Hou, X. Xiao and G. Zhang, *J. Phys. Chem. B*, 114, 9987-9993, (2010).
- [47] S. Dubas and J. Schlenoff, *Macromolecules*, 34, 592, (2001).
- [48] J. Schlenoff, H. Ly and M. Ly, *J. Am. Chem. Soc.*, 120, 7626, (1998).
- [49] H. van de Steeg, M. Cohen-Stuart, A. de Keizer and B. Bijsterbosch, *Langmuir*, 8, 2538, (1992).
- [50] S. Park, R. Bruinsma and W. Gelbart, *Europhys. Lett.*, 46, 454, (1999).
- [51] F. Essler and H. Riegler, *Langmuir*, 18, 6694, (2002).
- [52] S. Schlenoff and J. Dubas, *Macromolecules*, 34, 3736, (2001).
- [53] J. Schlenoff and S. Dubas, *Langmuir*, 17, 1184, (2001).
- [54] T. Farhat and J. Schlenoff, *Langmuir*, 17, 1184, (2001).
- [55] T. Farhat and J. Schlenoff, *J. Am. Chem. Soc.*, 125, 4627, (2003).
- [56] K. Lebedev, P. Rami'rez, S. Mafe and J. Pellicer, *Langmuir*, 16, 9941, (2000).

- [57] H. Miyoshi, *J. Membr. Sci.*, 141, 101, (1998).
- [58] A. Balachandra, J. Dai and M. Bruening, *Macromolecules*, 35, 3171, (2002).
- [59] M. Bruening and D. Sullivan, *Chem. Eur. J.*, 8, 3833, (2002).
- [60] G. Decher, *Science*, 277, 1232, (1997).
- [61] R. Steitz, V. Leiner and R. Klitzing, *Colloids Surf. A*, 163, 63, (2000).
- [62] J. Ruths, J. Essler, G. Decher and H. Riegler, *Langmuir*, 16, 8871, (2000).
- [63] Y. Lvov, K. Ariga, M. Onda, I. Ichinose and T. Kuitake, *Colloids Surf. A*, 146, 337, (1999).
- [64] G. Ladam, P. Schaad, J. Voegel, P. Schaaf, G. Decher and F. Cuisinier, *Langmuir*, 16, 1249-1255, (2000).
- [65] F. Caruso, E. Donath and H. Möhwald, *J. Phys. Chem. B*, 102, 2011, (1998).
- [66] T. Silva, S. Barreira, C. Moura and A. Silva, *Port. Electrochim. Acta*, 21, 281, (2003).
- [67] S. Barreira, V. García-Morales and C. Pereira, *J. Phys. Chem. B*, 108, 17973-17982, (2004).
- [68] Y. Sakamoto and S. Komari, *Materials for Advanced Packaging*, Chapter 10, D. Lu and CP Wong Editors, Springer, (2009).
- [69] J. Gotro, "Polymers in Electronic Packaging Part One: Introduction to Mold Compounds" Available: <https://polymerinnovationblog.com> [Accessed 17 April 2019].

- [70] J. Gotro, "Polymers in Electronic Packaging Part Two: Epoxy Mold Compounds, Thermosets in Action" Available: <https://polymerinnovationblog.com> [Accessed 27 April 2019].
- [71] H. Mehrer, *Diffusion in Solids: Fundamentals, Methods, Materials, Diffusion-Controlled Processes*, Springer, (2007).
- [72] A. Einstein, *Annalen der Physik*, 17, 549, (1905).
- [73] M. von Smoluchowski, *Annalen der Physik*, 21, 756, (1906).
- [74] M. von Smolouchowski, *Z.Phys.*, 13, 1069, (1912).
- [75] J. C. Dyre, P. Maass, B. Roling and D. L. Sidebottom, *Reports on Progress in Physics*, 72 (4), 046501, (2009).
- [76] S. Baranovski, *Charge Transport in Disordered Solids*, Wiley, (2006).
- [77] R. Barnes, *Nature*, 166, 1032, (1950).
- [78] A. Le Claire, *Philos. Mag.*, 42, 468, (1951).
- [79] J. Fisher, *J.Appl.Phys.*, 22, 74, (1951).
- [80] L. Harrison, *Trans. Faraday Soc.*, 57, 1191, (1961).
- [81] W. Dyrka, A. T. Augousti and M. Kotulska, *J. Comput. Chem.*, 29, 1876, (2008).
- [82] J. Schlenoff, H. Ly and M. Li, *J. Am. Chem. Soc.*, 120, 7626, (1998).
- [83] F. Essler and H. Riegler, *Langmuir*, 18, 6694, (2002).
- [84] B. Tieke and L. Krasemann, *Langmuir*, 16, 287, (2000).
- [85] M. Urairi, T. Tsuru, S. Nakao and S. Kimura, *J. Membr. Sci.*, 70, 153, (1992).

- [86] J. Harris, *Chem. Mater.*, 12, 1941, (2000).
- [87] J. Schlenoff and T. R. Farhat, *J. A. Chem. Soc.*, 125, 4627, (2003).
- [88] T. Farhat and J. Schlenoff, *Langmuir*, 17, 1184, (2001).
- [89] T. Radeva, *Physicl Chemistry of Polyelectrolytes*, (2001).
- [90] F. Helfferich, *Ion Exchange*, McGraw-Hill: New York: Chapter 8, (1962).
- [91] P. Egelstaff, *An introduction to the Liquid State*, Academic Press Inc.: New York Chapter 10, 119-132, (1967).
- [92] S. Dushman, *Rev. Mod. Phys.*, 2, 0381, (1930).
- [93] I. Langmuir, *Phys. Z.*, 15, 516, (1914).
- [94] E. J. Jones and J. P. Blewett, *Phys. Rev.*, 50, 464, (1936).
- [95] D. Chattopadhyay, *Electronics (fundamental and application)*, New Age International Pvt Ltd Publisher, (2006).
- [96] S. Dushman, *Phys. Rev.*, 21, 623, (1923).
- [97] F. W. Smith and J. I. Gersten, *The Physics and Chemistry of Materials*, Wiley, (2001).
- [98] C. D. Child, *Phys. Rev. (Ser. I)*, 32, 492, (1911).
- [99] O. W. Richardson, *The Emission of Electricity from Hot Bodies*, Longmans, Green and Co., London, (1916).
- [100] R. W. Wright, *Phys. Rev.*, 60, 465, (1941).
- [101] W. Schottky, *Z. Phys.*, 14, 63, (1923).

- [102] C. S. Ryu, Charge Control With Lithium Ion Source And Electron, Master Thesis, Naval Postgraduate School, California, (1990).
- [103] M. Wakihara, *Sci. Eng. R.*, 33, 109-134, (2001).
- [104] A. Bagiani, V. Ghiaroni and F. Fieni, *Prog. Biophys. Mol. Biol.*, 83, 193-225, (2003).
- [105] I. Terzic, M. M. Tasic and J. Alazar, *Meas. Sci. Technol.*, 7, 944-948, (1996).
- [106] K. K. Chow, H. S. Maddix and P. Chorney, *Appl. Phys. Lett.*, 10, 256, (1967).
- [107] R. K. Feeney, W. E. Sayle and J. W. Hooper, *Rev. Sci. Instrum.*, 47, 964, (1976).
- [108] R. D. Banhatti e K. Funke, *Solid State Ionics*, 177, 1551, (2006).
- [109] B. Roling, C. Martiny and S. Bruckner, *Phys. Rev. B: Condens. Matter*, 6321, 214203, (2001).
- [110] C. Brinkmann, S. Faske, B. Koch and M. Vogel, *Z. Phys. Chem.*, 224, 535, (2010).
- [111] R. Bohmer, K. Jeffery and M. Vogel, *Prog. Nucl. Magn. Reson. Spectrosc.*, 50, 87, (2007).
- [112] S. Arumugan, J. Shi, D. Tunstall and C. Vincent, *J.Phys.:Condens. Matter*, 5, 153, (1993).
- [113] L. van Wüllen, T. Echelmeyer, N. Voigt, T. K. Koster and G. Schiffmann, *Z. Phys. Chem.*, 224, 1735, (2010).
- [114] M. Lepke, P. Fieliz, G. Borchardt, G. H. Frischat, A. Goss and E. Posl, *J. Non-Cryst. Solids*, 356, 1604, (2010).
- [115] R. Dieckmann and L. Tian, *J.Non-Cryst.Solids*, 265, 36, (2000).
- [116] H. Mehrer, *Z.Phys.Chem*, 223, 1143, (2009).

- [117] M. Martin and R. A. De Souza, *Phys. Chem. Chem. Phys.*, 10, 2356, (2008).
- [118] J. Janek, *Solid State Ionics*, 131, 129, (2000).
- [119] M. Schäfer, K. Lange, K. N. Rohmann, A. Schlemmer, B. Roling and K. M. Weitzel, *Proceedings 2010 IEEE ICSD*, 655-658, (2010).
- [120] D. Budina, J. Zakel, J. Martin, P. V. Menezes, M. Schäfer and K. M. Weitzel, *Zeitschrift für Physikalische Chemie*, 228(4-5), (2014).
- [121] J. Zakel, P. V. Menezes, M. Schäfer and K. M. Weitzel, *Solid State Ionics*, 242, 20-25, (2013).
- [122] I. M. Hodge, M. D. Ingram and A. R. West, *J. Electroanal. Chem.*, 76, 125-143, (1976).
- [123] J. C. Vickermann and D. Briggs, "TOF-SIMS: Material Analysis by Mass Spectrometry," *IM Publications*, (2013).
- [124] J. C. Vickermann and N. Vinograd, *International Journal of Mass Spectrometry*, 377, 568-579, (2015).
- [125] J. J. Thomson, *Phil. Mag.*, 20, 252, (1910).
- [126] F. P. Viebock and R. F. Herzog, *Phys. Rev.*, 76, 855L, (1949).
- [127] R. F. Herzog and H. J. Liebl, *J. Appl. Phys.*, 34, 2893, (1963).
- [128] G. Slodzian and R. Castaing, *J. Microscopy*, 1, 395, (1962).
- [129] A. Benninghoven, *Z. Physik*, 230, 403, (1970).
- [130] A. Benninghoven, F. G. Rudenauer and H. W. Werner, *Secondary Ion Mass Spectrometry*, New York: John Wiley & Sons, (1987).

- [131] A. Delcorte, P. Bertrand and B. J. Garrison, "Collision cascade and sputtering process in a polymer," *J. Phys. Chem. B.*, 105, 9474-9486, (2001).
- [132] I. Gilmore and M. Seah, "Cluster primary ion sputtering: Correlations in secondary ion intensities in TOF SIMS," *Surf. Interface Anal.*, 43, 228-235, (2011).
- [133] T. S. Nunney and M. P. Seah, "Sputtering yields of compounds using argon ions," *J. Phys. D. Appl. Phys.*, 43, (2010).
- [134] M. P. Seah, *J. Phys. Chem. C.*, 117, 12622-12632, (2013).
- [135] F. Kollmer, "Cluster primary ion bombardment of organic materials," *Appl. Surf. Sci.*, 231-232, (2004).
- [136] L. Nittler, A. Delcorte, P. Bertrand and H. N. Migeon, *Surf. Interface Anal.*, 45, 18-21, (2013).
- [137] A. Delcorte and O. A. Restrepo, *Surf. Interface Anal.*, 43, 70-73, (2011).
- [138] "Heidelberg Ion Probe: Instrumentation - SIMS Basics", Available: <https://www.geow.uni-heidelberg.de> [Accessed 17 April 2019].
- [139] P. T. Murray and J. W. Rabalais, 549, 1007-1013, (1981).
- [140] A. M. Spool, *The Practice of TOF-SIMS: Time of Flight Secondary Ion Mass Spectrometry*, Momentum Press, (2016).
- [141] B. A. Mamyrin, "Time-of-flight mass spectrometry (concepts , achievements , and prospects)", 206, 251-266, (2001).
- [142] F. Güthe, M. Malow, K. M. Weitzel and H. Baumgärtel, *International Journal of Mass Spectrometry and Ion Processes*, 172, 47 - 55, (1998).
- [143] F. Güthe, Dissertation, Freien Universität Berlin, (1997).

- [144] "Optical Profilometry" Available: <https://www.nanoscience.com> [Accessed 17 April 2019].
- [145] M. Hughes, "What is DC Sputtering?" Available: <http://www.semicore.com> - [Accessed 17 April 2019].
- [146] J. P. Blewett and E. J. Jones, *Phys. Rev.*, 50, 464, (1936).
- [147] T. Kolling, A. Schlemmer, C. Pietzonka, B. Harbrecht and K. M. Weitzel, *J. Appl. Phys.*, 107, 014105, (2010).
- [148] S. Schuld, Master thesis, Philipps University Marburg, (2012).
- [149] Y. Lvov, G. Decher and H. Möhwald, *Langmuir*, 9, 481, (1993).
- [150] N. B. Singh, *Polymer Degradation and Stability*, 93, 93561-584, (2008).
- [151] M. Mengel et al., *Journal of reinforced plastics and composites (Issue 16)*, 23, 1766-1765, (2004).
- [152] K. M. Jansen, J. de Vreugd, L. Ernst and C. Bohm, "Thermal Aging of Molding Compounds", *Conference paper: September 2010*.
- [153] M. L. Minges, *Electronic Materials Handbook: Packaging, Novelty*: ASM International, (1989).
- [154] A. Hein, J. Martin, M. Schäfer and K. M. Weitzel, *J. Phys. Chem. C*, 121 (6), 3203-3211, (2017).
- [155] H. Mehrer, "Diffusion in solids. Fundamentals, Methods, Materials, Diffusion-Controlled Processes", Springer, 155, (2007).
- [156] F. Caruso, K. Niikura, D. N. Furlong and Y. Okahata, *Langmuir*, 13, 3422-3426, (1997).

-
- [157] J. J. Ramasden, Y. Lvov and G. Decher, *Thin Solid Films*, 254, 246-251, (1995).
- [158] P. Lavalle, C. Gergely, F. J. Cuisinier, G. Decher, P. Schaaf, J. C. Voegel and C. Picart, 35, 4458-4465, (2002).
- [159] C. Picart, G. Ladam, B. Senger, J. C. Voegel, P. Schaaf, F. J. Cuisinier and C. Gergely, *J.Chem.Phys*, 115, 1086, (2001).
- [160] J. Martin, S. Mehrwald, M. Schäfer, T. Kramer, C. Jooss and K. M. Weitzel, *Electrochimica Acta*, 191, 616, (2016).
- [161] M. F. Durstock and M. F. Rubner, *Langmuir* 17, 25, 7865-7872, (2001).
- [162] D. M. De Longchamp and P. T. Hammond, *Chem. Mater.*, 15, 1165-1173, (2003).
- [163] D. M. De Longchamp and P. T. Hammon, *Langmuir* 20, 13, 5403-5411, (2004).
- [164] Y. Akgöl, C. Hofmann, Y. Karatas, C. Cramer, H. D. Wiemhöfer and M. Schönhoff, *J.Phys.Chem.B(111)*, 29, 8532-8539, (2007).
- [165] A. A. Argun, J. N. Ashcraft, M. K. Herring, D. K. Lee, H. R. Allcock and P. Hammond, *Chem. Mater.* 22, 1, 226-232, (2010).
- [166] P. Bieker and M. Schönhoff, *Macromolecules*, 43, 5052-5059, (2010).
- [167] K. Büscher, K. Graf, H. Ahrens and C. A. Helm, *Langmuir*, 18, 3585-3591, (2002).
- [168] J. N. Ashcraft, A. A. Argun and P. T. Hammond, *J.Mater.Chem.*, 20, 6250-6257, (2010).
- [169] X. Zhang, C. Jang, M. Cheng, Y. Zhou, X. Zhu, J. Nie, Y. Zhang, Q. An and F. Shi, *Langmuir*, 28, 7096-7100, (2012).
- [170] M. A. Pechenkin, H. Möhwald and D. V. Volodkin, *Soft Matter*, 8, 8659, (2012).
- [171] C. D. Gutsche and L. J. Bauer, *J. Chem. Soc.*, 107, 6052, (1985).

- [172] T. R. Farhat and J. B. Schlenoff, *Langmuir*, 17, 1184-1192, (2001).
- [173] J. B. Schlenoff and T. R. Farhat, *J. Am. Chem. Soc.*, 125, 4627-4636, (2003).
- [174] H. Kösters, *Z.Phys.*, 66, 807, (1930).
- [175] E. Spenke, *Elektronische Halbleiter*, Springer Berlin Heidelberg, (1965).
- [176] S. Schuld, M. Diekmann and K. M. Weitzel, *Journal of Applied Physics*, 120, 185102, (2016).
- [177] *Periodensystem der Elemente: Nach Fluck und Heumann unter Berücksichtigung der IUPAC-Empfehlungen bis 2006*, Weinheim: Wiley-VCH, (2007).
- [178] K. K. Chow, H. Maddix and P. Chorney, *Appl. Phys. Lett.*, 10, 256, (1967).

8 Appendix

Appendix A. Temperature dependent current–voltage characteristics and temperature dependence of the specific conductivity for samples: MCP1, MCP2, MCP3, MCP4.

A.1 Results for mold compound of type MCP1 for different reproduction measurements.

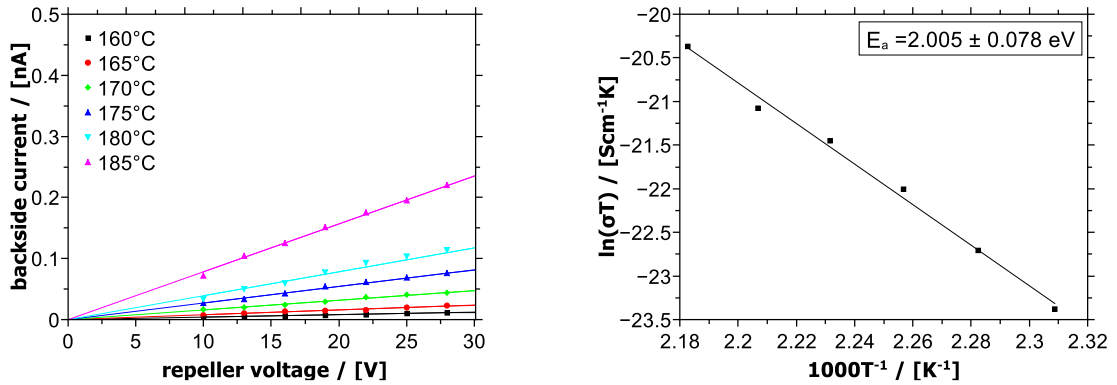


Fig. A1.1: Left: Temperature dependent current–voltage curves. Right: temperature dependence of the specific conductivity and value of E_{act} calculated from the slope of the linear regression.

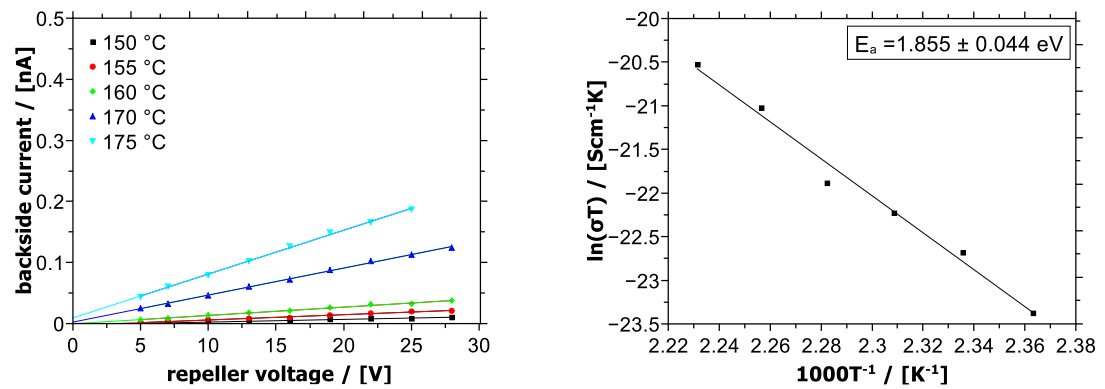


Fig. A1.2: Left: Temperature dependent current–voltage curves. Right: temperature dependence of the specific conductivity and value of E_{act} calculated from the slope of the linear regression.

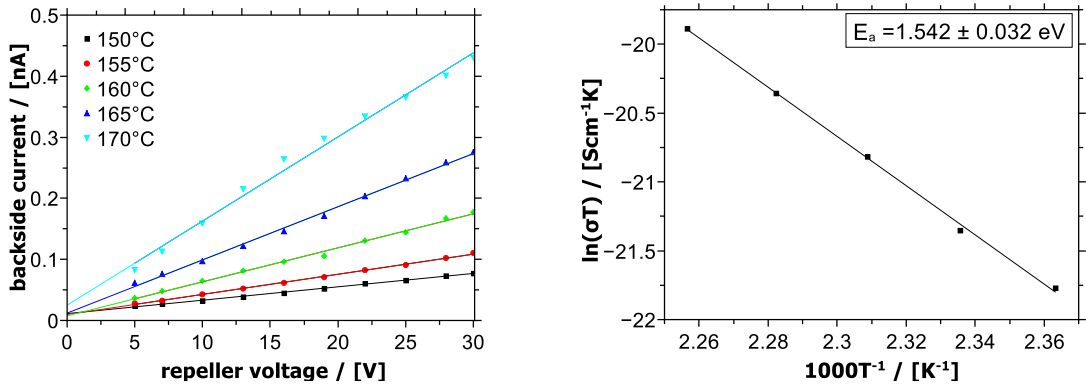


Fig. A1.3: Left: Temperature dependent current–voltage curves. Right: temperature dependence of the specific conductivity and value of E_{act} calculated from the slope of the linear regression.

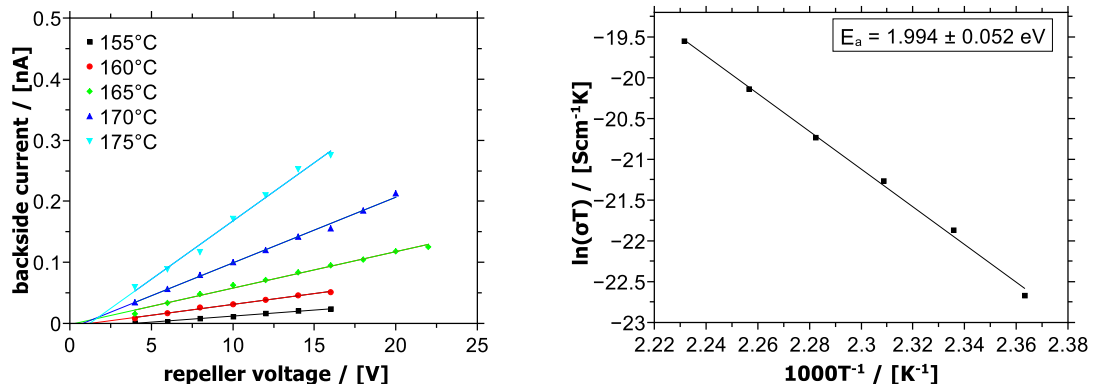


Fig. A1.4: Left: Temperature dependent current–voltage curves. Right: temperature dependence of the specific conductivity and value of E_{act} calculated from the slope of the linear regression.

A.2 Results for mold compound of type MCP2 for different reproduction measurements.

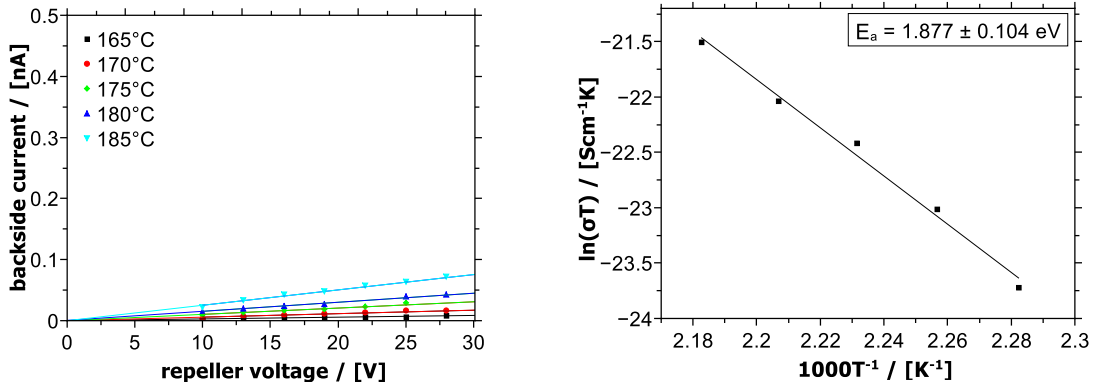


Fig. A2.1: Left: Temperature dependent current–voltage curves. Right: temperature dependence of the specific conductivity and value of E_{act} calculated from the slope of the linear regression.

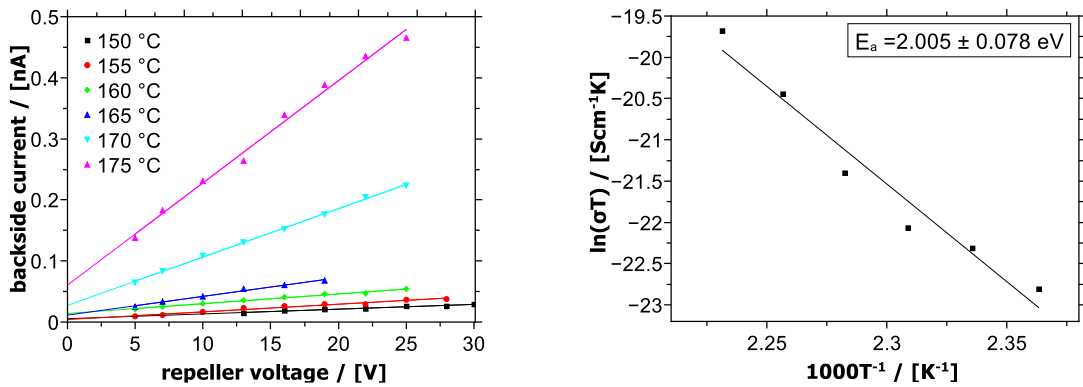


Fig. A2.2: Left: Temperature dependent current–voltage curves. Right: temperature dependence of the specific conductivity and value of E_{act} calculated from the slope of the linear regression.

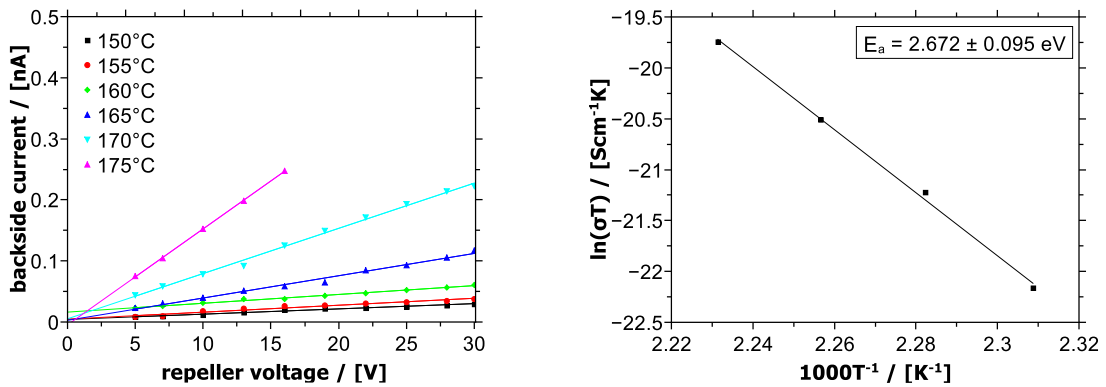


Fig. A2.3: Left: Temperature dependent current–voltage curves. Right: temperature dependence of the specific conductivity and value of E_{act} calculated from the slope of the linear regression.

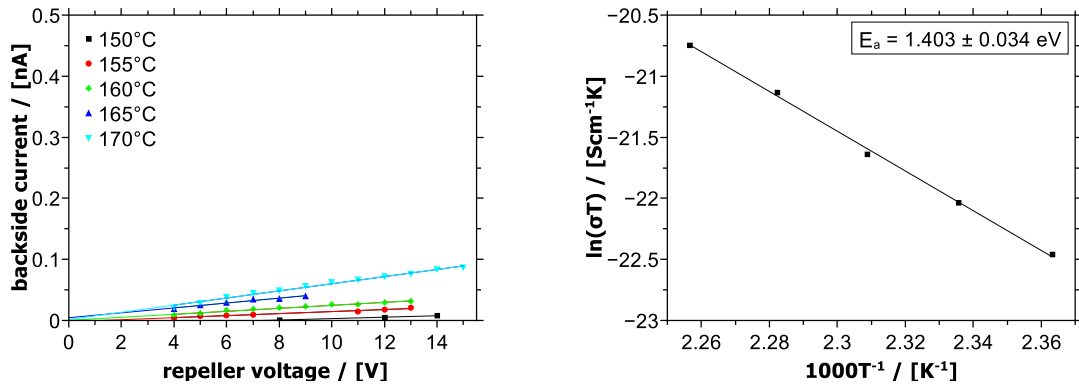


Fig. A2.4: Left: Temperature dependent current–voltage curves. Right: temperature dependence of the specific conductivity and value of E_{act} calculated from the slope of the linear regression.

A.3 Results for mold compound of type MCP3 for different reproduction measurements.

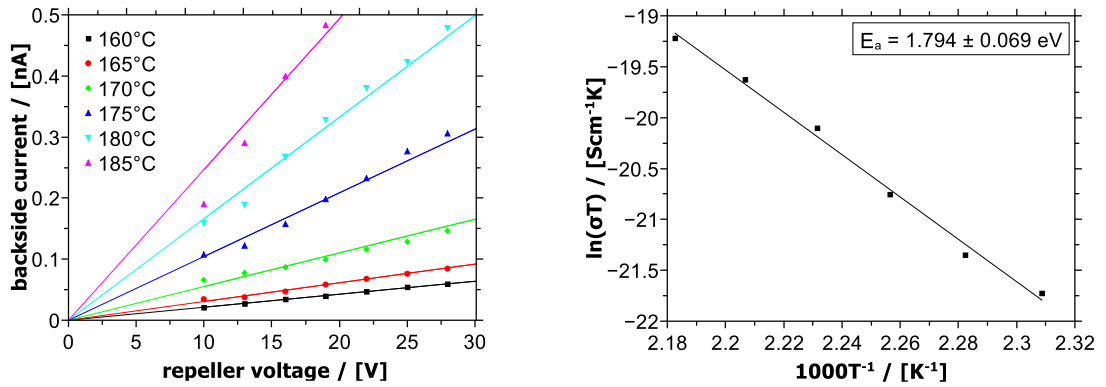


Fig. A3.1: Left: Temperature dependent current–voltage curves. Right: temperature dependence of the specific conductivity and value of E_{act} calculated from the slope of the linear regression.

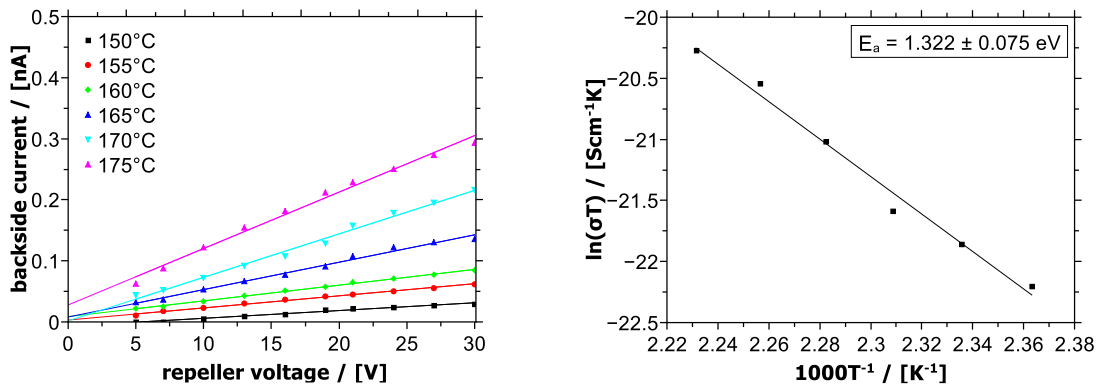


Fig. A3.2: Left: Temperature dependent current–voltage curves. Right: temperature dependence of the specific conductivity and value of E_{act} calculated from the slope of the linear regression.

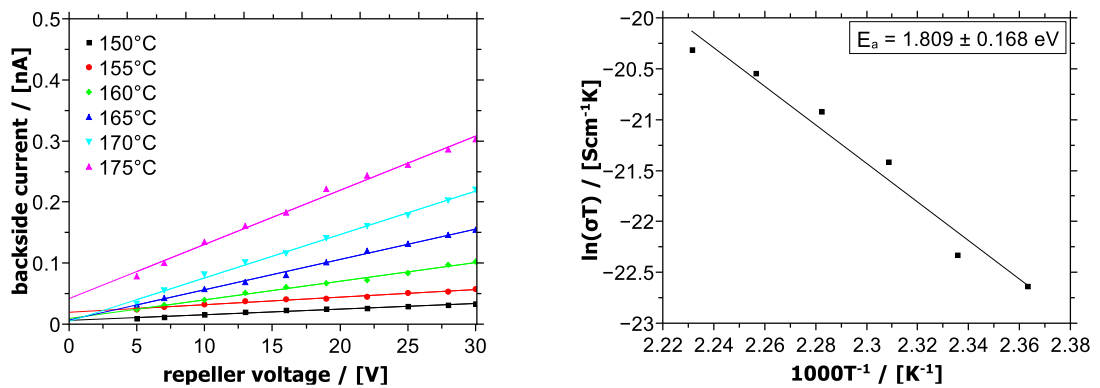


Fig. A3.3: Left: Temperature dependent current–voltage curves. Right: temperature dependence of the specific conductivity and value of E_{act} calculated from the slope of the linear regression.

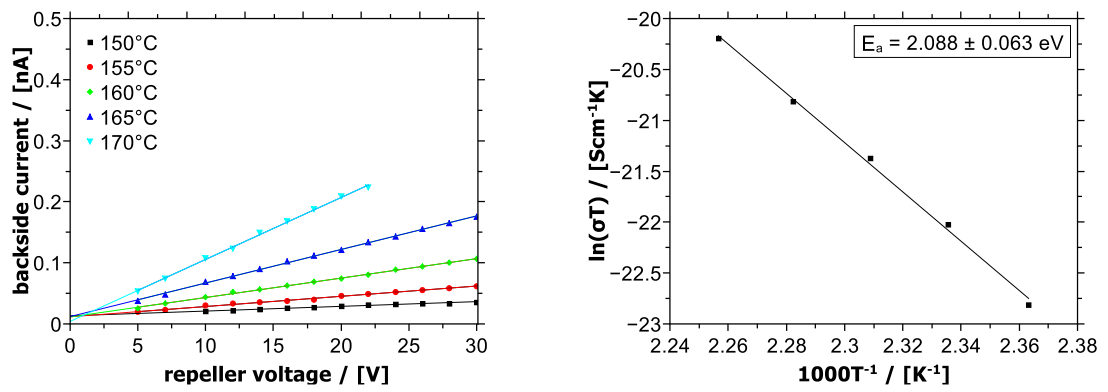


Fig. A3.4: Left: Temperature dependent current–voltage curves. Right: temperature dependence of the specific conductivity and value of E_{act} calculated from the slope of the linear regression.

A.4 Results for mold compound of type MCP4 for different reproduction measurements.

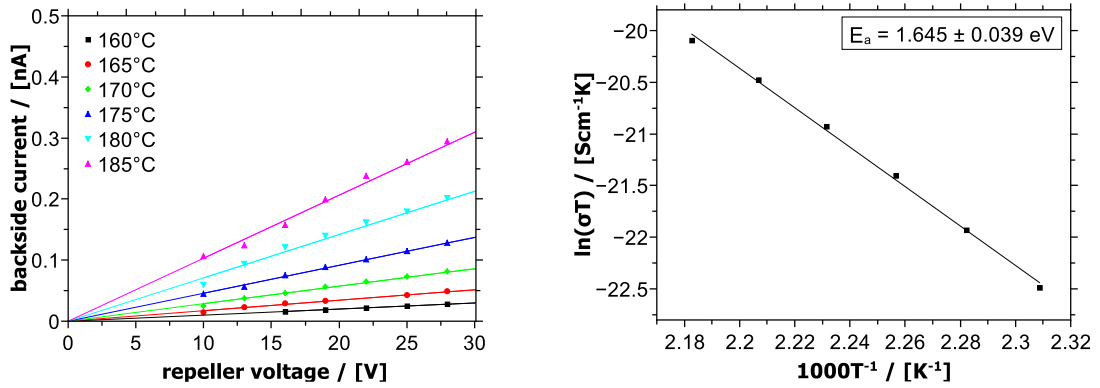


Fig. A4.1: Left: Temperature dependent current–voltage curves. Right: temperature dependence of the specific conductivity and value of E_{act} calculated from the slope of the linear regression.

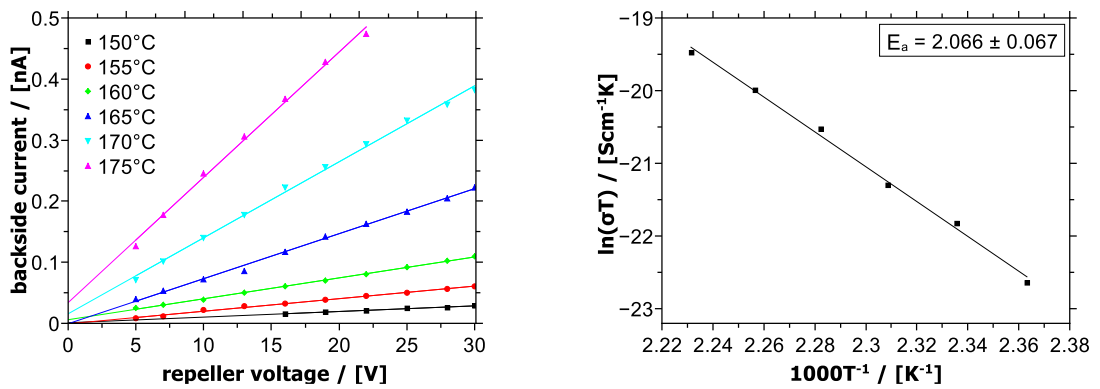


Fig. A4.2: Left: Temperature dependent current–voltage curves. Right: temperature dependence of the specific conductivity and value of E_{act} calculated from the slope of the linear regression.

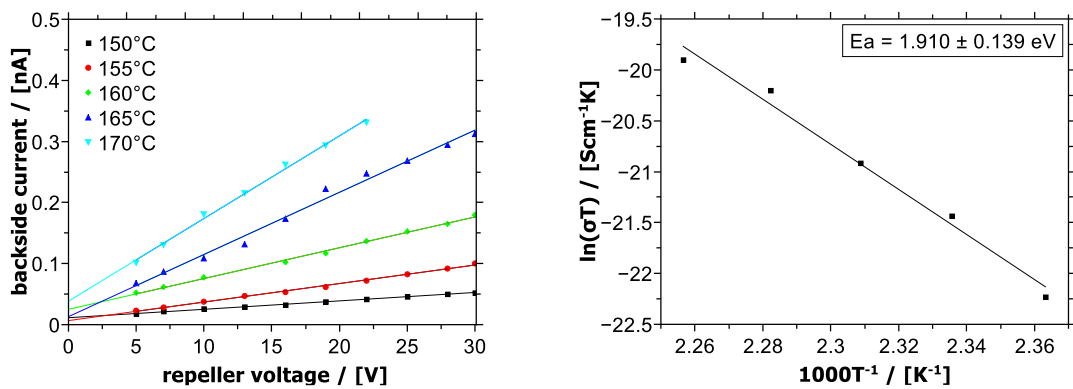


Fig. A4.3: Left: Temperature dependent current–voltage curves. Right: temperature dependence of the specific conductivity and value of E_{act} calculated from the slope of the linear regression.

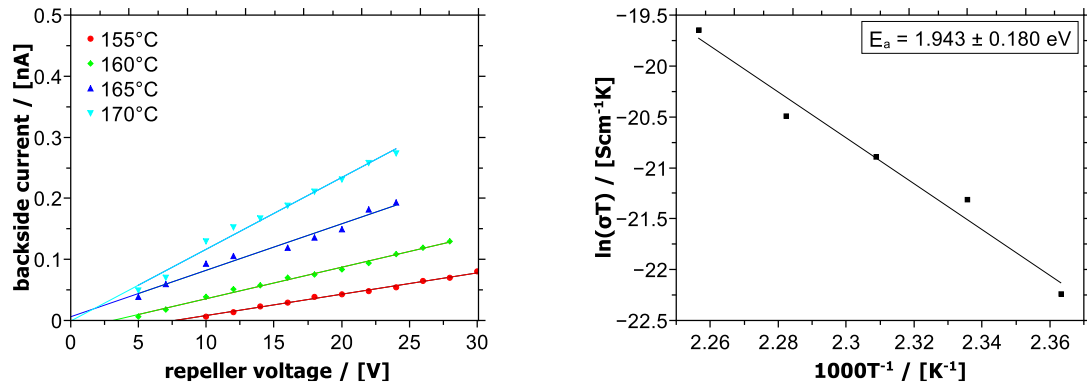
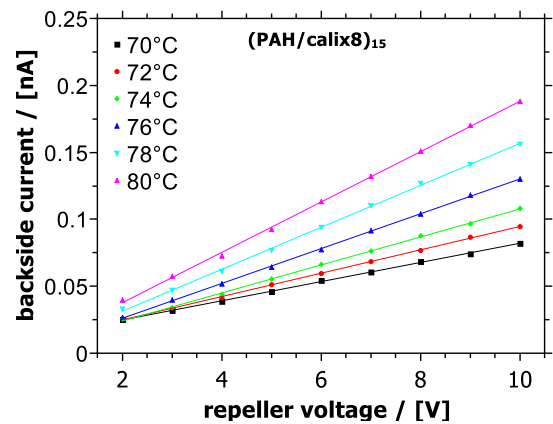
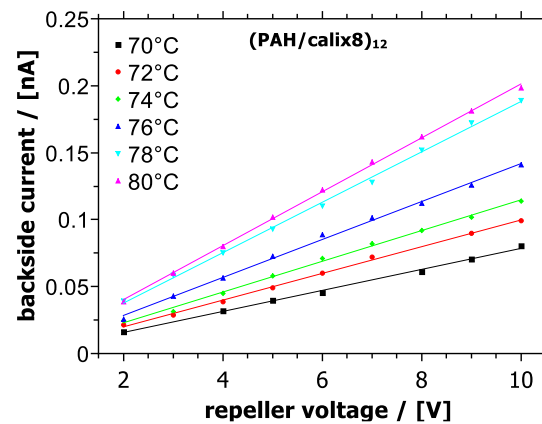
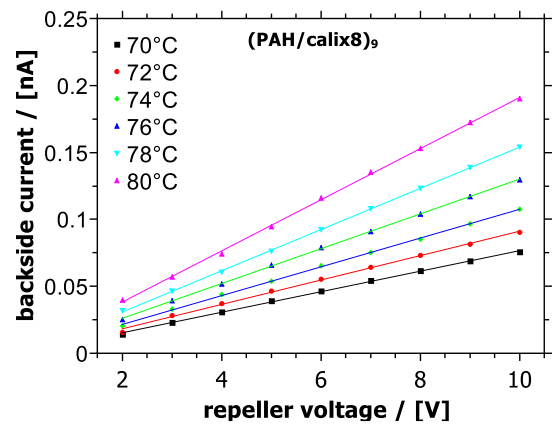
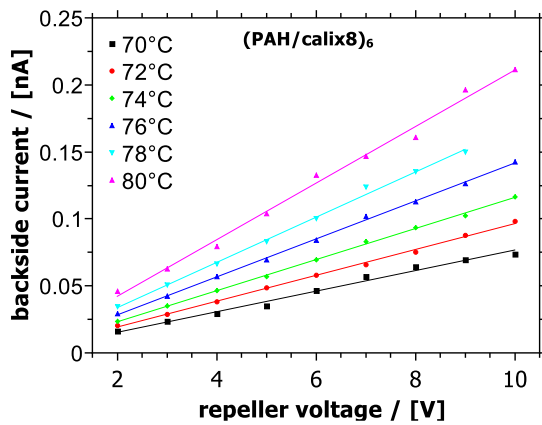
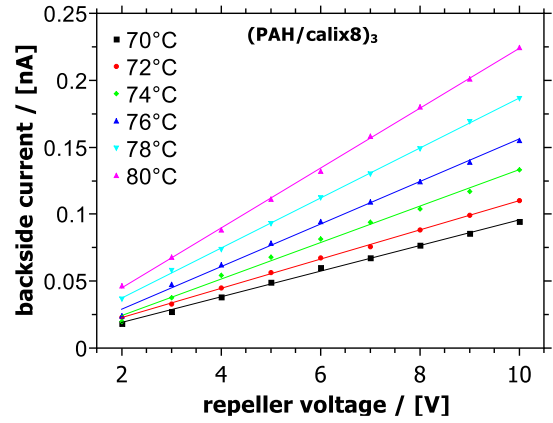
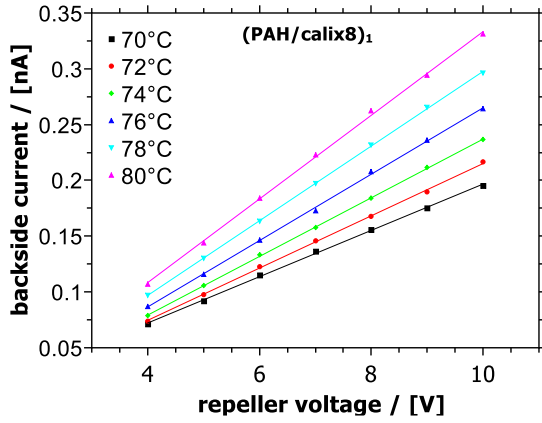


Fig. A4.4: Left: Temperature dependent current–voltage curves. Right: temperature dependence of the specific conductivity and value of E_{act} calculated from the slope of the linear regression.

Appendix B. Temperature dependent current–voltage characteristics for (PAH/calix8)_n with n = 1, 3, 6, 9, 12, 15, 20, 30 under the influence of the glass substrate.



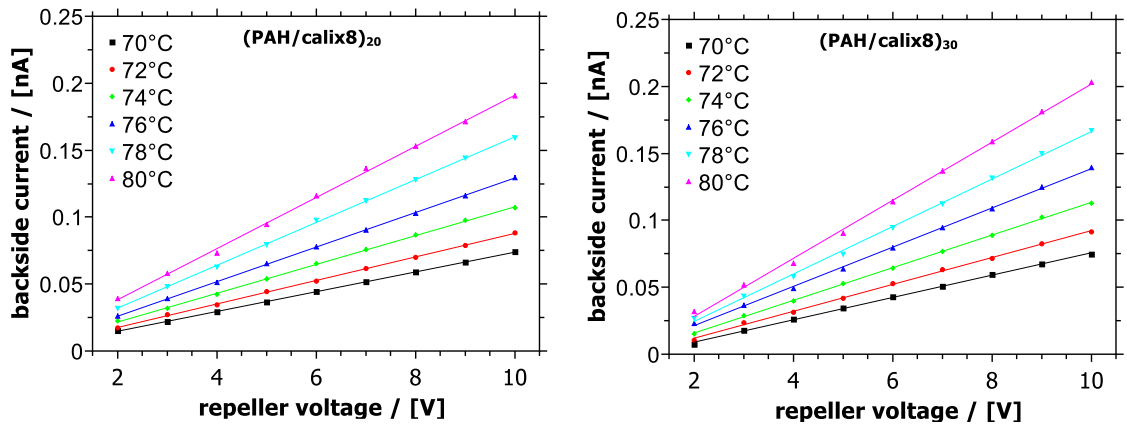


Fig. B: Temperature dependent current–voltage characteristic of $(\text{PAH/calix8})_n$ with $n = 1, 3, 6, 9, 12, 15, 20, 30$ under the influence of the glass substrate. The sample associated with the plot, e.g. $(\text{PAH/calix})_1$, is labeled in figures.

Appendix C: ToF-SIMS depth profiles.

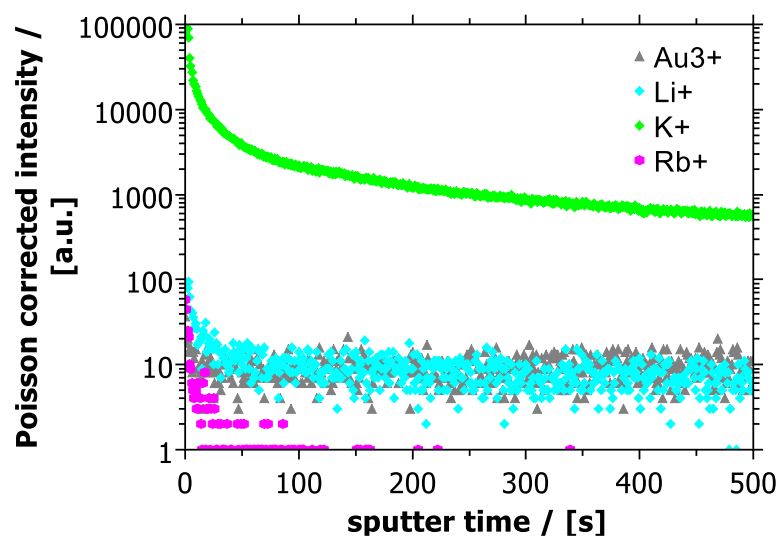


Fig. C1: ToF-SIMS depth profile of the gold foil used as substrate for the construction of Design IV. The analysis shows the presence of K⁺ within the gold. Neither Li⁺ nor Rb⁺ ions were found within the gold layer.

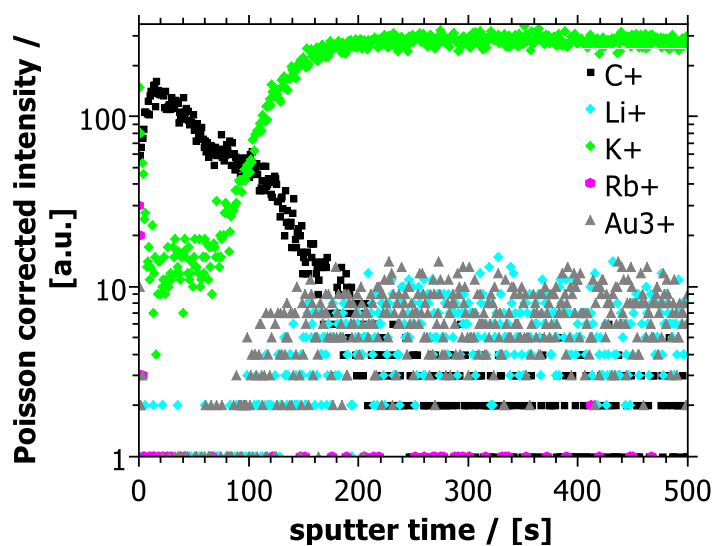


Fig. C2: ToF-SIMS depth profile of a fresh, not-bombarded sample of (PAH/calix8)₃₀.